Fabrication and characterization of graphene nanoribbons epitaxially grown on SiC(0001)

DISSERTATION

zur Erlangung des akademischen Grades

Dr. rer. nat.
im Fach Physik

eingereicht an der
Mathematisch-Naturwissenschaftliche Fakultät
Humboldt-Universität zu Berlin

von
M.Sc. Lauren Aranha Galves

Präsidentin der Humboldt-Universität zu Berlin:
Prof. Dr.-Ing. Dr. Sabine Kunst

Dekan der Mathematisch-Naturwissenschaftliche Fakultät:
Prof. Dr. Elmar Kulke

Gutachter:

(i) Prof. Dr. Henning Riechert

(ii) Prof. Dr. Saskia Fischer

(iii) Prof. Dr. Thomas Seyller

Tag der mündlichen Prüfung: 26.10.2018

Abstract

Graphene nanoribbons (GNRs) are promising for applications in nanoelectronics due to their unique properties. Therefore, achieving the controlled and high-quality synthesis of GNRs is anticipated to be of great importance. One of the methods which shows great potential is the growth of GNRs on surface facets of SiC(0001) by the surface graphitization method. The dependency of the GNR width on growth temperature and SiC substrate miscut angle (or initial step height) is first investigated. Monolayer GNRs were synthesized on SiC(0001) substrates with two different miscut angles at temperatures ranging from 1 410 to 1 460 °C. The structural characterization of the samples was performed by means of atomic force microscopy, scanning electron microscopy, transmission electron microscopy, and Raman spectroscopy. The GNR growth in lower step heights is best described by an exponential growth rate with regards to the growth temperature, which is correlated with the energy barrier for Si out-diffusion. On the other hand, a non-exponential rate is observed as a function of temperature for substrates with higher steps, which is associated with the formation of few-layer graphene on the step edges. The thicker layers, which act as an effective diffusion barrier, constrict Si diffusion.

The direct growth of isolated graphene nanostructures by using concepts of self-assembly and intercalation without further lithography and transfer processes is beneficial for their integration into device applications. Therefore, oxygen intercalation of epitaxial GNRs is investigated next by air annealing ribbons grown in different SiC(0001) substrates. Besides the conversion of monolayer into bilayer graphene near the step edges of SiC, the oxygen intercalation also leads to the formation of an oxide layer on the terraces of the substrate, leaving the bilayer GNRs electronically isolated from each other. Furthermore, the oxide layer formed underneath graphene can locally thicken at different spots, expanding the GNRs upward and eventually leading to the formation of holes on them. A lateral etching of the ribbons has also been observed, which differs depending on their width and miscut angle of the SiC substrate, offering an additional parameter for their controlled fabrication. Additionally, the oxygen intercalation of GNRs and complete graphene layers reveal a similar intercalation mechanism for both systems. Electrical characterization of bilayer GNRs, which is performed by means of a 4-tip scanning tunneling microscopy system, reveals that the ribbons are electrically decoupled from the substrate by the oxygen treatment. A robust hole concentration of around 1×10^{13} cm^{-2} and mobilities up to 700 cm^2/(V s) at room temperature are measured for GNRs whose typical width is 100 nm. The transport is not limited by the step roughness; thus, this scalable process can be easily extended to arbitrarily shaped structures.

The study of natural steps demonstrates the difficulty in finding suitable substrates for the growth of GNRs directly on etched SiC(0001) surfaces. The surface morphology of different substrates after hydrogen etching is varied. As a consequence, after GNR growth, the shape of the ribbons changes with substrate, leading to a non-standardized morphology, which hinders possible applications. As a solution to this issue, well defined mesa structures patterned by electron beam lithography on the surface of SiC(0001) substrates is lastly researched. However, the direct fabrication of GNRs on the patterned structures after the lithography process leads to unstable facets, that may decompose during the growth, or to parasitic ribbons. To circumvent such matters, vacuum annealing subsequent to the patterning of SiC substrates stabilizes the facets and creates smooth terraces. The resulting intercalated graphene is observed on the sidewalls of the mesa structures as well as patches throughout the terraces, whereas a defective graphene is detected on the suddenly rough trenches. Transport characterization of GNRs grown on the sidewalls of the patterned terraces shows a mobility in the range of 1 000 – 2 000 cm^2/(V s), which is homogeneous for various structures throughout the sample, indicating the reproducibility of this fabrication method and its potential for implementation in future technologies based on epitaxially grown GNRs.

Zusammenfassung

Graphen-Nanobänder (GNR für engl. graphene nanoribbons) sind auf Grund ihrer einzigartigen Eigenschaften vielversprechend für Anwendungen in der Nanoelektronik. Daher wird erwartet, dass die kontrollierte Synthese qualitativ hochwertiger GNRs von großer Bedeutung sein könnte. Eine der Methoden, welche hier großes Potential zeigt, ist das Wachstum von GNRs auf Oberflächenfacetten von SiC(0001) durch die Methode der Oberflächengraphitisierung. Zunächst wird die Abhängigkeit der Breite der GNRs von der Wachstumstemperatur und von dem Fehlschnitt des SiC-Substrats (bzw. der ursprünglichen Stufenkantenhöhe) untersucht. Einzelschichten von GNRs wurden auf SiC(0001)-Substraten mit zwei unterschiedlichen Fehlschnitten bei Temperaturen von 1 410 bis 1 460 °C synthetisiert. Die strukturelle Charakterisierung erfolgte mittels Rasterkraft-, Rasterelektronen- und Transmissionselektronenmikroskopie sowie Raman-Spektroskopie. Das GNR-Wachstum lässt sich bei niedriger Stufenkantenhöhe am besten durch eine exponentielle Wachstumsrate in Bezug auf die Wachstumstemperatur beschreiben, welche mit der Energiebarriere für die Ausdiffusion von Si korreliert ist. Anderseits wird bei Substraten mit höheren Stufenkanten eine nicht-exponentielle Rate als Funktion der Temperatur beobachtet, was mit der Bildung von mehrlagigen Graphen an den Stufenkanten in Verbindung gebracht wird. Die dickeren Schichten, welche als effektive Diffusionsbarriere fungieren, behindern die Si-Diffusion.

Das direkte Wachstum von isolierten Graphen-Nanostrukturen mittels Ansätzen der Selbstorganisation und Interkalation, ohne zusätzliche Lithographie- oder Transferprozesse, ist für deren Integration in Geräteanwendungen vorteilhaft. Von daher wird als nächstes die Sauerstoffinterkalation von epitaktischen GNRs mittels Ausglühen an Luft von Bändern untersucht, welche auf unterschiedlichen SiC(0001)-Substraten gewachsen wurden. Neben der Umwandlung von monolagigem zu zweilagigem Graphen in der Nähe der Stufenkanten von SiC, führt die Sauerstoffinterkalation zusätzlich zu der Bildung einer Oxidschicht auf den Terrassen des Substrats, was die zweilagigen GNRs elektrisch isoliert voneinander zurücklässt. Außerdem kann die Oxidschicht, welche sich unter dem Graphen bildet, an verschiedenen Stellen lokal dicker werden, wodurch sich die GNRs nach oben ausdehnen, was schließlich zur Bildung von Löchern in ihnen führt. Es konnte auch ein laterales Ätzen der Bänder beobachtet werden, welches in Abhängigkeit von deren Breite und des Fehlschnitts des SiC-Substrats variiert, was einen zusätzlichen Parameter für deren kontrollierte Herstellung bietet. Darüber hinaus zeigt die Sauerstoffinterkalation von GNRs und von vollständigen Graphenschichten einen ähnlichen Interkalationsmechanismus für beide Systeme. Die elektrische Charakterisierung der zweilagigen GNRs, welche mittels eines 4-Spitzen-Systems innerhalb eines Rasterkraftelektronenmikroskops durchgeführt wurden, zeigten dass die Bänder durch die Behandlung mit Sauerstoff elektrisch voneinander entkoppelt sind. Eine robuste Lochkonzentration von etwa 1×10^{13} cm^{-2} und Mobilitäten von bis zu 700 cm^2/(V s) wurden für die GNRs mit einer typischen Breite von 100 nm bei Raumtemperatur gemessen. Der Ladungsträgertransport wird nicht durch die Stufenrauhigkeit beschränkt und somit kann dieser skalierbare Prozess einfach auf beliebig geformte Strukturen ausgeweitet werden.

Die Untersuchung von natürlichen Stufen veranschaulicht die Problematik ein geeignetes Substrat für das direkte Wachstum von GNRs auf geätzten SiC(0001)-Oberflächen zu finden. Die Oberflächenmorphologie verschiedener Substrate ist nach dem Wasserstoffätzen unterschiedlich. Somit ändert sich die Form der Bänder nach dem GNR-Wachstum, was zu einer uneinheitlichen Morphologie führt, welche deren Anwendungsmöglichkeiten beeinträchtigt. Eine Lösung dieses Problems, wohl definierte Mesastrukturen gebildet mittels Elektronenstrahllithographie auf SiC(0001)-Substraten, wurde zuletzt untersucht. Die direkte Herstellung von GNRs auf die dermaßen gebildeten Strukturen führt jedoch zu instabilen Facetten, die sich während des Wachstums zersetzen können, oder zu parasitären Bändern. Um solche Probleme zu umgehen stabili-

siert ein Ausglühen in Vakuum nach der Strukturierung der SiC-Substrate die Facetten und führt zu glatten Terrassen. Das resultierende interkalierte Graphene wird an den Seitenwänden der Mesastrukturen sowie an verschiedenen Stellen überall auf den Terrassen beobachtet, während ein fehlerhaftes Graphen in den unerwartet rauhen Gräben nachgewiesen wird. Die Charakterisierung des Ladungsträgertransports von GNRs die auf den Seitenwänden der strukturierten Terrassen gewachsen wurden, zeigt eine Mobilität im Bereich von 1 000 bis 2 000 $cm^2/(V\,s)$, welche für verschiedene Strukturen auf der gesamten Probe homogen ist, was die Reproduzierbarkeit dieses Herstellungsverfahrens hervorhebt, sowie dessen Potential für die Implementierung in zukünftigen Technologien, welche auf epitaktischgewachsenene GNRs basieren.

Publications list

Publications related to this thesis

M.H. Oliveira Jr., J. M. J. Lopes, T. Schumann, L. A. Galves, M. Ramsteiner, K. Berlin, A. Trampert, and H. Riechert. *Synthesis of quasi-free-standing bilayer graphene nanoribbons on SiC surfaces.* Nat. Commun. **6**, 7632 (2015).

L. A. Galves, J. M. Wofford, G. V. Soares, U. Jahn, C. Pfüller, H. Riechert, and J. M. J. Lopes. *The effect of the SiC(0001) surface morphology on the growth of epitaxial mono-layer graphene nanoribbons*. Carbon **115**, 162 (2017).

I. Miccoli, J. Aprojanz, J. Baringhaus, T. Lichtenstein, L. A. Galves, J. M. J. Lopes, and C. Tegenkamp. *Quasi-free-standing bilayer graphene nanoribbons probed by electronic transport*. Appl. Phys. Lett. **110**, 051601 (2017).

Other publications

J. E. Boschker, L. A. Galves, T. Flissikowski, J. M. J. Lopes, H. Riechert, and R. Calarco. *Coincident-site lattice matching during van der Waals epitaxy.* Sci. Rep. **5**, 18079 (2015).

S. Fernández-Garrido, M. Ramsteiner, G. Gao, L. A. Galves, B. Sharma, P. Corfdir, G. Calabrese, Z. de Souza Schiaber, C. Pfüller, A. Trampert, J. M. J. Lopes, O. Brandt, and L. Geelhaar. *Molecular Beam Epitaxy of GaN Nanowires on Epitaxial Graphene*. Nano Lett. **17**, 5213 (2017).

G.K. Rolim, S.A. Correa, L. A. Galves, J. M. J. Lopes, G.V. Soares, and C. Radtke. *Chemical and morphological modifications of single layer graphene submitted to annealing in water vapor*. Appl. Surf. Sci. **427**, 825 (2018).

S. Fernández-Garrido, M. Ramsteiner, L. A. Galves, C. Sinito, J. M. J. Lopes, L. Geelhaar, and O. Brandt. *Plasma-assisted molecular beam epitaxy of GaN nanowires on epitaxial single-layer graphene*. Proc. SPIE **10532**, 105321U (2018).

Talks and conference presentations

L. A. Galves, T. Schumann, J. M. J. Lopes, and H. Riechert. *Structural study of monolayer graphene nanoribbons directly grown on SiC(0001)*. Frühjahrstagung der Deutschen Physikalischen Gesellschaft (DPG), Berlin - Germany, March 2015 (talk).

L. A. Galves, J. M. Wofford, J. M. J. Lopes, and H. Riechert. *Synthesis and structural characterization of monolayer and quasi free standing bilayer GNR on SiC(0001)*. GraphITA, Bologna - Italy, September 2015 (poster).

L. A. Galves, J. M. Wofford, U. Jahn, J. M. J. Lopes and H. Riechert. *Growth and characterization of monolayer graphene nanoribbons grown on SiC(0001)*. Frühjahrstagung der Deutschen Physikalischen Gesellschaft (DPG), Regensburg - Germany, March 2016 (talk).

L. A. Galves, J. M. Wofford, G. V. Soares, U. Jahn, C. Pfüller, H. Riechert, and J. M. J. Lopes. *The effect of the SiC(0001) surface morphology on the growth of epitaxial mono-layer graphene nanoribbons*. Compound Semiconductor Week 2017 (CSW2017), Berlin - Germany, May 2017 (poster).

L. A. Galves, M. Heilmann, A. Tahraoui, H. Riechert, and J. M. J. Lopes. *Etching effect of bilayer graphene nanoribbons on SiC(0001) by O_2 intercalation upon air annealing*. Graphene Week 2017, Athens - Greece, September 2017 (poster).

Berlin, 30.07.2018 Lauren Aranha Galves

Contents

1 Introduction

1.1 Graphene

Graphene is a hexagonal structure consisting of sp^2 hybridized carbon atoms [1]. It is a single atomic plane of graphite, which is sufficiently isolated from its environment to be considered free-standing [2]. Described as the "mother" of all graphitic carbon materials [3], its honeycomb network is the building block for zero-dimensional (0D) fullerenes (wrapped up in buckyballs), one-dimensional (1D) carbon nanotubes (rolled up sheets), and three-dimensional (3D) graphite (stacked graphene sheets held together by van der Waals forces).

Graphite, its most famous allotrope, has been known for nearly 500 years, given that it is abundant and naturally occurring. Thanks to its layered morphology and weak forces between adjacent layers, it was used initially as a marking instrument in a way analogous to nowadays pencils, and more recently as dry lubricants [4].

Although atomic planes are known constituents of bulk crystals, one layer thick materials like graphene remained unknown until recently due to a natural prohibition to grow low-dimensional crystals [3]. High temperatures, which are necessary for crystal growth, are also synonym of thermal fluctuations that are detrimental for the stability of macroscopic 1D and two-dimensional (2D) objects. This means that 2D crystallites are forced to morph into a variety of stable 3D structures [2].

Even though atomically thin crystals cannot be naturally grown, they can be artificially fabricated and there are two main routes to do so. The first path is to mechanically split layered materials like graphite into individual atomic planes, also called mechanical exfoliation. This method was first used in the seminal work of Novoselov et al. in 2004 [5], which established this new research field by presenting an easy way to produce and identify graphene [6]. This technique provides crystals of high structural and electronic quality, which can reach millimeter sizes. Besides manually cleaving graphite by using, for instance, a scotch tape, it is possible to automate the process by employing ultrasonic cleavage [7], which leads to stable suspensions that can be used to make polycrystalline films and composite materials, allowing graphene production on an industrial scale. The successful isolation of graphene by mechanical exfoliation from highly oriented pyrolytic graphite [5] as well as its unconventional properties [8, 9], which opened the possibility for amazing physical and technological potential, lead to an increase in graphene research.

The second main way to produce graphene is by epitaxially growing it on top of other crystals. This route does not require to search for and manipulate individual flakes, instead it offers the possibility to scale up graphene towards wafer sizes which can be easily investigated afterwards. Graphene samples can be grown on metal surfaces by catalytic reaction or by chemical vapor deposition [10, 11, 12, 13], a generally self-limiting growth which often produces a monolayer of graphene, but that requires transfer to other substrates for technological applications. In this regard, epitaxial graphene grown by thermal decomposition of SiC surfaces [14] by annealing SiC substrates at high temperatures is a promising way to fabricate large area graphene directly on semi-insulating substrates.

1.2 Short history of graphene

Graphene has been studied for seventy years [15, 16, 17] and experiments on graphite have been utilizing progressively fewer layers [18], but none of them were able to unambiguously isolate or to identify any of graphene's unique properties [19, 15]. Graphene oxide, for instance, was independently synthesized in 1958 [20], in 1898 [21], and previously in 1859 [22]. Even synthesis of monolayer graphene (MLG) using silicon carbide substrates was achieved by 1975 [23], though no unique properties had been reported at the time. Graphene was then described as an academic material and believed not to exist in the free state [24], since it was considered unstable.

Therefore, the successful isolation and subsequent characterization of graphene by Geim and Novoselov at Manchester University [5] in 2004 was essential for the establishment of graphene as a research field. The researchers isolated and characterized pristine graphene for the first time exploiting the Scotch Tape method, a process in which an adhesive tape removes flakes of graphite from a piece of highly ordered pyrolytic graphite (HOPG) and deposits them on an appropriate substrate, in this case a SiO_2 surface. This process is repeated until a one atom thick layer of graphite, i. e. graphene, is left isolated on the substrate [5].

Other free-standing 2D atomic layers, such as boron nitride, were later discovered [25], generating an increase in research, since 2D crystals were considered thermodynamically unstable at finite temperatures [26]. Studies demonstrated that the 2D crystals were continuous and exhibited high crystal quality [5, 25, 8, 9, 27, 28].

The theory of Landau and Peierls claimed that strictly 2D crystals were thermodynamically unstable and could not exist [29, 26], since, at any finite temperature, contributions of thermal fluctuations should lead to displacements of atoms comparable to interatomic distances. The idea behind this theory is that as film thickness decreases, their melting temperature rapidly decreases, destabilizing a film at dozens of atomic layers [30, 31]. Consequently, atomic monolayers were solely know as part of 3D structures, generally epitaxially grown [30, 31]. However, thanks to crumpling and wrinkling in free layers [28] and to van der Waals bonding to the substrate in quasi-free standing layers [32], graphene and other 2D materials have been successfully isolated experimentally.

Due to its exceptional electronic qualities, including charge carriers that behave as massless Dirac fermions and travel thousands of interatomic distances without scattering [5, 25, 8, 9], graphene was initially more studied than other 2D materials. A particular turning point was the discovery that graphene could be observed by an optical microscope if placed on top of a Si wafer with a SiO_2 film of a specific thickness (300 nm) [25]. The fact that a 5 % difference in film thickness makes graphene invisible grants this discovery an important place in the early graphene research, when finding appropriate monolayer was essential. More recently, Raman spectroscopy has also been found a useful tool for determining the number of layers in graphene samples [33, 34] (see Section 2.3).

The combination of a simple isolation method and the discovery of unique properties ensured the Nobel Prize for physics in 2010 to Geim and Novoselov for groundbreaking experiments regarding the 2D material graphene [35].

1.3 Crystalline structure

The hexagonal structure of graphene is formed by sp^2-bonded carbon atoms that are separated by the interatomic distance $a = 1.42$ Å. The unit cell of a graphene monolayer consists of two carbon atoms, A and B, each forming a triangular 2D network (Figure 1.1 a). The first Brillouin zone in the reciprocal lattice is presented in Figure 1.1 b.

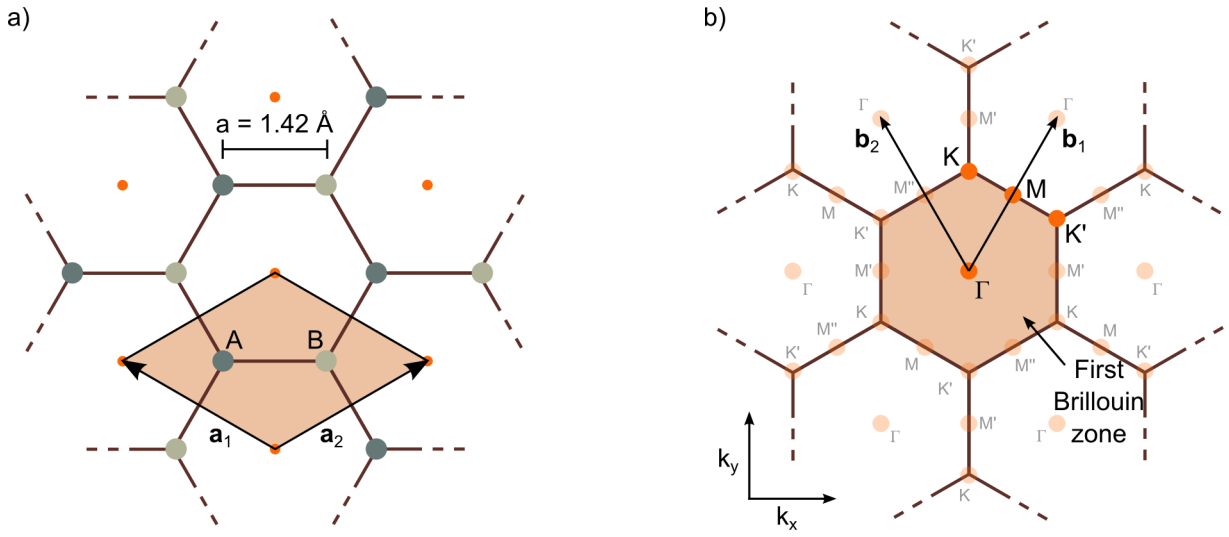

Figure 1.1: (a) Honeycomb lattice structure of MLG with two inequivalent atoms A and B, lattice unit vectors $\mathbf{a}_1$ and $\mathbf{a}_2$ and the unit cell (shaded orange), besides the distance between neighboring atoms a. (b) Reciprocal lattice of MLG with the first Brillouin zone (BZ), in shaded orange, and its high symmetry points, the two primitive vectors $\mathbf{b}_1$ and $\mathbf{b}_2$, and the reciprocal space coordinate axes. In the center of the first BZ is the Γ point, in its two inequivalent corners the Dirac points (K and K') and the three crystallographically equivalent points M, M' and M'' are situated in the middle of the corners.

The stacking of graphene layers perpendicular to the plane of each layer corresponds to a 3D graphite structure. If carbon atoms from one layer are positioned in the center of the hexagons of the adjacent layer, then the stacking is called Bernal, or AB. In this case, the unit cell consists of four carbon atoms, A1, A2, B1 and B2, on the two layer planes. It has been shown that bilayer graphene (BLG) on SiC(0001) exhibits this type of stacking [36], therefore also possessing four carbon atoms in its unit cell (Figure 1.2).

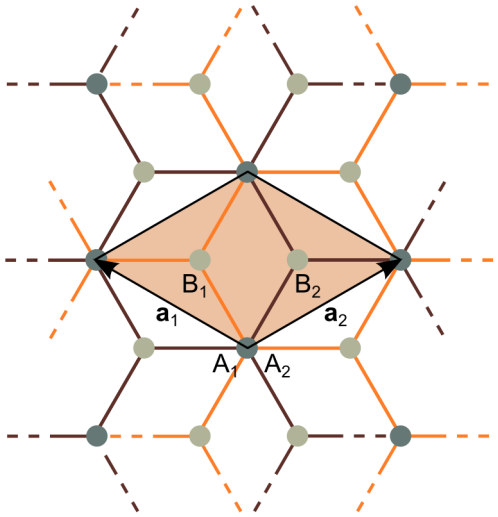

Figure 1.2: A top view of the real space lattice of BLG. The orange and brown lines denote the upper and lower lattices, in which the inequivalent atoms A_1, B_1 and A_2, B_2 belong to the different planes. The lattice unit vectors are $\mathbf{a}_1$ and $\mathbf{a}_2$.

1.4 Graphene's properties

Carbon, the elementary constituent of graphene, has 6 electrons in the configuration $1s^2\,2s^2\,2p^2$, i.e. 2 electrons fill the inner shell 1s, which is close to the nucleus and therefore irrelevant for chemical reactions, and 4 electrons occupy the outer shell of 2s and 2p orbitals. In the presence of other atoms, such as H, O, or other C atoms, it is favorable to excite one electron from the 2s to the third 2p orbital, in order to form covalent σ bonds with the other atoms. This process leads to a gain in energy which compensates the invested energy to excite the electron in the first place. Therefore, in the excited state, four quantum mechanical states $\mid 2s >$ and $n \mid 2p_j >$, which are called sp^n hybridization, are superposed [37]. If the superposition occurs between one 2s and two 2p orbitals, one obtains the planar sp^2 hybridization. The sp^3 hybridization is obtained by superposing one 2s and three 2p orbitals, which consists of a tetrahedron. The carbon atoms in graphene condense in a honeycomb lattice due to their sp^2 hybridization.

Carbon has therefore four valence electrons, three of which form tight covalent σ bonds with neighboring atoms in the plane and are responsible for the toughness of the lattice structure in graphene [6], and one conduction π electron, which is the one responsible for most electronic properties of graphene [38]. Wallace developed a "tight binding" method to calculate the band structure of graphene (at the time called simply a single layer of graphite) [15], which is now widely used to study the energy bands of graphene. The energy dispersion of π electrons in the honeycomb lattice is shown in Figure 1.3 a, as well as a close-up of the energy bands near to one of the Dirac points (Figure 1.3 b) and a cut along the characteristic symmetry points (Figure 1.3 c). The valence (or π) band is completely filled, whereas the conduction (or $\pi*$) band is completely empty. The Fermi level is therefore situated at the points where the two bands touch each other, which are called the Dirac points (or K and K' points). Because the valence and conduction bands are touching each other, graphene can be seen as a zero-gap semiconductor or as a zero-overlap semimetal [6].

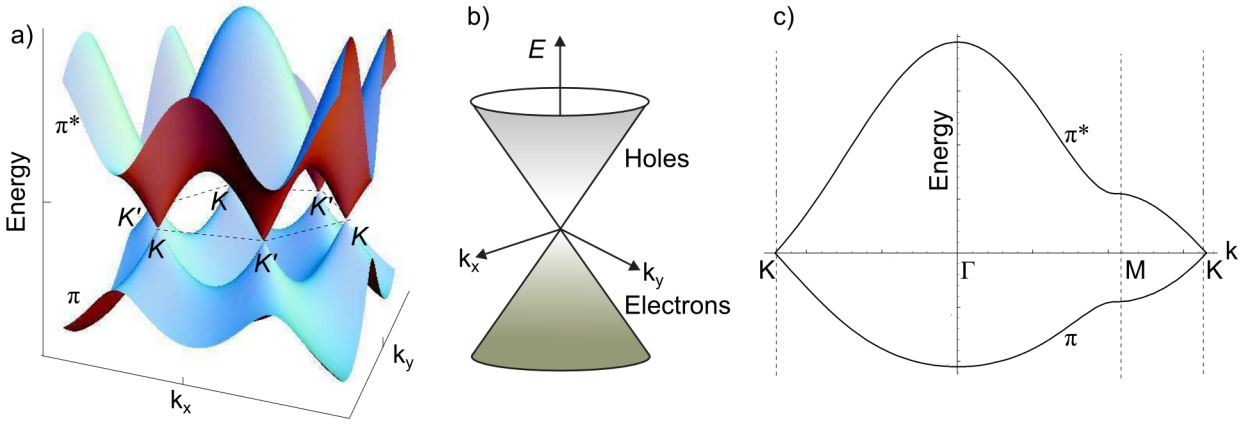

Figure 1.3: Energy dispersion of MLG obtained within the tight-binding approximation. The valence (π) and conduction ($\pi*$) bands touch at the Dirac points (K and K'), where the Fermi level is positioned. (a) Energy dispersion as a function of the wave vector components k_x and k_y. Adapted from [37]. (b) Enlargement of the band structure close to the K and K' points showing the Dirac cones. Adapted from [39]. (c) Cut through the energy dispersion along characteristic lines (connecting the points $K \rightarrow \Gamma \rightarrow M \rightarrow K$). Adapted from [37].

While for most materials in condensed matter physics the Schrödinger equation, which charac-

terizes quantum systems, fully describes their electronic behavior, in graphene this is not the case. Its charge carriers are the only ones to mimic relativistic particles and are, therefore, best described by the Dirac equation [24, 40, 41, 42, 43, 44, 45, 46, 47] (which takes into account both quantum mechanics and special relativity). Electrons propagating through graphene's honeycomb lattice completely lose their effective mass, resulting in new quasiparticles that, at low energies, are accurately described by massless Dirac fermions [3, 48, 49].

The π bonds formed by the unaffected p_z orbital oriented perpendicular to the planar structure result in the π band, which is responsible for the astonishing electrical conductance in graphene [6, 50]. Because of graphene's two equivalent C sublattices, quantum mechanical hopping of fermions between the two sublattices forms two energy bands that intersect at the Dirac point (K and K') [51]. As a result, quasiparticles in graphene exhibit a linear dispersion relation, behaving as if they were massless relativistic particles with the speed of light c replaced by the Fermi velocity $v_F \approx c/300$ [51]. The quasiparticles behave differently from conventional metals and semiconductors (which have a parabolic energy spectrum), and, due to their band dispersion, they can reach a mobility of 2.5×10^5 cm^2/(V s) at room temperature [52, 53], a value that exceeds the theoretical limit [$\sim 2 \times 10^5$ cm^2/(V s)] [54]. Depending on the quality and fabrication method of the graphene sample, the charge carrier mobility will range from 2 000 to 200 000 cm^2/(V s) [55, 56, 57, 1, 58] (with the best samples measured for graphene exfoliated from HOPG). The mobility is rather unaffected by temperature and upon changing the carrier concentration by both electrical or chemical doping [6], which shows how robust the transport properties are in graphene.

Besides extraordinary mobilities, another exceptional feature in graphene is the ambipolarity of its charge transport. Graphene's charge carriers can be tuned continuously between electrons and holes in concentrations as high as 10^{13} cm^2 when subject to an ambipolar electric field [5, 3]. Both extremely high carrier mobility and an ambipolar field-effect had been predicted theoretically for graphene [15, 17]. Another indication of graphene's extreme electronic quality is the quantum Hall effect, which can be observed even at room temperature [59, 60, 61, 9, 62, 63].

Graphene's mechanical stiffness, strength and elasticity, as well as very high electrical and thermal conductivity, which have long been the interest of many theoretical studies and more recently became an appealing area for experimental researchers, are supreme [3, 2]. A monolayer of graphene displays a low optical absorption of 2.3 % [64], or an extremely high optical transparency of up to 97.7 % [19]. Thermal conductivity in graphene had initially been measured above 3 000 W/(m K) [65], which is already very high, but record values of $\sim$5 000 W/(m K) were also determined [66]. Furthermore, unlike any other material, it shrinks with increasing temperature for all temperatures [67]. A high Young's modulus of $\sim$1 TPa and an intrinsic strength of 130 GPa [68] (very close to the value predicted by theory) were determined for graphene. Additionally, complete impermeability to any gases including helium [69] (for defect-free graphene), extraordinarily large specific surface area of 2 630 m^2/g [70], and the first ever detection of single molecule adsorption event [71] are equally unprecedented. Finally, it can be stretched by 20 %, more than any crystal [72, 68], and its breaking strength reaches the theoretical limit of $\sim$ 40 N/m [68].

1.5 Possible applications

Because of its unique structure and excellent electrical, thermal, and mechanical properties, graphene-based smart devices are expected to be superior than its counterparts, for instance in energy conversion materials and device systems that convert energy from different forms (e.g., electric, chemical, photonic, thermal) to mechanical actuators and electrical generators [73]. Graphene composites and macroscopic graphene assemblies are also expected to be promising for energy storage applications [27, 74, 75, 76, 77, 78]. As a consequence of its high optical transparency,

potential applications like transparent electrodes in solar cell [79] and holographic data storage [80] are foreseen. Graphene is also recognized as one of the most promising candidates for future applications in nanoelectronics due to its high carrier mobility [52, 81]. Due to its transparency, conductivity and elasticity, graphene could additionally be used as flexible electrodes [50].

In general, graphene's high intrinsic carrier mobility, large specific surface area, high mechanical strength, and light transparency, as well as superior flexibility, shows extensive potential for applications in a variety of fields [73]. In particular, field effect transistors (FETs) could operate at frequencies as high as 100 GHz as of 2010, whereas graphene FETs operate at terahertz frequencies [82], therefore expanding their operational range. However, the absence of a bandgap makes it difficult to switch off a graphene FET, leading to a rather small on/off ratios [81]. In order for all of those applications to become a reality, graphene sheets need to be modified to tailor their intrinsic physical and chemical properties [27, 74, 83, 75, 84, 85]. Therefore, two things are necessary: large-area growth and modification of graphene's intrinsic properties. Those points will be discussed in the next sections.

1.6 Large-area epitaxial graphene on SiC

For graphene to be attractive to industrial applications, it must offer similar outstanding properties in samples prepared in large scale as it offers for the state-of-the-art samples. The latter are prepared by graphite exfoliation [5] followed by μm-sized transfer[53, 86] , which are not scalable methods. The properties and performance of future graphene devices also depends on the number of layers and the overall quality of the crystal lattice [54, 87, 88, 89], therefore the progress of new applications will depend on the development of precise and scalable fabrication methods that will permit the synthesis of graphene with high structural quality.

Among the different methods to produce graphene, the surface graphitization of SiC is certainly one of the most promising large-scale ones [90]. Graphene samples have been fabricated on SiC substrates with a diameter as large as two inches [91]. With this approach, the direct fabrication of a graphene monolayer on an insulating material can be accomplished; which is ideal for device processing and alleviates the need for transfer to another substrate (as is required for graphene synthesized on metals) [14, 92]. However, the cost of a SiC substrate, about $375 for a two-inch wafer [93], is considered a limiting factor in the utilization of this method.

The graphitization of SiC crystals and SiC surfaces was first studied in 1962 by Badami [94] and in 1975 by Van Bommel et al. [23], respectively. The crystal structure of different SiC polytypes, i.e., particular stacking arrangements, is shown in Figure 1.4, as well as the notation of such systems. The basal plane surfaces, perpendicular to the c-axis, exhibit two different surface terminations: the Si-terminated SiC(0001) surface, or Si-face, and the C-terminated SiC$(000\bar{1})$ surface, or C-face, both of which are polar surfaces. The group of de Heer at the Georgia Institute of Technology was the first to investigate the transport properties of epitaxial graphene grown on the Si-face in 2004 [14], whereas graphene fabricated on the C-face was studied in 2006 [95].

At the polar surfaces, Si and C atoms, which have each four valence electrons, make three bonds to the underlying atoms. The fourth unsaturated bond, which points outwards, is filled by a single electron, and is called a "dangling bond" [6]. Because dangling bonds are energetically unfavorable for the surface of the crystal, they are either saturated by foreign atoms like hydrogen [96] or the surface atoms rearrange themselves forming new bonds, a process that happens naturally in the absence of foreign atoms and that is called "reconstruction". Both these processes may induce a change in the periodicity at the surface.

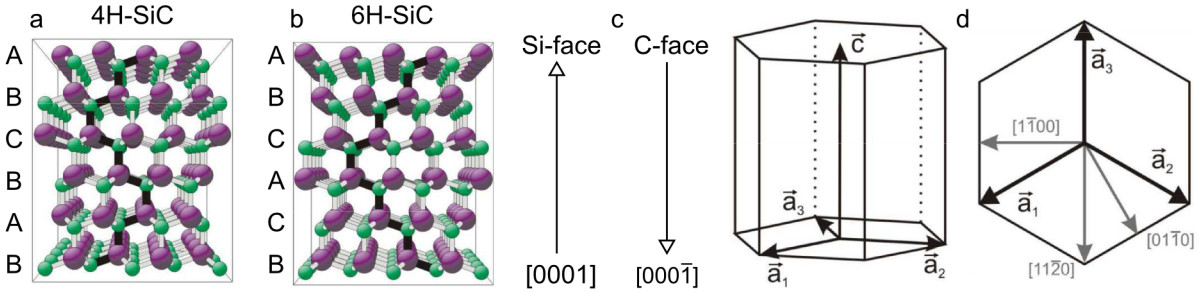

Figure 1.4: Crystal structure of hexagonal (a) 4H-SiC and (b) 6H-SiC. Large violet spheres correspond to Si atoms, whereas small green spheres to C atoms, and the thick black line indicates the stacking sequence. (c) the direction of the Si-face, or (0001), and the C-face, or $(000\bar{1})$, for both systems as well as (d) the hexagonal notation are also illustrated. Taken from [6].

The growth of graphene on SiC substrates is based on the thermal decomposition of the surfaces. Since Si has a higher vapor pressure than C, when heated at high temperatures the Si atoms sublimate first and leave behind C atoms, which recombine and form graphene layers at the surface [97]. However, the growth, oxidation, surface reconstruction and graphitization behavior occur in a different manner for the Si- and the C-face of SiC, since those surfaces are quite distinct from each other. A stronger localization is detected in the SiC$(000\bar{1})$ surface in comparison to the other polar face due to charge densities of the dangling bond states [98], for instance. In fact, the surface orientation is the parameter responsible for the nature of the reconstruction, whereas polytype (4H or 6H) does not play a role [99].

Growth of epitaxial graphene on SiC(0001) is characterized by the first carbon layer, which is covalently bound to the substrate and therefore does not behave like a graphene layer. This interface layer is the carbon rich reconstruction $\left(6\sqrt{3}\times 6\sqrt{3}\right) R30°$, commonly called "buffer layer" (BL). To understand the notation, one considers substrate unit vectors $\mathbf{a}_1$ and $\mathbf{a}_2$ (Figure 1.1) and reconstruction unit vectors $\mathbf{b}_1$ and $\mathbf{b}_2$, so that the surface reconstruction is usually denoted as $(p\times q)\, R\phi$ [100], where $p = b_1/a_1$, $q = b_2/a_2$ and ϕ is the angle between the reconstruction and substrate unit vectors (if $\phi = 0$, the angle is omitted). By counting the number of C atoms in the BL or, likewise, in a graphene layer, it is clear that three SiC bilayer are necessary to form each carbon layer. New carbon layers are formed by the desorption of Si atoms and each new layer entails the reformation of a $\left(6\sqrt{3}\times 6\sqrt{3}\right) R30°$ reconstruction [101], so that the previous BL is released from its covalent bonding to the substrate and is therefore transformed into a graphene layer. In this sense, the BL acts as a precursor phase for graphitization and is responsible for the ordered growth of graphene layers. Because the reciprocal unit cell of the BL is rotated by 30° with respect to the substrate, all graphene layers have the same 30° rotation in regard to the SiC(0001) surface.

Slightly less than a third of the C atoms in the BL are bounded to a Si atom of the SiC surface and to three other C atoms from the interface layer. The other two thirds are sp^2-bonded to other C atoms in the BL [101, 6]. This generates a spatial dependence of the electronic distribution, which influences the graphene layers above. The BL has been considered the responsible for a reduced mobility in epitaxial graphene grown on the Si-face. Density functional theory (DFT) calculations have shown that charge transfer between Si dangling bonds of the SiC(0001) surface and the BL creates an electric dipole in the BL that is responsible for n-doping the epitaxial graphene [102, 103]. For an increasing number of graphene layers, the electric field is screened and the upper layers are less doped. In general, epitaxial graphene on SiC(0001) shows a high structural order and a well defined number of layers on a large scale [92]. Mobilities up to 29 000 $\mathrm{cm}^2/(\mathrm{V\,s})$

were measured in epitaxial graphene on SiC(0001) [104].

In contrast, epitaxial graphene on SiC$(000\bar{1})$ grows with rotational disorder and limited thickness control [105]. Additionally, no covalent bonding of graphene to the SiC substrate is observed upon graphitization [105]. Graphene grows more rapidly on the C face, which typically leads to the formation of multilayer thick graphene films that may offer exceptionally high electronic quality [$\mu \approx 250\,000$ cm^2/(V s) at room temperature] [52].

1.7 Bandgap opening

Graphene is considered an ideal candidate for nanoelectronic applications due to its unique properties, such as scalability, high mobility, and even room temperature ballistic transport [14, 106]. However, the lack of an electronic bandgap restricts its use in several applications such as FETs. When used as the conducting channel in a FET, the main result of the gapless nature of graphene are small on/off current ratios [107]. An electronic bandgap is a necessary attribute for a high on/off ratio in a digital switching device such as a FET. More generally, electronic devices consist of semiconductors which exhibit small yet significant bandgaps [108], however large area graphene shows no bandgap. Therefore, graphene-based devices are virtually impossible to be turned off at any reasonable temperature because large carrier populations are easily produced in graphene by thermal energy and fluctuations. This results in a high "leakage" current which is unsuitable for implementation in real devices [4].

There are many ways to induce a bandgap in graphene. One possibility is to apply uniaxial strain to a graphene sheet, though extremely high strain would be necessary to provide useful gaps for electronic applications, which is not realistically achievable [109, 72, 110]. Chemical methods such as doping and functionalization by atoms or molecules can also open an intrinsic bandgap, in hydrogenated graphene, for instance [111]. By intentionally incorporating heteroatoms with different sizes and electronegativities when compared to C atoms, the atomic configuration on the graphene plane can be rearranged. This in turn induces a polarization of the electronic density at the honeycomb lattice, opening its intrinsic bandgap [73]. However, because of the nature of such processes, disorder leads to a degradation of the mobility [112]. Another path is offered by engineering graphene into nanostructures such as quantum dots (GQDs) [113], nanomeshes (GNMs) [114, 115], and nanoribbons (GNRs), as can be seen in Figure 1.5 [116, 117, 118, 119]. When the size of a material approaches the length of the motion of electrons (inside it), the properties of this material depend strongly on its size and shape [81]. Therefore, by changing its shape and size it is possible to induce quantum confinement and edge-related effects [73]. The lateral confinement of charge carriers in GNRs leads to the formation of an electronic bandgap (Figure 1.6 a) , the magnitude of which increases with decreasing ribbon width [120, 121, 116, 122]. Because the bandgap can vary with the geometric structure of the ribbon, GNRs can be tuned from semimetal to semiconductors. GNR transistors with large on/off current ratios at room temperature were already demonstrated [123], though an additional complication of this approach is that the electronic properties are also strongly affected by the edge termination (armchair, zigzag or mixed) of the GNR [120, 121].

Another method is to apply an electric field on a BLG. A bilayer of graphene, whose valence and conduction bands around the K point have a parabolic shape, is gapless (Figure 1.6 b). If, however, an electric field is applied perpendicular to the bilayer, a bandgap opens around the K point (Figure 1.6 c), an effect predicted by theory [87, 124] and verified experimentally [125, 126].

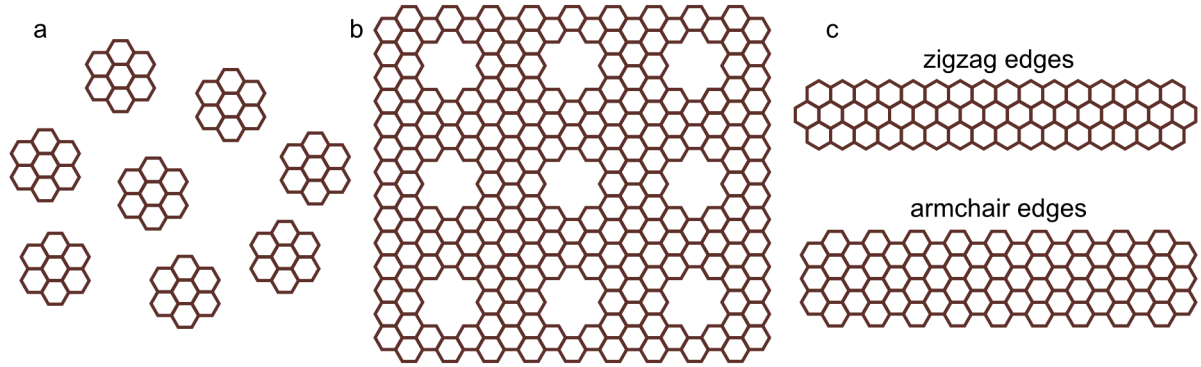

Figure 1.5: Illustration of graphene nanostructures: (a) GQDs, (b) GNMs, and (c) GNRs.

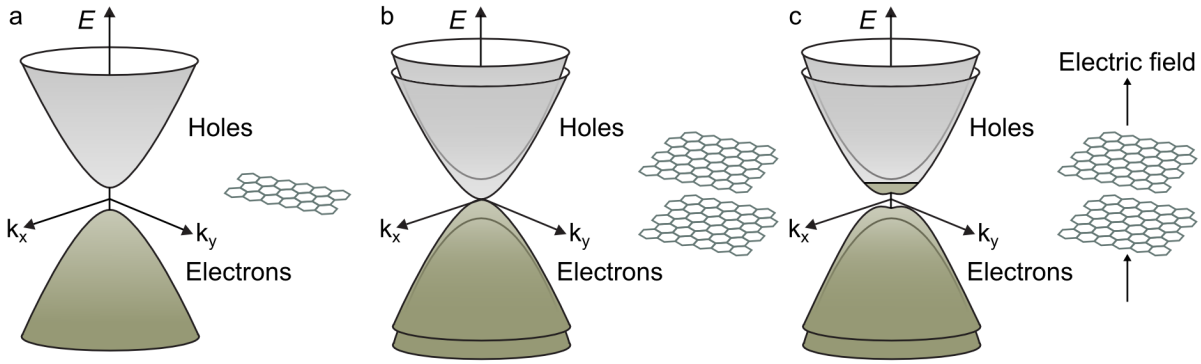

Figure 1.6: Band structure around the *K* point of (a) GNR, (b) BLG, and (c) BLG with an applied electric field. Adapted from [127].

1.8 Fabrication methods of graphene nanoribbons

GNRs can be synthesized by top-down or bottom-up methods. In the former, a large area graphene sheet is modified (e.g., patterned) to a desired nanometric size and shape. In the latter, small building blocks are assembled to construct a larger object.

1.8.1 Top-down

The most widely employed method to fabricate GNRs is oxygen-assisted lithography of graphene sheets (e.g., exfoliated graphene, graphene on metal by chemical vapor deposition or epitaxial graphene on SiC) with different masks [81]. This approach combines a lithography method, such as electron beam lithography (EBL) [128], nanosphere [129], block copolymer [130] or nanowire [131, 132] as a mask patterning technique, with oxygen plasma etching. GNRs patterned by EBL display the narrowest widths ($\sim$ 10 nm [133]) and are the most widely adopted approach for graphene nanostructures, but electronic properties are degraded because the edges are passivated by O- or HO- after etching [116]. Block copolymer as a template lithography method produces low quality GNRs due to a doping effect and impurities. Nanowires with few nanometers in width ($\sim$ 1–2 nm) and smooth edges can be used as a mask patterning, potentially fabricating narrow GNRs. For all these lithography templates, plasma etching is used to remove unmasked areas, leaving behind narrow stripes of graphene, which, due to quantum confinement, display sizeable bandgaps. However, GNR edges tend to exhibit disorder due to the violent nature of oxygen

plasma etching, which greatly reduces the carrier mobility in GNRs produced by this method [81].

A technique that aims to produce smooth and well-defined edges is scanning probe lithography. The edges are tailored with atomic force microscopy (AFM), scanning tunneling microscopy (STM) or transmission electron microscopy (TEM), so that control over the crystallographic orientation as well as the structure is achieved down to the nanometer scale. AFM-based local anodic oxidation lithography fabricates GNRs but is limited by the tip radius and the edge chirality [134, 135, 136, 137]. GNRs with widths as narrow as 12 nm can be obtained by heated AFM tips [138]. STM lithography can pattern GNRs with specific edge chirality by applying a potential bias and moving the tip along the desired crystallographic direction in unwanted graphene areas. With this method, widths down to 2.5 nm and energy gaps up to 0.5 eV are obtained [139, 140].

Another top-down fabrication technique that does not uses patterning masks is hydrogen-assisted etching. At elevated temperatures, particles of a catalytic metal such as Ni, Fe, and Co deposited on a graphene flake cut out graphene nanostructures in the presence of a hydrogen atmosphere by dissociating C-C bonds [141, 142, 143]. When the cutting paths of the particles run parallel to each other, GNRs as narrow as 10 nm with well defined edges are produced [141]. GNRs produced by this method have residues of metal particles, which results in lower electrical performance [81]. This technique can also occur without the assistance of catalytic nanoparticles. Anisotropic etching of graphene via facile H-plasma etching produces GNRs with widths down to 6 nm and high carrier mobility [up to $\sim$ 3 000 $cm^2/(V\,s)$ for monolayer GNR on h-BN] [144, 145, 146].

A large degree of control over large quantities of GNRs with defined size distribution can be obtained with chemical methods. Graphite or carbon-based molecules undergo chemical reactions when placed in appropriate solutions, producing GNR in a powder or a dispersed solution with a low size distribution around 1 nm [147]. Although high mobilities up to 15 000 $cm^2/(V\,s)$ are obtained, GNRs are organized in a network [112]. Alternatively, dispersing carbon nanotubes (CNTs) in a solution with specific chemical agents can unzip their walls [112]. The width of the GNRs produced by this method is determined by the circumference of the CNTs. Narrow width distributions with smooth edges yield high quality samples, but it is difficult to obtain GNRs with well-defined edge structures, since the structure depends on the raw CNT, which has many different chiralities [81].

1.8.2 Bottom-up

One of the bottom-up methods to form GNRs is the molecular precursor-based growth, in which a monomeric precursor reacts at the surface of catalytic metals to form GNRs. This approach usually requires two thermal activation steps, which are achieved by annealing the sample at different temperatures [148]. Initially, the precursor is sublimated onto a slightly hot metallic surface to stimulate the production of polymeric chains, a process which was alternatively performed at room temperature [149], then annealing at a higher temperature dehydrogenates the polymer chains resulting in the GNRs. The organic molecules could also self-assembly using a solution mediated method, which yields GNRs longer than 200 nm (the longest GNRs for self-assembly molecules) [150]. However, because GNRs are fabricated in metal substrates, this method requires a post-synthesis transfer to other substrates for device fabrication.

Chemical vapor deposition (CVD) is a powerful approach to grow MLG on catalytic metal substrates, such as Co, Cu, and Ni [**?** **?**]. Steps or twin boundaries on the metal substrate stimulate GNR growth. A metallic template acts as a catalyst for the decomposition of hydrocarbons that, at high temperatures (between 700 and 1 000 °C) break C-H bonds and form graphene [112]. The size and shape of the GNRs is limited by the template, and transfer methods are required for subsequent transport measurements. One example of a template is a Ni nanobar evaporated

on a SiO_2/Si substrate [**?**]. By exposing the substrate to a hydrocarbon at high temperature, GNRs are formed on the nanobar. Ribbons as narrow as 20 nm with high carrier mobility up to 1 000 $cm^2/(V\,s)$ are obtained with a similar method [**?**]. When using a h-BN substrate, widths between 15 and 150 nm were obtained [**?**]. Because of the atomically smooth h-BN surface, an effective reduction of charge impurities and phonon scattering leads to ultra high quality of the GNRs, which exhibited carrier mobility up to $\sim$ 20 000 $cm^2/(V\,s)$ at low temperature or $\sim$ 4 000 $cm^2/(V\,s)$ at room temperature [**?**].

It is a challenge to combine control over the precise location of the GNRs, over the width, direction and edge smoothness of the ribbons, and direct growth on an insulating substrate. The epitaxial growth of sidewall GNRs on crystalline 4H/6H-SiC(0001) substrates represents a solution to those issues [90]. The direct synthesis of GNRs on an insulating template is beneficial for fundamental investigations of their properties, as well as for applications, in particular due to the possibility to tailor the dimensions of the GNRs [151]. Artificial trenches are etched with photolithography at predetermined locations and, at a high annealing temperature, the trenches sidewall crystallize into stable SiC facets due to SiC step flow. When heated in a vacuum or in an inert gas atmosphere, graphene grows selectively on the sidewalls, since Si sublimates preferentially at the SiC steps and the remaining C atoms rearrange as a graphene layer [23, 14]. The resulting sidewall GNRs have smooth edges that merge into SiC or into the BL. The self-organized growth of GNR on a templated SiC substrate was first demonstrated by Sprinkle et. al in 2010 [90], in a method which did not require damaging post-processing (Figure 1.7). In the study, 10 000 top-gated graphene transistors were fabricated on a 0.24 cm^2 SiC chip, the largest density of graphene devices reported at the time. GNRs as narrow as 40 nm were obtained at specified positions on the substrate, and mobilities up to 2 700 $cm^2/(V\,s)$ were measured at room temperature. This fabrication method has shown exceptional ballistic transport properties, with electronic mean free paths up to 15 μm in a single electronic channel [106], surpassing the theoretical predictions for perfect graphene by at least one order of magnitude [48]. Additionally, bandgaps of up to 1.3 eV indicate that the GNRs are electronically isolated, which corroborates their potential for future graphene-based nanoelectronics [152].

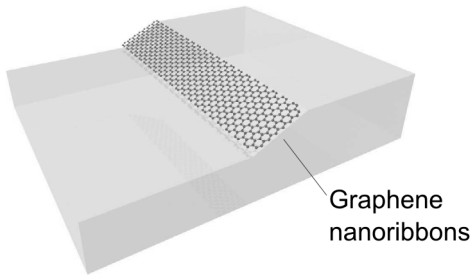

Figure 1.7: Self organized GNRs form on the SiC facet. Adapted from [90].

The morphology of the epitaxial graphene grown by this method is influenced by the SiC structure underneath it. The SiC substrate miscut angle originates a stepped surface which is maintained during standard growth conditions [95, 153, 154, 92, 155]. The preferential sublimation of Si from the step edges [156] allows a selective growth of the GNRs on the SiC nanofacets that does not require any further post-processing [90]. Due to its appealing transport properties and the scalability of the fabrication method in a wafer scale, GNRs grown by self-assembly stands out as potential candidates for graphene devices of high electronic performance [152]. The growth and characterization of monolayer GNRs will be addressed in Chapter 3.

1.9 Bilayer graphene nanoribbons

As established in Section 1.7, the lack of a bandgap in graphene sheets makes them unsuitable for room temperature transistors with sufficient on/off ratios for digital electronic or photonic applications [157, 158]. Among the strategies to solve this challenge is the aforementioned lateral constriction and confinement of charge carriers achieved in GNRs, GNMs or GQDs, in which the transport gap is inversely proportional to the conducting channel width. Typical on/off ratios up to ~ 100 were achieved with this approach [159, 114, 113]. Another method to induce a bandgap in graphene is to apply a vertical external electric field in a BLG. It has been demonstrated that BLG films exhibit a tunable bandgap under an external electric field [125, 87, 160, 126], and that BLG FETs achieve an on/off ratio up to ~ 100 at room temperature [161].

Typical on/off ratios are larger than 1 000, so each of these strategies alone are not large enough for logical applications. Therefore, by combining the properties of BLG with the ones of GNRs, it is possible to fabricate new devices that explore the features of this system, such as improved on/off current ratio [162] or strong electrical noise suppression [163]. Theoretical studies initially predicted that a vertical electric field could further modulate the bandgap in bilayer GNRs, due to the combination of the lateral carrier constriction and the vertical inversion symmetry breaking in bilayer GNRs [164, 165, 166]. On/off ratios up to 3 000 were obtained at room temperature by applying a vertical external field [162], 30 times higher than the maximum value of ~ 100 previously reported for BLG devices [161].

Following the pioneer work of Sprinkle [90], the fabrication of bilayer GNR in SiC was also demonstrated. The growth and characterization of bilayer GNRs will be addressed in details in Chapter 4.

1.10 Possible applications for graphene nanoribbons

Graphene is an ideal material for sensors, due to its ultrathin thickness, large specific surface area, extremely high electron mobility, and high sensitivity to electronic perturbations from foreign molecules [107]. In fact, simulation results for DNA and gas sensing applications anticipate that FET sensors with a single GNR will have higher sensitivity as well as spatial resolution in comparison to other structures [167]. Graphene-based FET biosensors can be used for quantitative measurements of biomolecules, achieving a good low limit of detection. It is therefore an ideal candidate for rapid detection of biomolecules with low concentration or real-time detection of biomolecules [107].

Because of its semiconductor characteristics, GNRs could also compliment semiconducting Si for transistors and other photoelectric devices [127, 168]. Charge transport is favored in GNRs due to its excellent conductivity and tunable bandgap, creating a good solar light response. Therefore, photoelectrochemical devices are another potential application [169, 170].

To integrate ribbons into devices requires junction and heterojunctions [112]. An example of an all-graphene p-n junction assembled different molecular precursors and connected GNRs with p- or n-doping in a continuous GNR [169]. Since epitaxial graphene is conducting and GNRs are semiconducting, regions with a bandgap at the top of curved, sidewall GNRs connected to the conducting facets are another example of an all-graphene semiconductor-conductor junction [171, 172].

2 Experimental procedures

This chapter presents the growth and characterization methods employed to fabricate and analyze the samples studied in the following chapters. It is useful to have a general knowledge of such techniques before exhibiting the results themselves so that a better understanding of the study can be achieved.

2.1 Graphene growth by surface graphitization of SiC(0001)

The equipment as well as the different procedures involved in the fabrication of GNR on SiC are described in this section. More details about the growth mechanisms of GNRs on SiC will be explained in Chapter 3.

2.1.1 Components of the furnace

The fabrication of graphene samples takes place in a radio-frequency (RF) induction furnace (depicted in Figure 2.1), whose designed was based on another system described elsewhere ([173]). It consists of a quartz tube in which a graphite crucible holds the sample in the center of the tube. A graphite fiber acts as thermal insulation between the heated crucible, which reaches temperatures up to 1 600 °C, and the walls of the tube. The crucible is inductively heated by a RF coil externally positioned around the tube. A power supply produces up to ∼12 kW of heating power, which translates into heating ramps of ∼ 8 °C/s. The temperature inside the crucible is measured by a pyrometer pointed toward a hole in the crucible, in an attempt to obtain the temperature closest to the surface of the sample. A controller that uses the difference between a setpoint and a measured value to apply a correction based on proportional, integral and derivative terms is called a PID controller. This device allows the pyrometer to adjust the output from the power supply and therefore the temperature in the crucible. Two ventilators placed underneath the RF coil secure the tube from being damaged by the high temperatures.

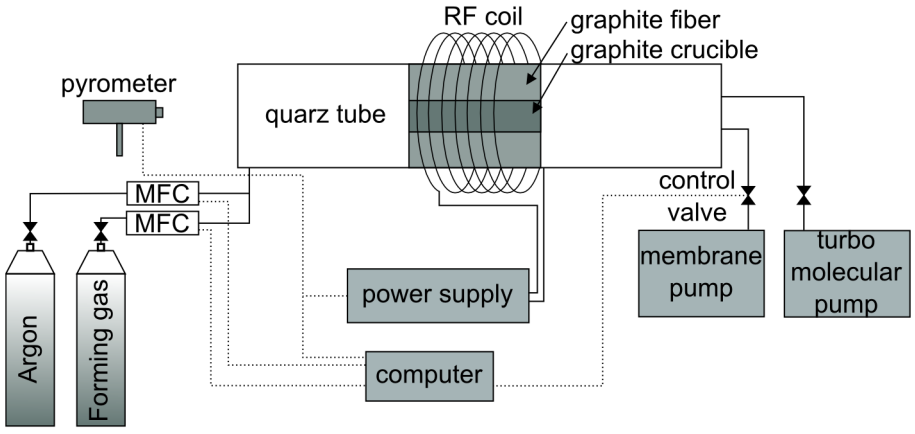

Figure 2.1: Schematic of the furnace used for the synthesis of epitaxial graphene on SiC. The dashed lines correspond to the automated processes. Adapted from [174].

Two different pumps provide control over the pressure during the distinct processes and allow a vacuum of down to $\sim 10^{-5}$ mbar. A turbo molecular pump is used for high-vacuum processes, whereas a membrane pump reaches a rough vacuum and is used in higher pressure processes. A control valve connects the membrane pump to the reactor and allows for the adjustment of the pressure inside the tube when there is a constant gas flow. The two gases that can be flushed through the furnace are pure argon and forming gas (FG, a mixture of 5 at. % H_2 and 95 at. % Ar), whose fluxes are controlled by mass flow controllers (MFC). When loading or unloading a sample from the furnace, the system is vented with nitrogen. A computer program controls all the components of the system.

2.1.2 Hydrogen etching

Initially, each SiC sample is chemically cleaned with n-Butyl acetate (10 minutes), acetone (5 minutes) and isopropanol (5 minutes) under ultrasonication in order to remove the protective photoresist layer and any other organic residues from the SiC surface. They are afterwards dipped in deionized water and blow-dried with high-purity nitrogen.

The subsequent procedure, namely H etching, removes surface contaminants and irregularities, and results in step bunching. For this, the sample is loaded in the furnace (described in Section 2.1 on the preceding page) and pumped until a pressure in the order of 10^{-4} mbar is reached. To ensure that water and contaminations are desorbed from the sample surface, the graphite crucible is heated to 800 °C for 10 minutes.

The H etching process takes place by initially filling the quartz tube with Ar at a flux of 500 sccm (standard cubic cm per minute) until the pressure reaches 900 mbar, at which point, the temperature is raised from 800 °C to 1 400 °C. Once the final temperature is reached, the gas is switched to forming gas (5 at. % H_2 and 95 at. % Ar) while pressure and flux are kept constant for 15 min. By the end of this period, the gas is switched back to Ar and the furnace is turned off, until the temperature reaches room temperature (about an hour later), when the system is pumped again and the sample can be removed after N_2 venting.

After two etching processes the furnace is cleaned in order to avoid an excess of Si in the sample holder, which may contaminate the subsequent growth of GNRs. The cleaning is performed by outgassing the system in vacuum at 800 °C for 10 minutes, followed by another 10 min at 1 600 °C. After this period, the tube is filled with Ar at a flux of 500 sccm until a pressure of 900 mbar is reached, at which point the temperature is kept constant for 50 minutes. The furnace is then turned off until room temperature is reached.

2.1.3 Growth of graphene

The fabrication of graphene itself occurs in a similar fashion as the H etching process, but instead of forming gas, the whole growth takes place in an Ar atmosphere. The sample is likewise loaded in the furnace, which is pumped to ensure no contaminations interfere with the growth process, and subsequently filled with Ar. However, once the desired growth temperature is reached, there is no switch of gas and a constant Ar flow of 100 sccm is kept for 15 minutes, when the furnace is then turned off. Once the system reaches room temperature, the sample can be removed.

2.1.4 Air annealing of graphene samples

In a resistive oven, different from the oven used for graphene growth, oxygen intercalation of the graphene and GNR samples was performed in air for different durations of time at 600 °C, with a preceding heating ramp of 50 °C/min. A hood placed on top of the sample isolates the area being heated, so that there is no flux of air during the annealing.

2.2 Patterning of samples

The growth of graphene on SiC(0001) natural steps highly depends on the morphology of the substrate (which in turn alters from wafer to wafer), as will be shown in Chapter 5. In an attempt to obtain more control over the growth of GNRs, templated SiC(0001) substrates were also utilized. As previously described in Section 1.8, Si sublimates preferentially from the fabricated sidewalls, offering a more selective growth of the GNRs on SiC. The fabrication of such templated samples, performed by Dr. Abbes Tahraoui and Walid Anders, occurred by means of EBL, which will be described next.

In a cleanroom ISO 4, the procedures for patterning of the SiC(0001) are as follows:

1. Samples are clean with 2-Propanol in an ultrasonic bath for a few seconds, followed by N_2 blow to dry any droplets.

2. In order for the resist to be fixed onto the sample, 2 droplets of hexamethyldisilazane (HMDS) are placed on top of the surface of the sample, which is then spun for 45 seconds at 4 000 rpm, followed by a 1 min exposure to a hotplate at 150 °C.

3. Once the sticking layer of HMDS covers the sample, a negative electron beam resist (AR-N 7520-18 1:9) is dropped on top of the surface of the sample, which is again spun for 45 seconds at 8 000 rpm, followed by a 1 min exposure to a hotplate at 85 °C.

4. At this point, the sample is placed on the electron beam system, which is coupled to an SEM to locate the sample. For the electrons to locally remove the resist in accordance to the pattern of our mask, an electron beam energy of 30 kV with 20 μm aperture and an area dose of 80 $\mu m/cm^2$ was used.

5. Once again, the sample is positioned on the hotplate for 1 min at 85 °C to get a better profile.

6. An aqueous developer (AR 300-40 1:5) removes the non-exposed resist after 45 seconds, when the sample is rinsed with water.

7. An inspection in the microscope shows whether it was enough or not, and the sample may be additionally developed for another 10 seconds.

8. Oxygen plasma for 30 seconds in a O_2 pressure between $0.4-0.6$ mbar removes the resist from other undesired areas of the sample.

9. An exposure to plasma treatment of SF_6 (75 W at 1 Pa for 1 minute at 10 sccm) is used to etch the sample.

10. Finally, the sample is cleaned with acetone for 10 minutes, followed by an oxygen plasma treatment for another 30 minutes.

An example of a sample after the patterning process can be seen in Figure 2.2, in which three different magnifications are shown.

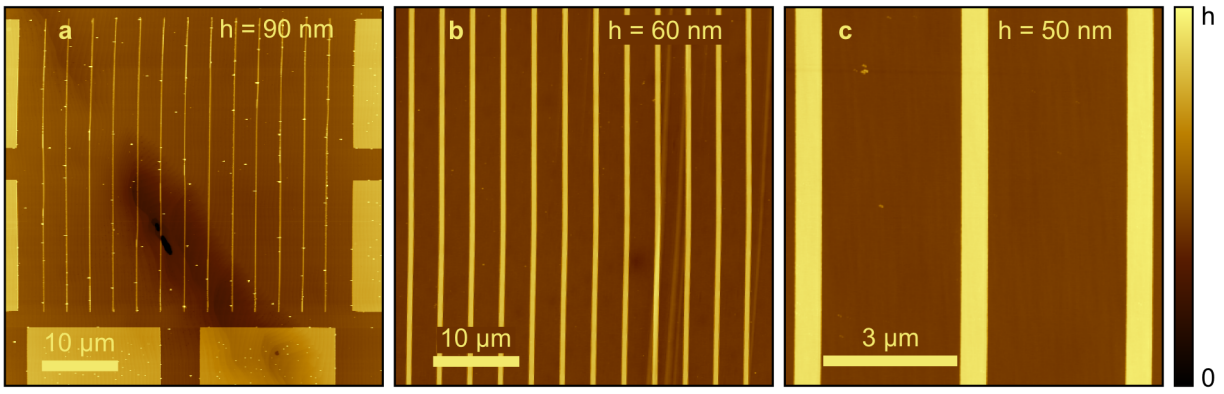

Figure 2.2: SiC sample after the patterning process.

2.3 Raman spectroscopy

Raman spectroscopy is a fast and non-destructive characterization method, which offers high resolution, gives structural and electronic information, besides being suited both at laboratory and mass-production scales [175]. In the study of graphene, it is used to determine the number and orientation of layers, as well as the quality and type of edge [33, 176]. Even though all carbon-based materials show only a few prominent features in their spectra, the position, intensity and shape of each peak gives great insight into these carbon allotropes [175]. This section will present a brief introduction to Raman characterization, followed by a more specific analysis of the Raman spectrum of graphene.

2.3.1 Principles of spectroscopy

Atoms in a crystal lattice always possess some motion around their lattice point, even at absolute zero, due to Heisenberg's uncertainty principle. The fact that there is a motion, even if incredibly small, is what determines thermal and electrical properties of a crystal. If considered isolated, the motion of an atom about its equilibrium position is approximately the same as that of a simple harmonic oscillator [177]. However, since atoms in a crystal are connected, the vibration is disseminated throughout the crystal by means of bonds. The entity in quantum mechanics that represents these vibrations in solids are called phonons and due to their quantum mechanical nature, they can be though of as either waves or particles. Like photons, they can only possess certain values of energy, which are $\hbar\omega$ apart from each other, where ω is their frequency of vibration. Because they are considered quantized packets of vibratory energy, regions of a solid with larger amplitude of atomic vibrations contain more phonons [177]. Due to their particle nature, phonons can be scattered by point defects, dislocations, other phonons, or the surface of a solid.

Physical matter responds in a unique way when exposed to specific frequencies of electromagnetic radiation, i.e., when light interacts with a material, it is absorbed at specific frequencies, depending on the chemical characteristics of that material. This general principle is what allows for most spectroscopic measurements to take place. Unique energetic states in different atoms, molecules, or crystals, create distinct spectral transitions between those states that are responsible for the series of lines observed in a spectrum.

2.3.2 Raman scattering

When using Raman spectroscopy, a laser is focused on the sample and the intensity of scattered radiation is measured as a function of its wavelength. In a Raman spectrum, the intensity is

plotted as a function of the Raman wavenumber ω, which is the difference in frequency (in cm^{-1}) between scattered light and incident electromagnetic radiation (Raman shift frequency) [178]. A measurement gives an estimate of the fundamental vibration modes from different materials and Raman spectroscopy is used therefore to provide a measure of the inelastic scattering of each sample [179].

The Raman scattering effect was discovered in 1928 by C.V. Raman and K.S. Krishnan [180]. The first experiments used the brightest source available, sunlight, or a quartz mercury emission lamp, since lasers did not yet exist. The sources were filtered for specific wavelengths and were used to excite the newly discovered scattering effect. Initially, the necessary exposure time would range from several hours to almost 200 h [179]. Nowadays, laser excitations are able to provide a high density flux of photons in a short period, dramatically reducing the acquisition time.

The Raman effect can be generally understood as the inelastic scattering of electromagnetic radiation. The energy transfer between photons of the radiation source and phonons from the crystal leads to a difference in energy between the incoming and the scattered photon [178]. Once the energy levels of a system are known (or its Hamiltonian), the scattering in this structure can be better understood. Because the laser energy is large compared to the phonon energy for light in the infrared to ultraviolet spectral range [181], the main scattering mechanism does not involve direct photon-phonon coupling, but rather electronic excitations as intermediate states. When a photon collides with a sample, it creates a time-dependent perturbation of the Hamiltonian, which, due to its fast changing electric field, are only answered by electrons. Therefore, how electrons move, interfere and scatter considerably determines Raman scattering on phonons. Consequently, Raman spectra can shed light on the behavior of electrons [182, 183].

To better understand the process of Raman scattering, it is useful to consider a crystal that is illuminated by a photon. The energy of the system, initially in the ground state E_0, is increased by a photon of energy $\hbar\omega_L$, resulting in $E_0 + \hbar\omega_L$, which in general does not lead to a stationary state [184]. Consequently, the system goes to a virtual level, i.e. the electrons are forced to oscillate with a frequency ω_L. Once the photon recognizes that there is no stationary state of energy $E_0 + \hbar\omega_L$, it leaves the unstable situation. The photon is then emitted by the perturbed system, falling back to one of its stationary states. Figure 2.3 shows the possible scattering processes.

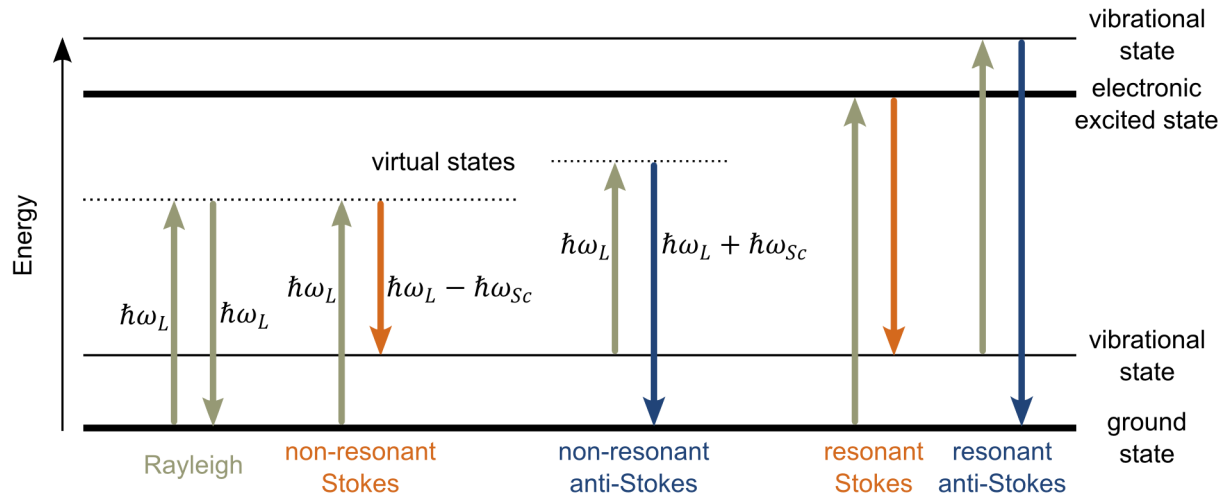

Figure 2.3: Rayleigh and Raman scattering in resonant and non resonant conditions. Based on [184].

The system may return to its initial state in an elastic scattering, or Rayleigh scattering. In this case, the frequency of the emitted photon remains the same as the incident one, changing only its

direction of propagation. When the photon loses or increases part of its energy in the interaction with the system, then the scattering is called Raman. It is an inelastic scattering of photons by phonons [180] and has a much lower probability than Rayleigh scattering. If the transition starts in the ground state and finishes at an excited state, that is, if it loses energy, the process is called Stokes. The photon exits the sample with a lower energy of $\hbar\omega_{Sc}$, and the energy loss of the system corresponds to a phonon energy of $\hbar\omega_L - \hbar\omega_{Sc} = \hbar\Omega$. If the system is in an excited vibration state and, after the interaction with the photon, it returns to its ground level, the process is called Anti-Stokes. The photon leaves the system with energy $\hbar\omega_{Sc} = \hbar\omega_L + \hbar\Omega$. When $E_0 + \hbar\omega_L$ does not correspond to a stationary state, the scattering is called non-resonant. If the excitation matches a specific energy level, the intensities are strongly enhanced and the process is said to be resonant [185].

Because in room temperature most systems are in the ground state, anti-Stokes transitions are less likely [185]. Consequently, a Raman spectrum usually plots the intensity of the Stokes scattered light as a function of the difference between incident and the scattered photon energy, or Raman shift, which is historically plotted in cm^{-1}.

2.3.3 Raman spectrum of graphene

The Raman spectra of graphite was first reported in 1970 in the seminal work of Tuinstra and Koenig [186]. Therefore, by the time graphene's spectra was measured in 2006 [33], Raman spectroscopy was already one of the most popular techniques for the characterization of carbon allotropes, such as fullerenes, nanotubes and diamonds [187]. Graphene differs from usual semiconductors in several aspects, one of which is its linear gapless electronic dispersion around the Dirac point (see Figure 1.3) that implies resonances for any wavelengths of incident radiation [184].

To comprehend the Raman spectra of graphene, it is useful to first understand its phonon dispersion. A dispersion relation, which is the energy or frequency of a photon as a function of its wave vector, $\omega = \omega\left(\overrightarrow{k}\right)$, allows one to obtain the optical and acoustic modes of phonons. The dispersion relation of a crystal with at least two atoms in its primitive cell exhibits two kinds of phonons, namely acoustic (A) and optical (O) modes. Since graphene has two atoms in its primitive cell (as previously shown in Section 1.3), it exhibits the two types of phonons in its dispersion relation. A crystal with more than one atom in its primitive cell will display three acoustic modes, one longitudinal (L) and two transverse (T) [188]. The number of optical modes can be obtained from the equation $3N-3$. Considering that graphene has two atoms in its primitive cell ($N = 2$), there are also three optical modes, similarly one longitudinal and two transverse. The atomic vibrations can occur perpendicular to the graphene plane, i.e. out-of-plane (o) phonon modes, or they can take place parallel to it, or in-plane (i) phonons. In this case, if they are parallel to the A – B direction (Figure 1.1 b), they are classified as longitudinal (L). Similarly, if they are perpendicular to this direction (but still in-plane) they are called transverse (T) [189].

The reciprocal space of MLG and BLG exhibits four high symmetry points within the first Brillouin zone. As can be seen from Figure 1.1 b, those points are: Γ point at the zone center, M points in the middle of the hexagonal sides, and K and K' points at the corners of the hexagons (they are inequivalent since they are not connected by the unit vectors of the reciprocal lattice). Thus, along the high symmetry directions ΓM and ΓK, the six phonon dispersion curves are named oTA, iLA, iTA, oTO, iLO and iTO (Figure 2.4) [189]. However, only a few phonon modes are Raman active and are involved in the creation of the features in the Raman spectra of graphene [188].

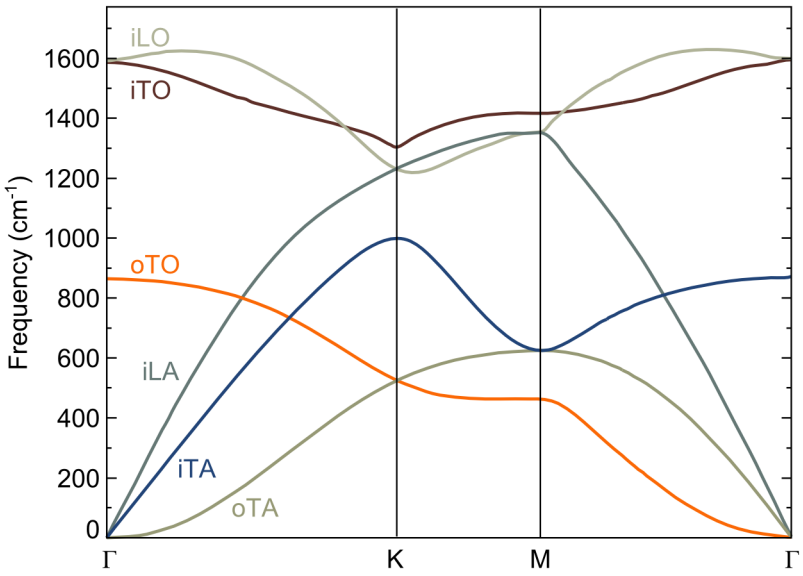

Figure 2.4: Calculated phonon dispersion relation of graphene showing the iLO, iTO, oTO, iLA, iTA, and oTA phonon branches. Adapted from [189] (which was taken from [190]).

Vidano and Fishbach proposed in 1977 the first nomenclature for the Raman spectrum of graphite [191]. Since they observed strong lines in $\sim 1\,580$ cm^{-1} and $\sim 2\,700$ cm^{-1} in pristine graphite, while another band at $\sim 1\,350$ cm^{-1} only appeared in defected graphite, they called the former G and G' (from Graphite), and the latter D (from Disorder). The G' band has later been renamed 2D band [33] (not to be confused with two-dimensional). In this regard, the most notable features of the Raman spectrum of MLG are the G band, which appears around 1 582 cm^{-1}, and the 2D band, at 2 700 cm^{-1}, for a laser excitation of 514 nm (Figure 2.5) [188]. The so-called disorder induced D band can also be seen in disordered samples, at about half the frequency of the 2D band (around 1 350 cm^{-1} for the same laser excitation). Other bands have also been attributed to the Raman spectra of graphene but, since they are not as pronounced, they will not be described in details here. Information can be found elsewhere [175].

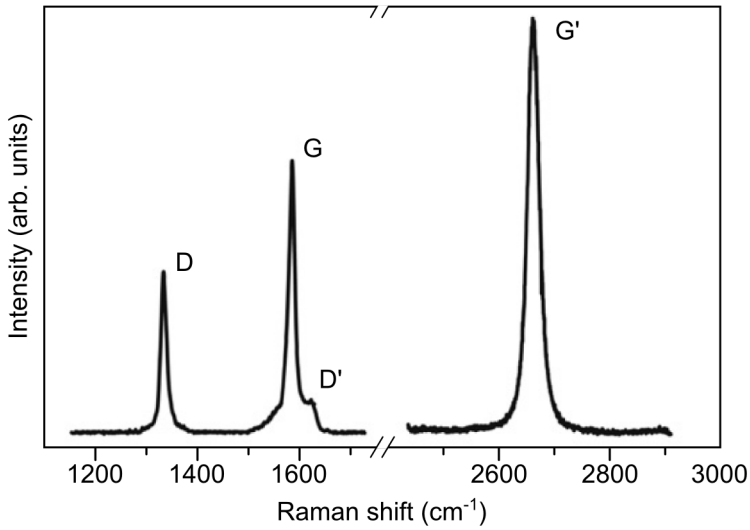

Figure 2.5: Raman spectrum of MLG. Adapted from [188].

The Raman scattering in graphene involves the excitation of an electron into the conduction

band by the absorption of a photon, then scattering of this electron by a phonon or a defect, and finally de-excitation of the electron back to the valence band accompanied by the emission of a photon. The energy difference between the incident and emitted photon is equal to the energy of the Raman active phonon scattering of the electron, which corresponds to a peak in the Raman spectrum. A Raman process may be classified according to the number of scattering events that the photoexcited electron goes through before returning to its initial state [192]. An inelastic scattering process can be originated, for instance, from vibrations of the lattice (phonons), whereas an elastic scattering may arise from defects [188]. Figure 2.6 plots the possible elementary steps of the Raman processes that contribute to each peak of graphene.

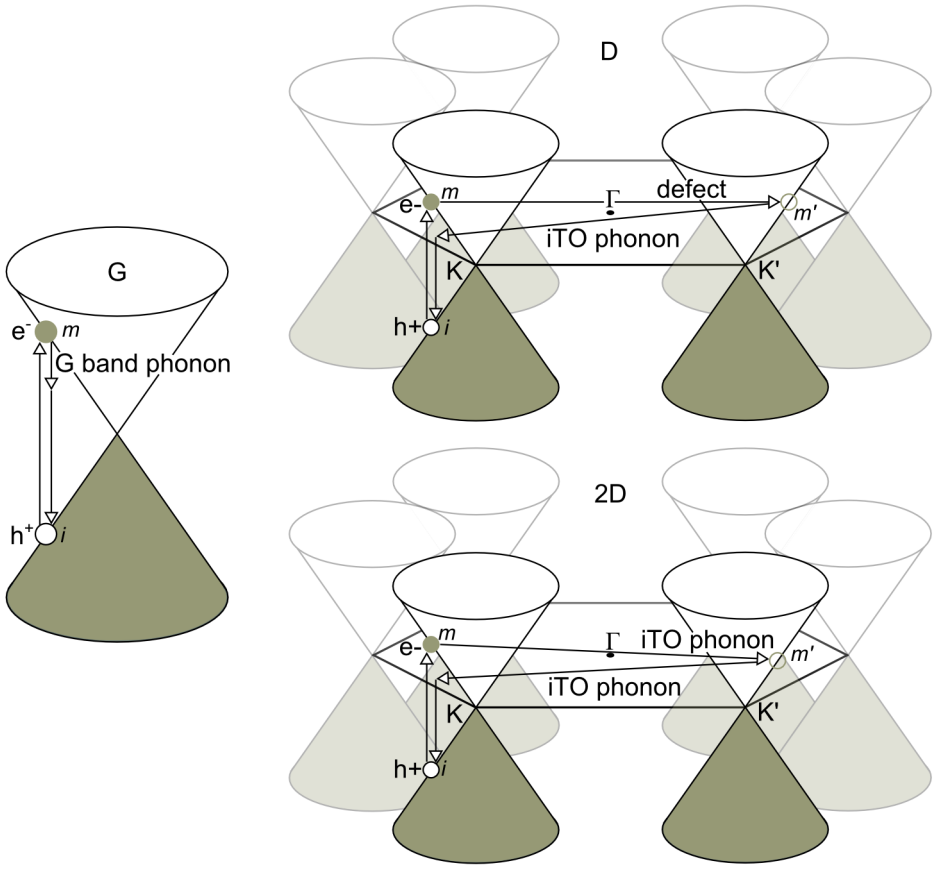

Figure 2.6: Elementary steps of the Raman processes for MLG. Adapted from [188].

The only band that comes from a single scattering process in graphene is the G peak (only one phonon is involved) [188]. It is associated with the double degenerate (iTO and iLO) phonon modes at the Brillouin zone center (Γ point) and it occurs due to the stretching of sp^2 pairs in both rings and chains of the hexagonal carbon lattice [184]. The physical steps involved in this scattering mechanism can be seen in Figure 2.6. An electron with wave vector $\mathbf{k}$ in an initial state i is excited by an incident photon with energy E_L from i to an excited state m. If the m state is a real electronic state, the light absorption is a resonant process. The photoexcited electron will be inelastically scattered by a $q \approx 0$ phonon with frequency ω_q to a virtual state m', and decay back to the initial state i by emitting scattered light [193].

Both the 2D and the D peaks originate from a two scattering process that involves either one iTO phonon and one defect (D band) or two iTO phonon modes near the K point (2D band) [188]. The physical steps can be seen in Figure 2.6. A photon with incident energy E_L excites an electron from an initial state i to an excited state m. Because graphene has no energy gap around the K

point, electrons always have a resonant condition for any laser energy. The photoexcited electron with wave vector $\mathbf{k}$ is inelastically scattered by a defect (D band) or by a phonon (2D band) with wave vector $\mathbf{q}$ ($\neq 0$) to a state $\mathbf{k}-\mathbf{q}$ around the K' point. The electron is scattered back by emitting a (second) phonon with wave vector $-\mathbf{q}$. Finally, the electron returns to the initial state i as it recombines with a hole at the $\mathbf{k}$ state [193].

In the D band, the first scattering process is an elastic event by defects of the crystal, while the second is an inelastic that emits or absorbs a phonon. The D peak occurs due to the breathing modes of six sp^2 atoms in rings [186, 194] and therefore requires a defect in the crystal lattice for its activation [186, 194, 195]. Since the 2D mode originates from a process where momentum conservation is satisfied by two phonons with opposite wave vectors, no defects are required for its activation, and this peak is thus always present on the Raman spectra of graphene [33, 182]. It is characterized by two inelastic scattering events in which two phonons are involved.

Both the D and 2D bands exhibit a dispersive behavior, which means that, depending on the energy of the incident laser, their frequencies in the Raman spectra change. When the laser energy is increased (relative to the Dirac point), the resonance vector $\mathbf{k}$ moves away from the K point. In a double resonance process, as is the case for the D and 2D bands, the corresponding $\mathbf{q}$ vector for the phonon increases with increasing $\mathbf{k}$ (measured from the K point) [188]. Thus, by changing the laser energy, the phonon energy can be observed along the phonon dispersion relations.

2.3.4 Spectra of buffer layer, monolayer and bilayer graphene

As previously explained in Section 2.1, the samples prepared for this study were fabricated on SiC substrates, which has Raman active modes in the area where the spectra are collected (between 1 050 and 3 000 cm^{-1}) [196]. Figure 2.7 exhibits the spectrum of a SiC substrate used in this work, where the two-phonon modes of the SiC substrate can be seen in the region between 1 000 and 2 000 cm^{-1} [197]. Because Raman spectroscopy is a technique sensitive not only to the surface, but it also probes beyond the graphene sheet itself, features from the substrate are also present in the spectra of graphene films grown on SiC [197].

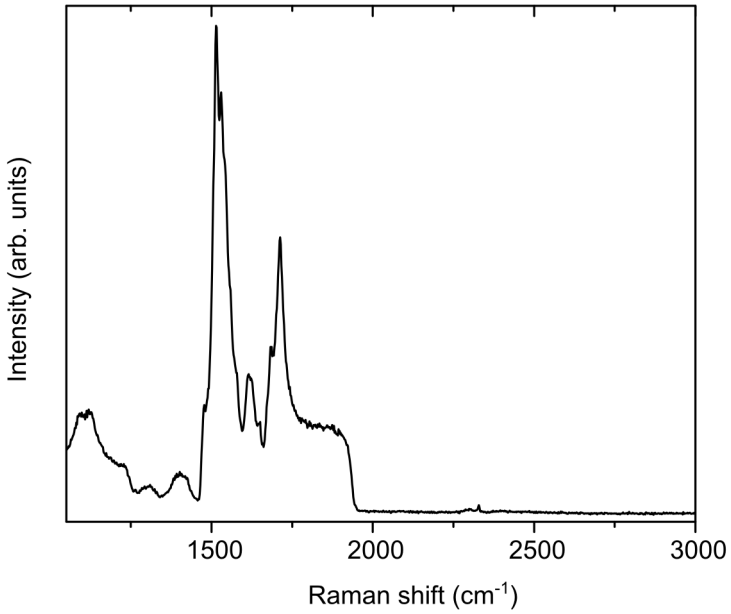

Figure 2.7: Raman spectrum of a SiC(0001) substrate.

As formerly explained in Section 1.6, graphene grown by thermal graphitization of SiC surfaces

exhibits a BL interface. The fabrication of BLG, which was introduced in Section 1.9 and will be described in details in Chapter 4, converts the BL into a second graphene layer, eliminating the contribution from the BL to the Raman spectrum. Therefore, the samples studied in this work contained areas with either only BL, MLG on top of the BL, or BLG (without the BL contribution). Figure 2.8 shows the spectra of the BL, a MLG and a BLG with the background from the SiC. Although the 2D peak is clearly visible around $\sim 2\,700$ cm^{-1} for the MLG and the BLG samples, the spectrum of the underlying SiC substrate is much stronger than the intensity of the the G and D peaks from the graphene films.

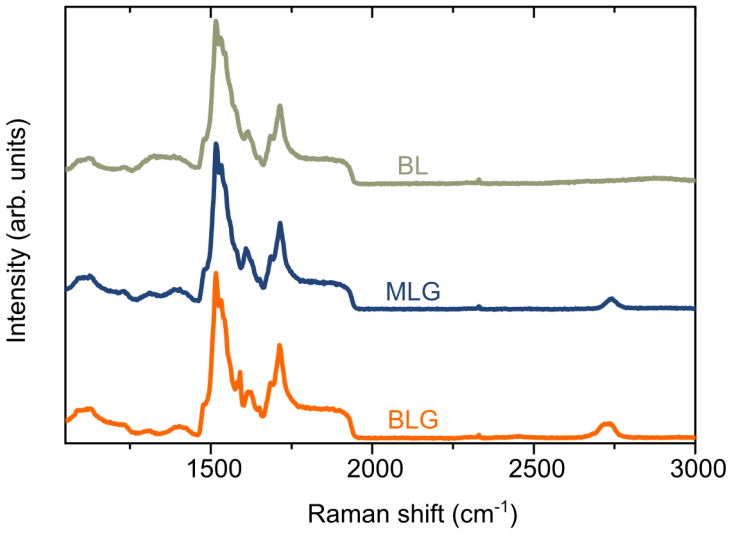

Figure 2.8: Raman spectra of BL, MLG and BLG with SiC(0001) substrate background.

To study the graphene spectra without the background contribution, it is necessary to subtract the SiC spectrum. Figure 2.9 shows the spectra of the BL, the MLG and the BLG after the background removal. The BL spectrum contains two broad features, one centered around $1\,355$ cm^{-1} and the other around $1\,570$ cm^{-1}. *Ab initio* phonon calculations have revealed that these features can be attributed to the vibrational density of states of the BL [197]. The spectrum of MLG also shows the characteristic BL bands, whereas the spectrum of BLG is free from them. Those results are consistent with the fabrication method utilized in this work, since the growth of monolayer GNRs entails the presence of the BL, whereas the fabrication of BLG removes the BL. Additionally, both the spectra of MLG and BLG exhibit the G and 2D band. The 2D band for MLG at room temperature is well described by a single Lorentzian [198] with a full width at half maximum (FWHM) of ~ 40 cm^{-1}. For BLG with Bernal AB layer stacking, both the electronic and the phonon bands split into two components. In this case, four different scattering processes give rise to four Raman peaks in the spectrum of the 2D band. The spectra is therefore fitted with four Lorentzians, each with a FWHM of ~ 24 cm^{-1} [199].

The relative intensity of the 2D to G bands, (I_{2D}/I_G), is decreased in epitaxial graphene (Figure 2.9) when compared to the spectrum of pristine graphene (Figure 2.5). This occurs as a consequence of the intrinsical n-doping of epitaxial graphene on SiC(0001) due to the BL [200]. While the G band intensity is independent of the doping level, the 2D band intensity decreases as the doping level increases (both for hole and electron doping) [201]. Accordingly, (I_{2D}/I_G) changes as the doping level is altered.

A laser excitation wavelength of 473 nm and spatial resolution of ~ 1 μm was used in all the Raman measurements throughout this work. All the spectra which will be later shown had the SiC background signal subtracted. For this, spectra collected from a bare SiC sample from the

same wafer were used as a reference.

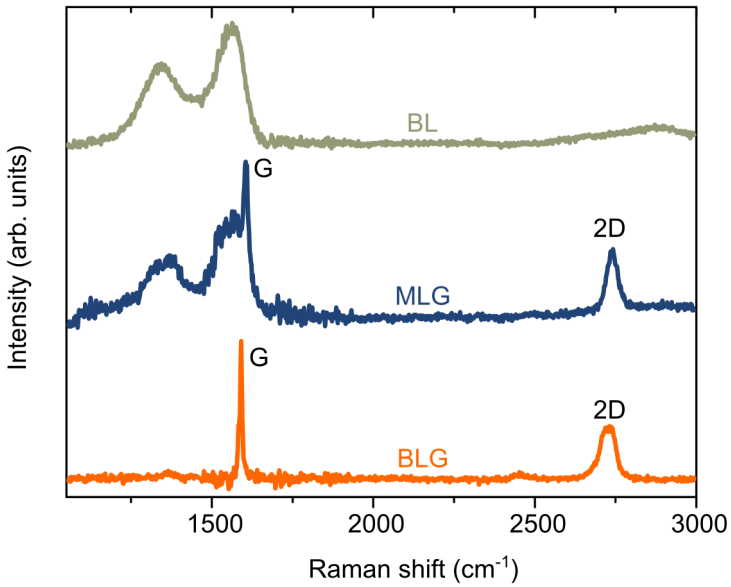

Figure 2.9: Raman spectra of BL, MLG and BLG on SiC(0001) without the background from the substrate.

2.4 Atomic force microscopy

Although a useful technique to study the structure of the surface of samples, Raman spectroscopy is not suitable to obtain information about the surface morphology and individual growth features of the graphene layers. AFM, in contrast, is a more appropriate technique for that.

The first technique to rely on the electron tunneling phenomenon for imaging a conducting surface on atomic scale was the STM, which was built in 1982 by Binnig et al. [202]. The transference of electrons from tip to sample surface involves only a few atoms, thus granting STM sub-angstrom resolution. A real space image on an atomic scale is then built from spatial variations of the tunneling current as the tip scans the sample. Additional features, such as atomic scale defects, which are not seen by diffraction and spectroscopy techniques, are also observed. Those mechanisms make of STM a powerful tool for examining metallic and semiconducting surfaces, which is the reason why it was awarded a Nobel Prize in physics. One of the disadvantages of this technique, however, is that it is unsuitable for insulating surfaces.

As a solution to this limitation, AFM was developed based on the repulsive force between tip and sample surface, which is valid for insulating as well as conducting materials [203]. Unlike other microscopes, AFM does not form an image by focusing light or electrons onto a surface, but rather "feels" the sample surface with a sharp probe [204]. Initially developed for the contact mode, this method forms images by measuring the spatial variation of the tip-sample repulsive force (or their height), producing a high-resolution surface profile. A feedback look keeps a constant deflection (and therefore a constant force) between the tip and the sample by vertically moving the tip. As a limitation, this method may modify the topography of samples with softer surfaces.

The modification of the sample surface induced by the tip can be reduced when using the tapping mode, in which the cantilever vibrates and allows the tip to make intermittent contact with the sample [205, 206]. In tapping mode, the tip oscillates vertically at its resonance frequency [205]. As the sample is approached, intermittent contact is established with the tip, lowering the vibrational amplitude and this drop is used on the feedback. The feedback loop keeps a constant

oscillation amplitude by maintaining a constant root mean square of the oscillation signal. This mode is better for soft surfaces when compared to contact mode because the lateral force between the tip and the sample is greatly reduced and because the short tip-sample contact time prevents inelastic surface modifications. The main elements of an AFM are illustrated in Figure 2.10.

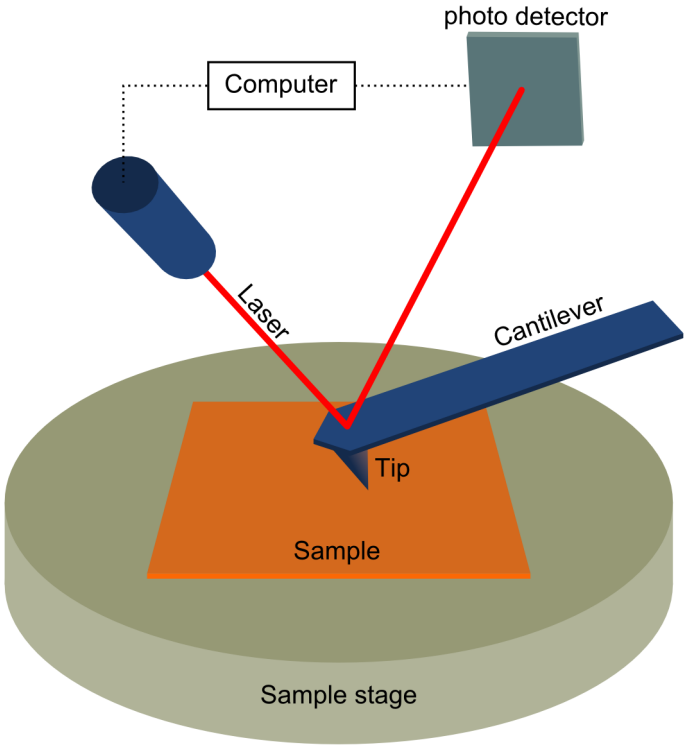

Figure 2.10: Schematics of an AFM.

One of the images obtained with a tapping mode configuration is the phase shift signal. It is one of the most commonly used techniques for characterization of sample surfaces. It measures the energy dissipation involved in the contact between tip and sample [207, 208, 209], which depends on several factors, including viscoelasticity (i.e., the stiffness or softness of a surface), adhesion between tip and sample, and contact area [204]. Since the contact area is altered by slopes on the sample, it also reflects topographic differences of the surface. The phase shift can be understood as a delay in the oscillation of the cantilever, when it moves back and forth towards the surface of the sample (Figure 2.11). As the tip experiences regions of different compositions, the phase signal changes. Brighter and darker areas indicate the various phase shift contrasts in this types of images [210]. In this way, a phase image maps out areas with different materials, since each material is chemically distinct. By capturing both height and phase contrast simultaneously, it is possible to compare topographic structures with material domains.

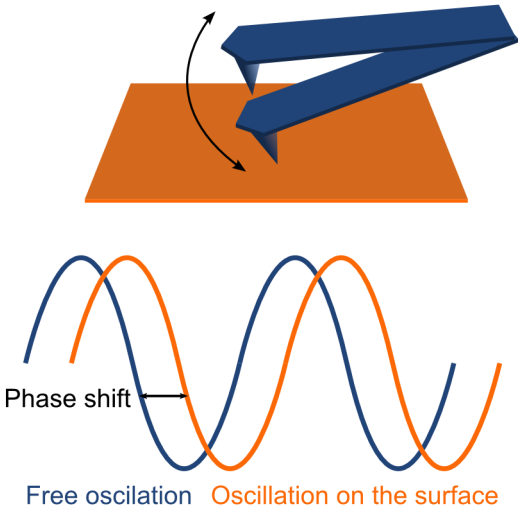

Figure 2.11: Illustration of a tip oscillating (above) and the corresponding response (below) in free oscillation (blue) and on the surface of the sample (orange), exemplifying a phase shift. Adapted from [204].

For graphene samples, the different surface compositions correspond to the SiC substrate, the BL, or graphene layers. An example of a graphene film grown at 1 475 °C for 10 minutes is represented in Figure 2.12 (from [211]). The topography image in Figure 2.12 a shows two pits of similar area on the same terrace. The inset images reveal that the pits have heights of 0.5 nm (b) and 1.0 nm (c) deep, respectively. The phase analysis in Figure 2.12 d exhibits no phase contrast for the 0.5 nm deep pit in comparison to the terrace (e), indicating that both areas display the same material. The 1.0 nm deep pit (f), on the other hand, shows a darker phase contrast, implying that this represents a different material. By combining the information obtained by height and phase contrast, one can conclude that four SiC bilayers were consumed to fabricate graphene. This example illustrates how the phase contrast is extremely useful for the graphene analysis.

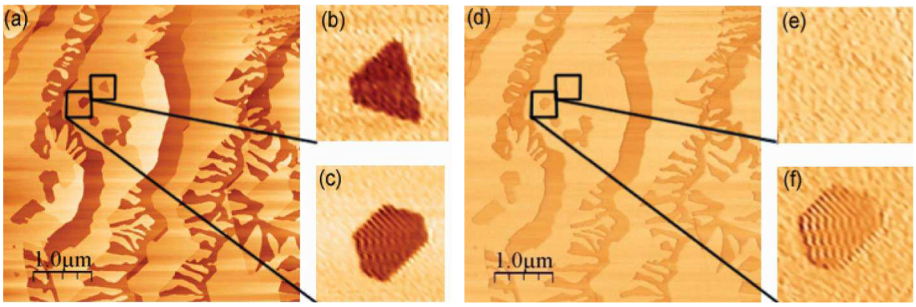

Figure 2.12: Two terrace pits highlighted on the AFM height (a-c) and phase (d-f) contrast images. Taken from [211].

2.5 Transmission electron microscopy

To understand the working principles of a transmission electron (TE) microscope, it is useful to first recall the concept of diffraction. Diffraction occurs when light is allowed to pass through the spaces in an object, similar to the way in which water waves pass through the spaces in between reeds [212]. If a gap is smaller than the wavelength of light the waves cannot pass through, and

therefore diffraction does not occur. According to the calculations from physicist Ernst Abbe's in 1872 on the wavelength of light, this limitation means that the size limit in a light microscope is about 0.5 micrometers, and so the magnification factor cannot be much higher than 1 000 [212].

Electron microscopy was therefore initially developed due to the limited image resolution in light microscopes (imposed by the wavelength of light) and to the need to image detail down to the atomic level in order to better understand the properties of a material. Since electrons are smaller than atoms, researchers wanted to use electrons to built a microscope that could "see" details below the atomic level [213]. The TE microscope operates on the same basic principles as a light microscope, but instead of light, it uses electrons. The limitations imposed by the wavelength of light in a light microscope do not apply to TE microscopes, since electrons have a much lower wavelength, improving the resolution of such microscopes by a factor of up to a thousand. (For an electron with 1 eV of kinetic energy and a rest mass energy of 0.511 MeV, the associated de Broglie wavelength is 1.23 nm, about a thousand times smaller than a 1 eV photon [214].)

The working principle of a TE microscope is similar to a slide projector. In a projector, a beam of light shines through a slide and, as light passes through the structures on the slide, it is affected by them. This results in a selective transmission of light through only certain parts of the slide, which is then projected onto the viewing screen and forms an enlarged image of the slide. In a TE microscope, instead of light it is a beam of electrons that is emitted from the top of the microscope and travels through vacuum towards the sample to be studied [215]. If glass lenses were used to focus the beam, they would impede electrons, therefore magnetic fields are used to converge electron rays into a very thin film and focus them on a sample (instead of the slide projector). The electron beam then shines through the sample and illuminates only the area being examined.

As electrons travel through the specimen, depending on the density of the material, they are either scattered by a variety of processes or they may remain unaffected. Although some electrons are scattered and deviate from the main beam, there is generally less scattering at higher angles so that they are mainly scattered parallel to the incident beam. The TE microscope is constructed to gather the electrons that do not deviate far from the incident beam and, in that way, give information about the internal structure and chemistry of the specimen [215]. The transmitted electrons are projected onto a phosphorescent or fluorescent screen, which is placed at the bottom of the microscope. This screen records a shadow image of the sample, based on the non-uniform distribution of electrons. In the image, different densities are displayed in varied darkness, due to differences in the diffraction conditions of the features on the electron path.

When radiated towards an atom, electrons are capable of removing tightly bound core electrons from the nucleus, thus producing a wide range of secondary signals from the specimen, as illustrated in Figure 2.13. Those signals give chemical and structural details about the sample. Since electrons are (negatively) charged particles, when they interact with the local electromagnetic field of a sample, they are strongly scattered by both the electrons and the nuclei in the material. Because the scattering process varies with the structure or composition of the specimen, it is possible to either image a structure, collect a diffraction pattern, or record a spectrum. Images of the specimen are obtained through investigation of the spatial distribution of scattering, while diffraction patterns are obtained by the angular distribution of scattering. The interaction between the electron beam and the sample results in a change of energy and/or trajectory without altering its kinetic energy.

High-resolution TEM images of typical graphene layers formed on a stepped 6H-SiC(0001) substrate observed along the $[11\bar{2}0]$ direction (electron incidence direction) are shown in Figure 2.14. In all the images, graphene layers (including the BL) appear as a dark line contrast, whereas the SiC substrate appears as a bright dotted contrast. Terraces covered by either one or two graphene layers on top of a BL are exhibited in Figures 2.14 a-b, whereas the initial growth of graphene layers can be observed starting from the step edges in Figures 2.14 c-d.

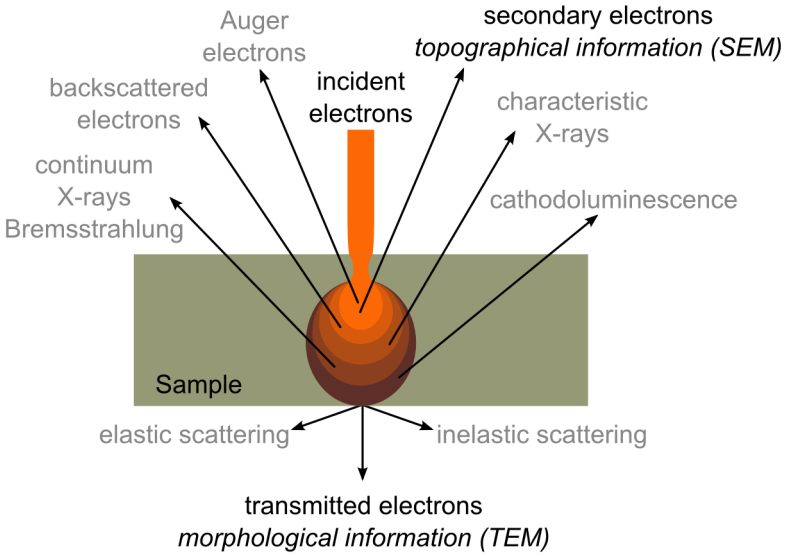

Figure 2.13: Signals emitted from different parts of the interaction of the primary electron beam with the sample. Adapted from [216].

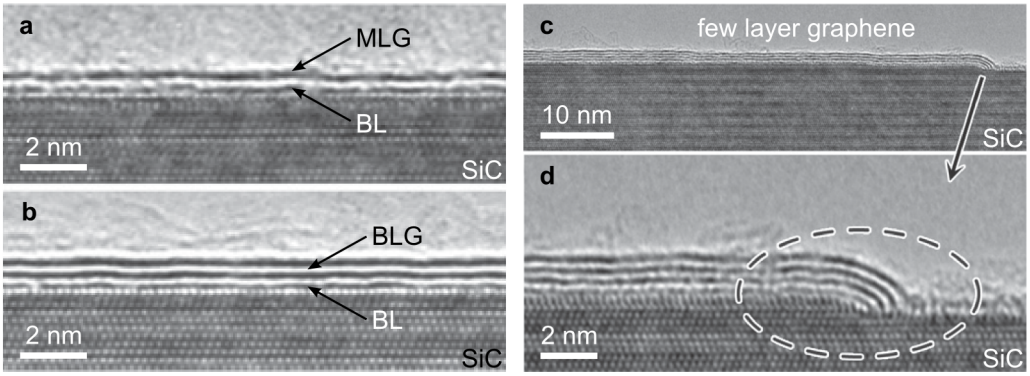

Figure 2.14: High-resolution TEM images of (a) monolayer, (b) bilayer, and (c-d) few layer graphene on top of a BL grown on SiC(0001) at different temperatures (1 350 °C – 1 450 °C) for 30 min. The image in (d) is an enlargement of part of (c). Taken from [217] and [218].

Cross-sectional TEM was conducted by Dr. Katja Berlin and Dr. Achim Trampert in a JEM-2100F operated at 80 kV equipped with a field emission gun. The samples were prepared using standard procedure of mechanical grinding and dimpling. Afterwards they have been thinned by argon ion beam milling with an energy of 4 keV under an incident angle of 4° using a Gatan precision ion polishing system.

2.6 Scanning electron microscopy

Scanning electron microscopy (SEM), like TEM, also relies on electrons to map the object of study, i.e., they're both electron microscopy techniques. Unlike TEM, which measures the electrons that travel through the sample, SEM analyzes electrons that travel back after interacting with the sample. This means that, while in TEM the specimen needs to be thin enough to avoid most electrons to be scattered or absorbed within the sample rather than transmitted, in SEM the specimens can

be relatively thick (what has stimulated the development of this technique in the first place [215]). SEM scans a focused beam of electrons over a surface to create an image. By interacting with the sample, the electrons in the beam produce a variety of signals that give information about the sample, including surface morphology, chemical composition and crystalline structure [219].

The incident electrons are accelerated and focused on the sample, where they go through several scattering processes before leaving the sample. Because they have a lot of kinetic energy, as they interact with the sample they are slowed down and their energy is dissipated as different signals. Besides X-rays, three kinds of electrons are emitted from the interaction, namely primary backscattered electrons (BSE), secondary electrons (SE) and Auger electrons [220]. The main scattered electrons are sketched in Figure 2.13. As the incident electron beam encounters the sample, it is inelastically scattered and ejects electrons from the atoms of the sample. Those are the so-called SE, which are commonly used for SEM. The SE produced from the first scattering processes, SE1, are the ones that offer most information about the sample surface. As the electron beam is further scattered by the sample, it produces more SE, called SE2. There is a third type of SE, SE3, which are generated by the interaction of BSE with other materials in the SEM chamber.

Electron guns, which produce a steady stream of electrons (incident electrons), are located either at the top or bottom of the microscope (so that micromechanical movements of the components due to the gravitational force do not affect the alignment with time). Like optical microscopes, SEM uses lenses that, instead of glass, are made of magnets which focus and control the electron beam. The sample to be examined is placed in a sample chamber insulated from vibrations. The position of the electron beam on the sample is controlled by coils that allow the beam to scan the surface of the sample. Different detectors register the various types of interactions of the electron beam within a defined area of the sample. As the electron beam traces over the sample and interacts with its surface, it penetrates a few microns, depending on the accelerating voltage and density of the sample. SE are removed in a unique pattern, and, depending on the number of electrons that reach the secondary electron detector, different levels of brightness are registered. Additional sensors detect BSE (reflected from the sample's surface) and X-rays (emitted from beneath the sample's surface). An image of the original object is created dot by dot, row by row, giving information about the collected area. In order for the electron beam not to be obstructed from the path towards the sample, it is important that all those elements of the microscope be immerse in vacuum [215].

Two detectors are responsible for the detection of the SE [221]. One is called Everhart-Thornley and is placed outside the lens system with an inclined angle relative to the incident electron beam. As a positive bias is applied to this detector, SE1, SE2, and BSE are attracted. Those emitted electrons offer information about the depth and topography of the sample. The incident electron beam has a higher penetration depth in materials that are extra-thin and have a low atomic number (like graphene), which results in electrons (SE1, SE2 and BSE) escaping the surface from a larger area. This in turn generates blurry images recorded by this detector. The other detector, called In-Lens, is placed inside the lens column, perpendicular to the incident electron beam. This detector effectively captures electrons from the SE1 type due to its position and the electrostatic/electromagnetic lenses that select only SE1 toward it. By using a In-Lens detector combined with a low acceleration voltage, it is possible to reduce the depth of penetration, which implies a higher surface sensitivity [221]. Accordingly, this combination is suitable for imaging of 2D materials like graphene. The SEM measurements were performed with the assistance of Dr. Uwe Jahn and Dr. Carsten Pfüller. The In-Lens secondary electron detector of a Carl-Zeiss-ULTRA 55 SEM operating at an acceleration voltage of 3 kV was used throughout this study.

An example of an In-Lens detector SEM image of a graphene sample is shown in Figure 2.15, in which graphene (darker contrast) differs from a bare Ni substrate (brighter contrast). Opposed to this image, the substrates utilized along this study were either semi-insulating or doped SiC. To

avoid the contamination promoted by the electron beam in semi-insulating substrates, which happens for long acquisition times or when the selected area is too small and the beam is, therefore, more focused, a silver paste was used on those substrates.

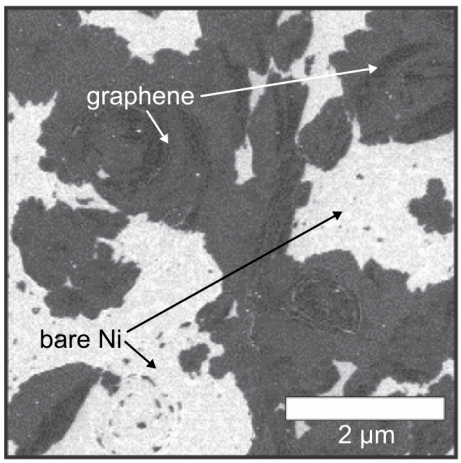

Figure 2.15: In-Lens detector SEM image of a graphene film on Ni-MgO(001). The dark regions are graphene, while the lighter areas are bare Ni. Taken from [222].

2.7 X-ray photoelectron spectroscopy

X-ray photoelectron spectroscopy (XPS) is a widely used surface analysis technique, since can be applied to a broad range of materials and provides useful information from the surface of the studied material, such as composition, chemical state of the elements and chemical bond strengths [**?**]. The technique is based on the photoelectric effect, in which the surface to be studied is exposed to light (in this case, a beam of x-rays) and, as a result, electrons are emitted from the material [**?**]. The energies of the photoelectrons that leave the sample, characteristic of each element, are then measured and the peak areas can be used to determine the composition of the surface of the material [**?**]. Initially, a survey (or wide) scan is performed from binding energies between 0 and 1200 eV to inform about the elements present in the sample by counting the number of photoelectrons over this wide range of energies. The obtained intensity is typically plotted as a function of electron binding energies [**?**]. Narrower scans focusing on a specific peak or set of peaks elucidate the chemical state or environment at the surface [**?**]. The binding energy of the photoelectron peaks identify the elements and their chemical state on the surface, whereas the intensity of the peaks quantifies the composition ratio of the surface elements [**?**].

An example of an XPS measurement from a pristine monolayer graphene on SiC(0001) is shown in Figure 2.16, which displays the C 1s and the Si 2p core level spectra of this sample. The spectrum in the C 1s region exhibits four components, one at 284.8 eV related to the carbon bonded within the graphene layer, the SiC bulk component at 283.9 eV, and the BL components S_1 (285.0 eV) and S_2 (285.7 eV) [223]. The lower energy component S_1 is related to the covalent bonds between the BL and the SiC surface, while S_2 is due to the sp^2 bonded carbon within the BL [101]. The spectrum of the Si 2p region was fitted with two components, labeled SiC bulk and Si_C, corresponding to silicon in the SiC bulk and silicon at the SiC surface bonded to carbon within the BL, respectively.

The XPS measurements presented in this work were obtained in collaboration with Dr. Muhammad Y. Bashouti, from the Ben-Gurion University of the Negev. They were aquired in UHV using an x-ray photoelectron spectrometer with an Al Kα x-ray source and a monochromator. The x-ray analytical spot diameter was $\sim$ 500 μm and survey spectra were recorded with a pass energy of

20 eV.

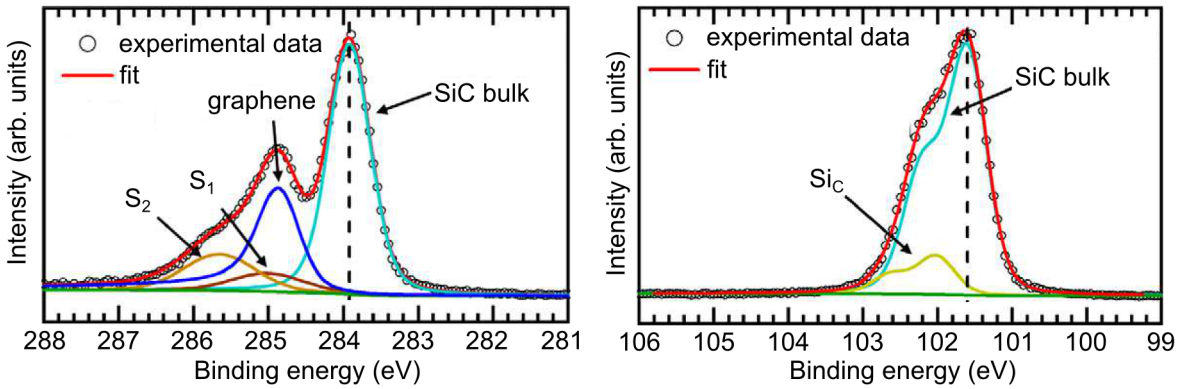

Figure 2.16: (a) C 1s and (b) Si 2p core level spectra of pristine monolayer graphene. Taken from [223].

2.8 Transport characterization

Electronic transport of the bilayer GNRs were measured in collaboration with Johannes Aprojanz, Dr. Ilio Miccoli, Dr. Timo Lichtenstein and Dr. Christoph Tegenkamp from the Leibniz Universität Hannover. This characterization technique can give information about mobility and carrier concentration on bilayer GNRs. Their 4-tip STM/SEM system, in which the samples are degassed for several hours at 700 °C, operates at a base pressure of 1×10^{-10} mbar. The high resolution of a scanning electron microscope allows a precise control over the position of the tips for transport measurements. Ohmic contact with the samples is established by tungsten tips, which are made by electrochemical etching with NaOH. The measurements were made either in a two-point probe (2PP) or a co-linear 4-point probe (4PP) configuration, the former due to its simplicity and the latter to verify how clean the tips were, giving rise to negligible contact resistances [224]. If the contact resistance exhibited too much fluctuation, the 4PP system was preferred.

The following procedure was adopted to obtain the mobility and carrier concentration of the samples. The SEM system is first used to search for the best areas of the sample to measure. Then either four or two STM tips are approached, depending on the configuration to be used, and brought into tunneling contact above the SiC substrate and in between the ribbons. Once tunneling occurs, to ensure that the distance between the tips and the sample is kept constant and the tips don't collide, the current between them varies as the tips are positioned on a ribbon. At this point, the feedback loop was turned off and I(V) curves were recorded. By moving the tips along the ribbons and performing I(V) measurements on different points, it is possible to learn whether the ribbon is diffusive or not, and if it has a 1D or a 2D behavior.

Figure 2.17 shows the two configurations used throughout the transport characterization of our samples, i.e., 2PP and 4PP. A GNR is illustrated on a step edge of a SiC(0001) substrate and the probe spacing, L, is shown for each geometry, as well as the corresponding probes. In the 2PP setup (a), both probes serve as a current (i) source and as a voltage (V) probe. When the linear fit of the resistance as a function of the probe spacing intercept the origin, the contact resistances of the tips are negligible and this configuration can be employed. If the 4PP geometry (b) is used instead, while two probes drive the current through the sample, another two probes measure the voltage drop simultaneously [225]. In this case, the current flowing through the voltage probes is practically zero due to the high input impedance of the voltmeter. Hence, the voltage drop over probes and contacts can be neglected and the measured resistance corresponds only to the resistance of the sample.

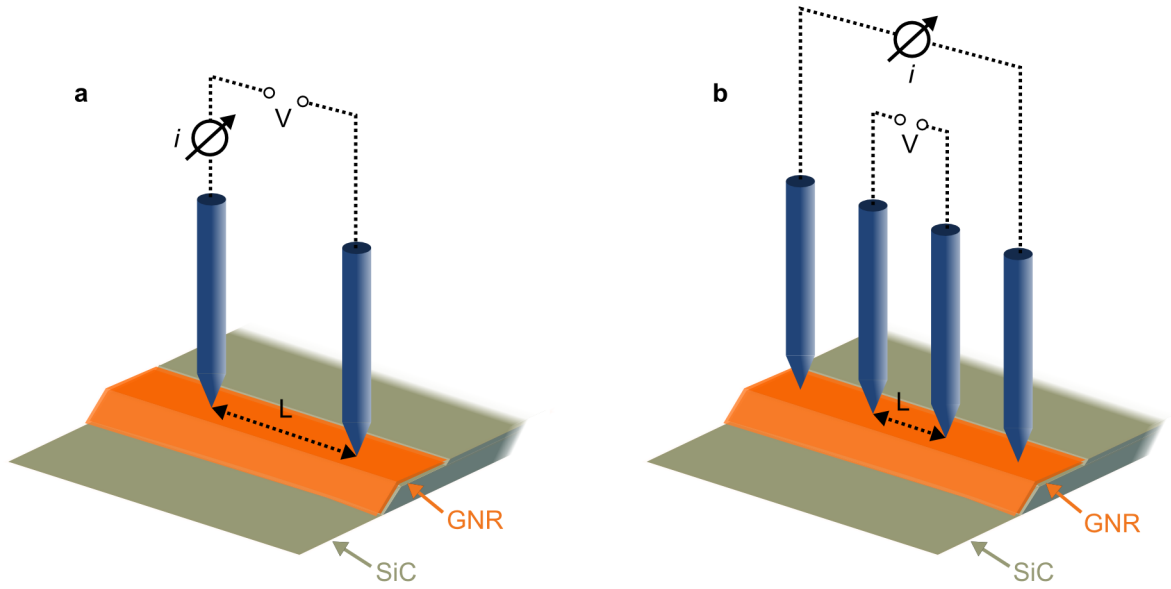

Figure 2.17: Schematic representation of the setup of (a) 2PP and (b) 4PP geometries. Adapted from [225].

3 Monolayer graphene nanoribbons

3.1 Introduction

As previously reported in Chapter 1, one of the proposed methods to induce a bandgap in graphene is to fashion it into quasi-one-dimensional nanoribbons. Therefore, the development of a scalable method that allows the production of GNRs with tailored dimensions and edge termination, directly on a technologically compatible substrate, would be ideal for device applications. Among the different approaches which have been reported [116, 139, 226, 227, 148] – spanning from the lithography patterning of mechanically exfoliated graphene [116] to the unzipping of CNTs [226] – the direct synthesis of GNRs by surface graphitization of SiC is certainly one of the most promising methods to fulfill the above requirements. Controlled, epitaxial growth of GNRs on SiC allows, in principle, the tailoring of both lateral dimension and edge termination [151]. Additionally, it avoids any post-growth process for "cutting" graphene into ribbons, which frequently results in structural damage.

Sprinkle et al. [90] pioneered this method by fabricating GNRs via self-organized growth on well-ordered, non-polar facets created by the surface patterning of the SiC prior to graphene growth. Baringhaus et al. [106, 152] later measured single-channel ballistic transport in monolayer GNRs prepared on the same type of SiC templates. Selective growth of GNRs on non-polar facets of vicinal SiC surfaces has also been achieved by employing chemical vapor deposition and molecular beam epitaxy [227, 228]. Alternatively, as it will be shown in this chapter, natural facets, formed due to step bunching promoted by H-etching, can be used as nucleation centers for ribbons that grow laterally on top of the (0001) terraces. A potential advantage of this approach is more precision in the control over the final width of the GNR, as the formation of MLG on the (0001) surface has been shown to be more readily achieved than on the non-polar $(1\text{–}100)$ and $(11\text{–}20)$ planes [229, 230]. In fact, the unintentional formation of few graphene layers on the non-polar facets of the SiC surface is a general challenge for GNRs grown on SiC, independently of whether step facets are designed as the active region for selective GNR growth, or only as nucleation centers.

In this context, investigating the growth process of GNRs on a stepped SiC surface and the mechanisms through which control may be exerted over the final size of the ribbons is very important to the fundamental understanding of this interesting – and potentially useful – material system. Thus, in order to obtain a direct correlation between fabrication temperature and final ribbon width, samples were grown at temperatures ranging from 1 410 °C to 1 460 °C for a fixed time of 15 min, which was sufficient to form monolayer GNRs close to step edges but without promoting a complete MLG coverage. Two SiC substrates with different miscuts were employed to also evaluate the influence of step height and terrace width on the formation of GNRs.

3.2 Sample preparation

Epitaxial monolayer GNRs were synthesized on n-type 6H-SiC(0001) substrates (1 cm $\times$ 1 cm). In order to study the effect of step height on growth behavior, two main series of samples employed as substrates nominally on-axis (low-miscut, 0.1°) and off-axis (high-miscut, 2.0°) SiC(0001). After each sample was chemically cleaned (as previously described in Section 2.1.2), a process of H etch-

ing removed any surface contaminants and irregularities (e.g. scratches), and led to step bunching and thus the formation of non-polar facets on the SiC surface [231]. The stepped surface is a result from the wafer miscut, which prevents the formation of a perfectly flat surface with a single crystalline face (this happens due to the unintentional miscut of the surface, even for nominally on-axis surfaces [231]).

AFM analysis reveals that, after GNR synthesis, the mean height of the surface step facets ranged from 1 to 3.5 nm for the low-miscut SiC, whereas for the high-miscut samples this value varied between 7.5 and 18 nm. Figure 3.1 shows AFM images which illustrate the overall surface morphology of the SiC(0001) samples used in this work after GNR growth at 1 450 °C for 15 min. No dependence on the GNR growth temperature was observed in either case. Note that some steps are actually formed of several smaller mini-steps with small terraces in between (see arrows in Figure 3.1).

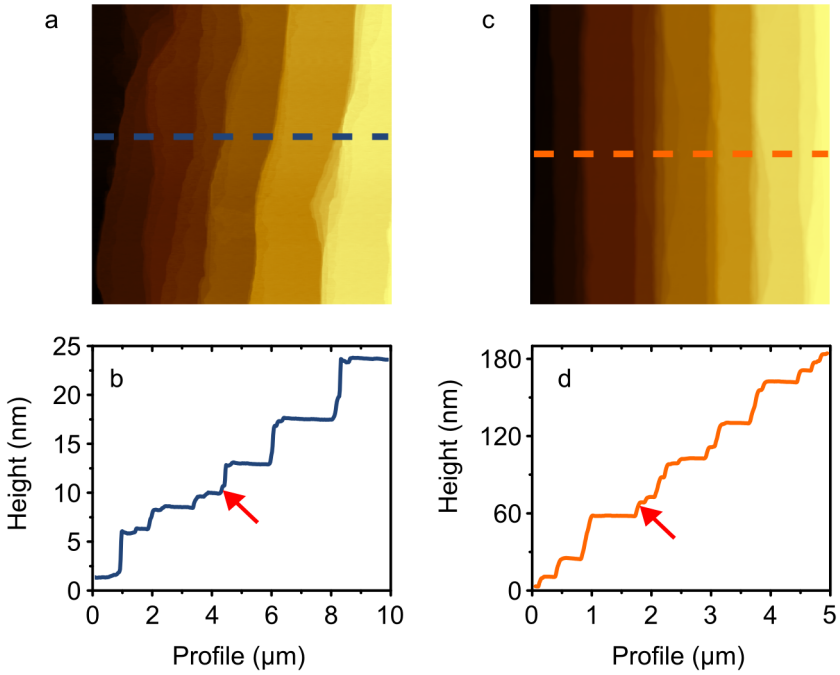

Figure 3.1: AFM height images for a low- (a) and high-miscut SiC (c) and their cross section profiles (b, d), respectively. The arrows in (b) and (d) indicate step edges where the existence of mini-steps separated by small terraces can be seen. The images were taken after GNR growth at 1 450 °C for 15 min.

The fabrication of graphene occurred in a similar fashion as the etching process, but instead of forming gas, the whole growth took place in an Ar atmosphere (as also previously described in Section 2.1.3).

3.3 General concepts of surface graphitization

The growth of epitaxial graphene on SiC(0001) is known to proceed in a layer-by-layer "inversed" mode when sublimation of Si atoms from the SiC surface takes place at high temperatures. Even though the graphitization of SiC surfaces had been observed in 1975 by Van Bommel et al. [23], de Herr and coworkers [14] were the first to produce graphene layers utilizing this method and to show, via transport measurements, the potential of epitaxial graphene as an electronic material.

Because Si has a higher vapor pressure than C [232], as the SiC substrate is heated, Si atoms desorb first from the sample surface [156, 233]. The C atoms left behind at the surface rearrange to form a layer that is isomorphic to graphene with a $6\sqrt{3} \times 6\sqrt{3}$ R30° periodicity [23, 234, 101, 200, 235, 236]. The R30° denotes the 30° angle between this surface reconstruction and the SiC substrate, whereas $6\sqrt{3}$ stands for the size of the new lattice vector, when compared to the SiC [100]. This layer, the one usually referred to "buffer layer" [103], or also zero-layer [237, 32], differs from a single layer of graphene because $\sim 1/3$ of its atoms are in a sp^3-configuration and covalently bound to Si atoms in the SiC substrate [101, 6]. As more Si atoms continue to escape from underneath the BL, a second BL layer is formed below the initial layer. Since the atoms are more weakly bound to the substrate close to the step edges when compared to the terraces, Si atoms desorb more rapidly from such areas [90, 156, 233]. This sequence leads to the decoupling of the first BL from the SiC, which is then converted into a graphene monolayer. The more the new underlying BL grows laterally, the broader the topmost decoupled MLG area becomes. This area is defined as a monolayer GNR. More details on the growth process will be described in more detail later.

3.4 Results

3.4.1 SEM

SEM images for some of the samples are shown in Figure 3.2. The darker contrast is in general related to the monolayer GNRs, whereas the brighter contrast is due to the SiC surface covered by the single $6\sqrt{3}$ BL. Due to the low-miscut angle, the first series of samples possesses surfaces with $1-2$ μm wide terraces (Figures 3.2 a-c), which makes it easier to distinguish individual ribbons in comparison to the case of the high-miscut substrates (Figures 3.2 d-f). The latter has terraces that are usually narrower than 1 μm. Due to this, it is possible to observe areas where the MLG is covering the whole terrace. These areas were not regarded as GNRs and therefore not considered in the statistical analysis shown next. Finally, it can also be seen that the steps of the low-miscut samples are not as straight as the ones in the SiC substrate having higher miscut. This is probably related to a higher misalignment in the (0001) basal plane from both the $<$ 1–100 $>$ and $<$ 11–20 $>$ directions [238]. There is also a clear increase in the spread of the GNR widths observed as the temperature is increased. In order to better quantify this change, a statistical analysis was performed on several SEM images as those shown in Figure 3.2. The statistical analyses were obtained based on 250 measurements of the GNR width for each sample.

The mean value and the standard deviation of the monolayer GNR widths for each sample are plotted in Figure 3.3 a. The larger standard deviation observed in the 1 440 – 1 460 °C temperature range for GNR ensembles in the low-miscut SiC is probably related to the misalignment in the (0001) basal plane leading to a larger width variation and edge disorder as the temperature increases. GNRs synthesized on the high-miscut SiC are on average narrower than those prepared on the low-miscut substrate for every growth temperature. Interestingly, two regimes are observed for the width variation as a function of the growth temperature, one between 1 400 and 1 430 °C, and another for the 1 440 – 1 460 °C range. For the latter, the width shows a weaker dependence on the synthesis temperature.

In order to gain more insight into the mechanisms involved in the growth process, the activation energy required to form monolayer GNRs on both types of substrates was estimated using the Arrhenius equation:

$$\ln k = \ln A - \frac{E_a}{k_B T}$$

in which for a given temperature T, the expansion rate of individual GNRs k (in nm/min) depends on the activation energy E_a. A is a prefactor, and k_B the Boltzmann constant. When plotting

$\ln k \times {}^{1}/_{T}$, a line with a slope corresponding to $-{}^{E_a}/_{k_B}$ intersects the $\ln k$ axis at $\ln A$. As k is the ratio between the mean width of the GNRs and their growth time, it was possible to determine the activation energy of the rate limiting step in the reaction from this value. Since the prefactor does not offer any important physical information for this work, it was not considered in this analysis. Figure 3.3 b shows the results obtained. For GNRs grown on the low-miscut substrate, E_a is 6.1 ± 0.3 eV. For the high-miscut case, the two growth regimes observed yielded two E_a values, 9.2 ± 0.1 eV at lower growth temperatures and 2.0 ± 0.9 eV when a growth temperature near the top of the range was used.

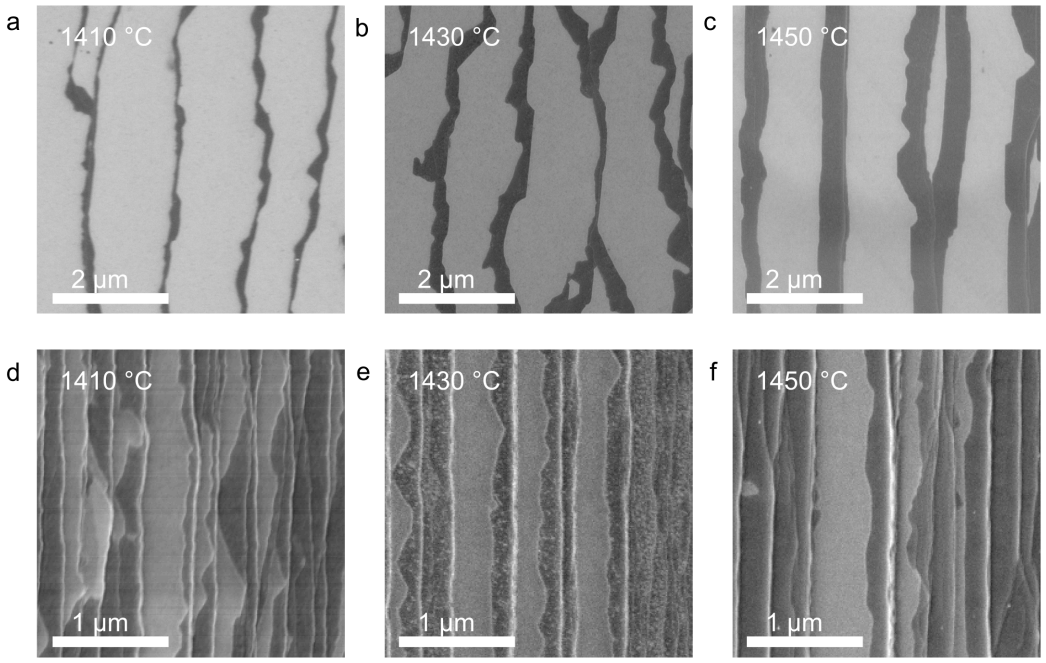

Figure 3.2: In-Lens detector SEM images from monolayer GNRs (darker contrast) grown at different temperatures on low- (a-c) and high-miscut (d-f) SiC substrates.

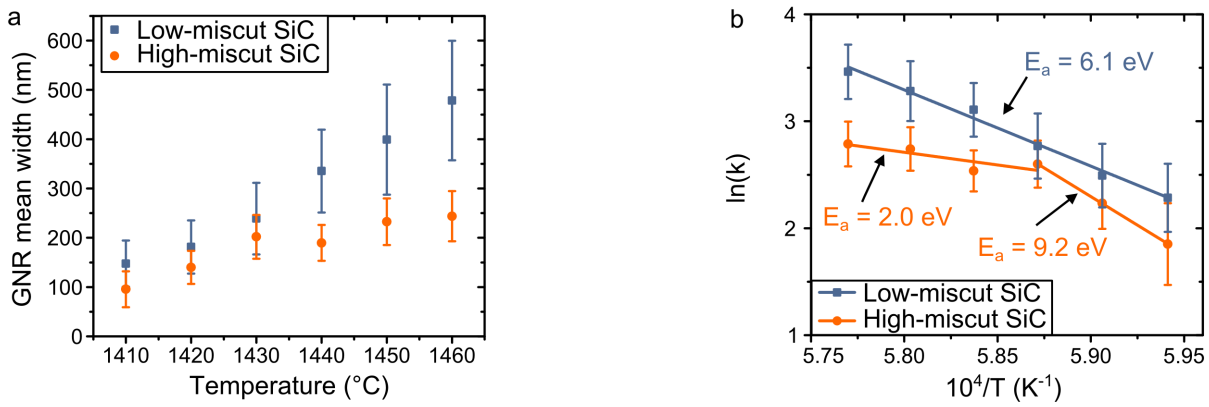

Figure 3.3: (a) The mean width of the GNRs as a function of the synthesis temperature for each type of substrate. (b) An Arrhenius plot of the rate of expansion of monolayer GNRs versus temperature. The activation energies obtained (E_a) are given.

3.4.2 TEM and AFM

TEM and AFM analysis of the step edge regions have provided additional information that illustrate the origin of the variations in the E_a values. It is anticipated that the main difference between the two cases studied here is the unintentional formation of few-layer graphene at the high step facets (7.5 – 18 nm) that are present on the surface of the high-miscut SiC samples. Figure 3.4 shows cross sectional TEM image of GNRs grown at 1 450 °C for 15 min in a low- (a,c) and a high-miscut (b,d) substrate. The influence of the step height is clear; while the same number of layers is seen at the edge and upper terrace of the small step facet, the same region of the high step reveals the existence of few-layer graphene. These results are in agreement with other TEM results from other groups [156, 218]. The AFM data corroborate these findings.

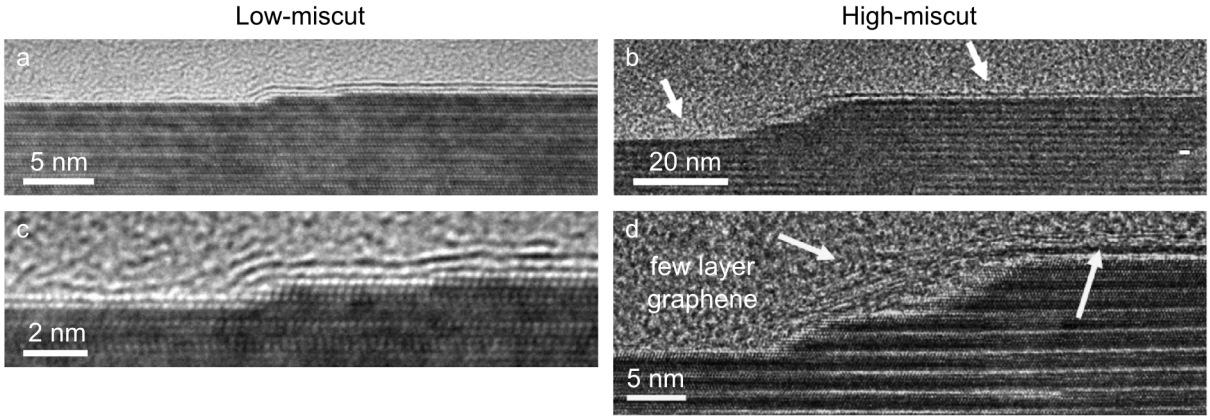

Figure 3.4: Cross sectional phase contrast TEM images of GNRs grown from a low-height step edge (a) and from a high step edge (b). (c,d) Close up views of the step edge area for the images shown in (a) and (b), respectively.

As previously explained in Section 2.4, the phase contrast can provide information about regions of the SiC surface covered by different number of graphene layers, as well as height variations from the step edges. This is illustrated in Figure 3.5, in which the phase contrast of a step edge with a GNR grown at 1 470 °C for 15 min followed by air annealing (a) is compared to one without (b), where only contrast due to the height difference is seen. The profile in Figure 3.5 c contrast the two cases and indicates the phase shift that is induced by the step edge alone due to the height variation.

Figures 3.6 a-b show AFM phase contrast images of single GNRs prepared on low- and high-miscut SiC substrates, respectively. The corresponding height profiles are plotted in (d) and (e). While the small step ($\sim$ 1.1 nm high) of the low-miscut surface only contributes with a sharp, bright line in the phase contrast image due to the height variation (Figure 3.6 a), a broader ($\sim$ 100 nm) and somewhat rough step edge is clearly seen for the high-miscut case (Figure 3.6 b). The observed roughness can be associated with the existence of mini-steps, which are a product of the formation process of few-layer graphene at this region [156, 239]. In addition, both surfaces show an additional small step ($\sim$ 0.4 nm high) at the upper edge of the step where it transitions to the terrace. It delimits the monolayer GNR from the rest of the terrace which is still covered only by a single BL. Considering the interlayer distances between SiC, BL, and MLG, as well as the fact that the formation of a BL will consume half c_{6H-SiC}, a step height of about 0.4 nm is indeed what is expected for the formation of MLG (see discussion below and Figure 3.7). Finally, only for the sake of comparison, results obtained for a GNR prepared on an off-axis SiC(0001) sample possessing an even higher degree of miscut of 4° are shown (Figure 3.6 c). One can clearly see that in this case the $\sim$ 50 nm high step is much broader ($\sim$ 200 nm) and rougher than the other cases (Figure 3.2 f).

The latter is a clear indication of few-layer graphene growth at this region. Interestingly, the height of the transition to the "upper" terrace is $\sim$ 1.2 nm in this case. Considering the same arguments utilized to explain the 0.4 nm step, it can be concluded that the GNR formed in this case is actually composed of three graphene layers (on top of the BL). As will be discussed later, this effect is also directly related to the "parasitic" formation of few-layer graphene at the step facet.

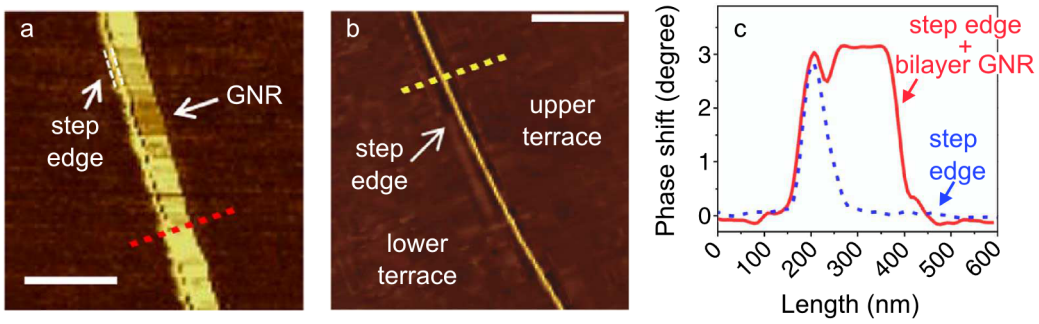

Figure 3.5: (a) Phase contrast image taken from a single bilayer GNR (growth at 1 470 °C for 15 min followed by air annealing). Scale bar, 0.5 μm. (b) Phase contrast image of a step edge without a GNR. Scale bar, 0.5 μm. (c) Phase shift profiles taken from images (a) (red dashed line) and (b) (yellow dashed line).

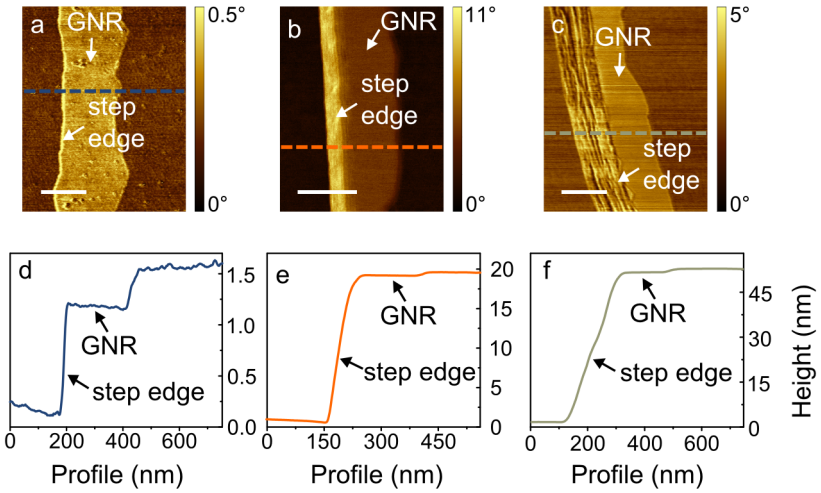

Figure 3.6: AFM phase contrast images for a single monolayer GNR formed on a step edge of a (a) low- and (b) high-miscut SiC sample. The corresponding height profiles are shown in (d) and (e). For comparison, (c) and (f) shows the phase contrast and height profile of a GNR prepared on off-axis SiC(0001) with a miscut of 4°. All GNRs were prepared at 1 430 °C for 15 min. The scale bars in (a-c) correspond to 200 nm.

The height difference between graphene layers and the substrate is depicted in Figure 3.7. Each bilayer of SiC is represented by a green line and every six bilayers compose one unit cell c_{6H-SiC} of 1.5 nm height (Figure 3.7 a). The formation of each graphene layer occurs at the cost of half a c_{6H-SiC} of the substrate (i.e., three SiC bilayers) [240, 101]. The height difference between a graphene layer on top of a BL and the BL on top of three SiC bilayers is illustrated in Figure 3.7 b.

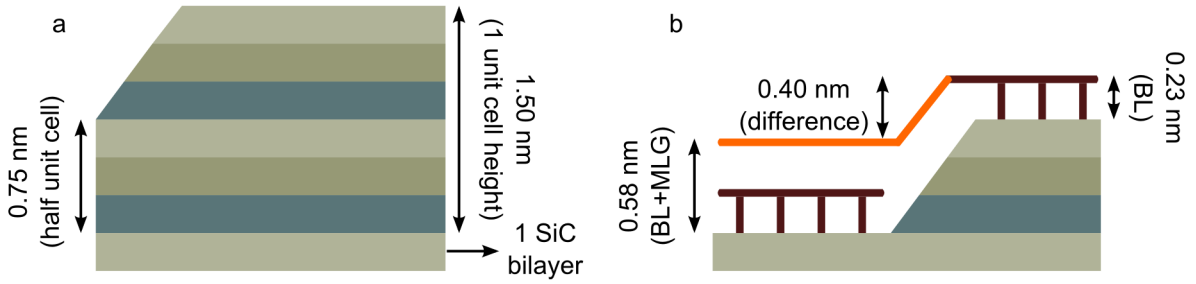

Figure 3.7: (a) Illustration of a 6H-SiC substrate with each bilayer represented by a different green line. One unit cell is formed by six SiC bilayers. (b) Depiction of the height difference between a monolayer GNR on top of a BL and a BL on top of three SiC bilayers.

3.4.3 Raman spectroscopy

Figure 3.8 shows representative Raman spectra obtained from measurements performed at step edges of the SiC(0001) sample having (a) low- and (b) high-miscut. The spectrum of the single BL from a measurement performed on a surface terrace is also plotted for comparison (c). The spectra in (a) and (b) contain the typical G ($\sim$ 1 590 cm^{-1}) and 2D ($\sim$ 2 730 cm^{-1}) peaks expected for the GNRs formed at the step edge region. The G peak overlaps with the BL-related signal, which shows up in the spectra as two broad bands located between 1 200 and 1 650 cm^{-1} [197]. The D peak, also expected to appear in this region, cannot be distinguished due to the BL signal. This BL contribution originates from the BL present beneath the monolayer GNR as well as from the BL covering the terraces. The latter signal is detected in the measurement due to the laser spot of $\sim$ 1 μm that is larger than the GNR lateral width. By comparing the results in Figures 3.8 a-b, it

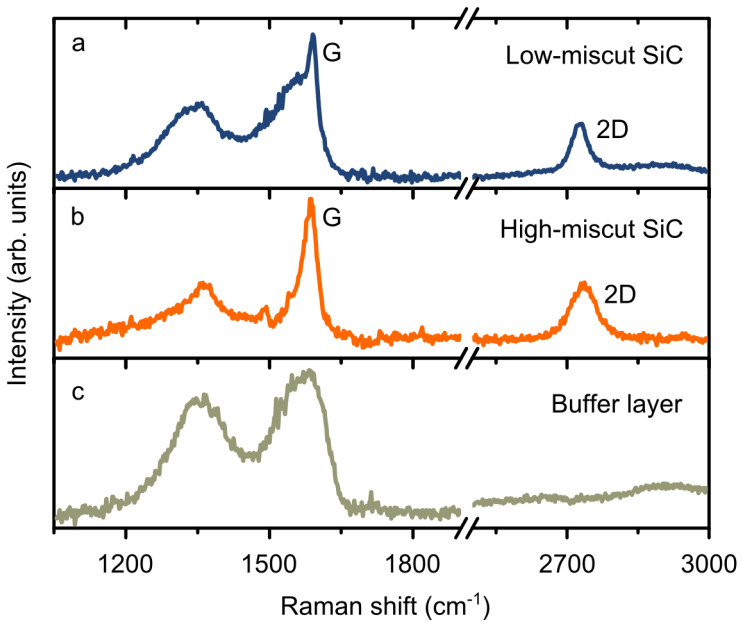

Figure 3.8: Raman spectra of monolayer GNRs (grown for 15 min, at 1 430 °C) at a step edge of the low- (a) and high-miscut (b) SiC substrate. A spectrum taken at a terrace of the high-miscut sample (c) confirms that only a single BL is formed at this region. The background signal originated from the SiC substrate was subtracted from all spectra.

is possible to identify two features in the spectrum of the GNR formed on the high-miscut SiC that confirms the formation of few-layer graphene at the step facet: (i) the stronger intensity of the G peak – which accounts for the quantity of sp^2-bonded atoms captured in the laser spot – in respect to the background BL signal, and (ii) a broader 2D peak (FWHM equals to 68 cm^{-1}) in comparison to what is measured for the low-miscut case (FWHM $\sim$ 38 cm^{-1}, as expected for epitaxial MLG on SiC(0001) [92, 241]). This broadening can be attributed to an overlapping of the Raman signals originating from the monolayer GNR area and from the few-layer graphene formed at the step facet [242, 243].

3.5 Our model for surface graphitization

Based on the obtained results, the mechanisms involved in the GNR growth on both types of substrates are described here (and illustrated in Figure 3.9) according to their explicit dependence on growth temperature, and take into account the formation of few-layer graphene at high steps. Once the SiC(0001) surface is smooth and step bunched (which occurs during hydrogen etching, Figure 3.9 a), the sample is heated to a temperature above Si sublimation (exploiting the fact that C has a lower vapor pressure than Si and will, therefore, desorb only at much higher temperatures). As described in Section 3.3, the steps act as nucleation centers from where Si first desorbs leaving behind a C-rich surface.

For GNRs prepared on the low-miscut substrate, C atoms reorganize to form the BL, which then "advances" from the step edge towards the upper terrace (i.e. the SiC outmost layer retreats as Si atoms leave and the BL is formed), ultimately covering the entire SiC(0001) terraces [218] (Figures 3.9 b-c). Please note that the BL growth behavior was not investigated in detail, and, as a result, it cannot be excluded the fact that the BL may also nucleate and grow directly on the terraces. Simultaneously, Si atoms continue to leave the SiC surface underlying the BL (again from the step edge), which leads to the formation of a new BL below the preexisting one. The latter becomes detached (i.e. it is no longer covalently bound to the SiC surface) and turns into MLG. Thus, as the new BL expands laterally, the MLG region also propagates, increasing the GNR width (Figure 3.9 d). A cross-sectional illustration of a monolayer GNR formed on a low-miscut substrate is shown in Figure 3.9 e. Even for the low-miscut case the carbon layers formed at non-polar facets are illustrated as graphene and not BL. The reason for this is based on previous results from Nicotra et al. [229], who have shown that naturally decoupled graphene layers form at the non-polar step facets without BL.

The activation energies quoted previously were determined on the implicit assumption that the GNR width increases as a function of the temperature. Therefore, they are related to the formation of the new BL taking place underneath the uppermost one. The obtained energies are possibly "apparent activation energies" which contain contributions from the following processes: (i) breaking of Si-C bonds, (ii) lateral diffusion of the Si "adatoms" at the interface between the upper BL and the SiC surface prior to their desorption at the step edge region, (iii) Si out-diffusion (i.e. desorption). Note that direct Si out-diffusion through defects (periodic pentagon-hexagon-pentagons inclusions, for example) existing in the upper BL – which reduces the relative importance of lateral adatom diffusion – have been proposed as an alternative diffusion path [244, 245]. However, the existence of such defects in the BL have been ruled out in other works [240, 246], and, as it will be discussed, our results also do not support this hypothesis. For GNR growth on the low-miscut SiC substrate, the obtained E_a value is close to 6.1 eV. A comparison with previous works in literature, which report energy barriers in the range of 4.5 – 6.1 eV [247, 248] for Si adatom desorption from an exposed SiC(0001) surface, indicates that Si out-diffusion is the process limiting the lateral growth of GNRs on this substrate.

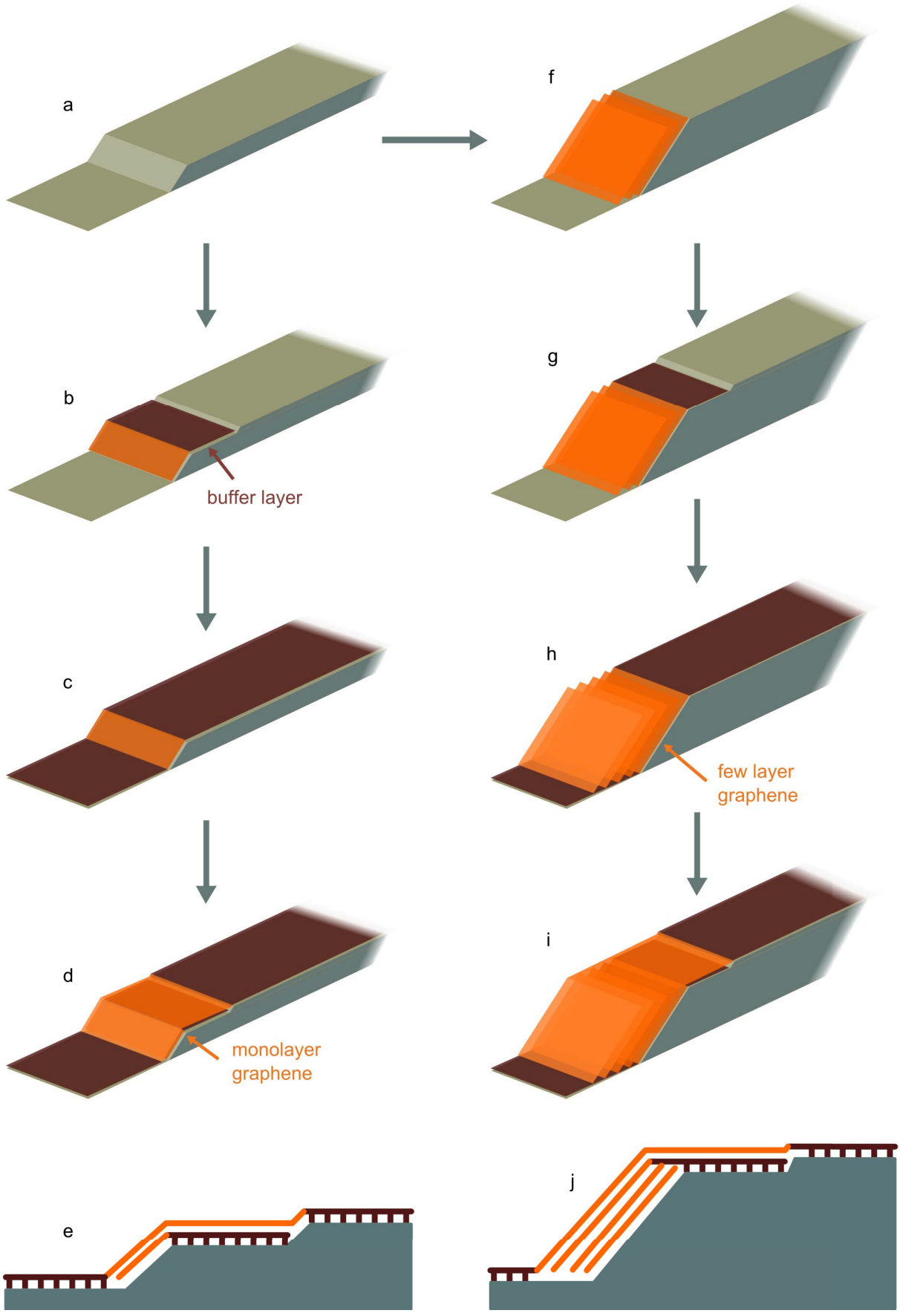

Figure 3.9: Schema for the growth of monolayer GNRs on low (a-e) and high (f-j) steps of a SiC(0001) surface. Note that the figures are not to scale.

The questions that arise at this point are: why is the activation energy for GNR growth on the high-miscut sample higher than in the low-miscut one, and why does the GNR lateral growth rate saturate for temperatures higher than 1 430 °C? In addition to the BL layered growth, the formation of few-layer graphene at the non-polar step facets – prior to and also during the expansion of the BL towards the upper terrace – takes place at high steps (like those observed on our high-miscut substrates) [239]. The higher the step is, the more enhanced will the few-layer growth be due to a higher number of mini-steps acting as nucleation centers. This behavior is portrayed in Figure 3.9. Starting from the bare SiC surface (Figure 3.9 a), the initial BL growth close to the step edge follows the formation of few-layer graphene at the step surface (Figure 3.9 f). The BL will further expand laterally (Figures 3.9 g-h) while new BL growth will also start from the step edge, finally resulting in the formation of a monolayer GNR (Figure 3.9 i). Eventually, as modeled by Ming and Zangwill [239], some of the layers formed at the facet will coalesce, at the upper part of the step, with the BL and graphene layers formed on the terrace. This effect is considered in Figure 3.9 j, which illustrates a cross section of a monolayer GNR synthesized on a step of a high-miscut substrate. Note that in addition to the coalescence, Ming and Zangwill also predicted that some of the layers formed at the facet might "climb over" the terrace, in which case lateral growth will proceed further. This effect, which is expected to be more likely as the dimensions of the non-polar facet increase, is probably the origin of the formation of three-layer thick GNRs on the 4° off-axis SiC(0001), as observed in the AFM results shown for comparison in Figures 3.6 c,f.

The few-layer graphene formation are interpreted as the origin of the higher activation energy found for GNR growth on the high-miscut substrate. The results suggest that, after a certain GNR width is reached, sufficient few-layer graphene has already been formed on the step facets for it to act as an effective diffusion barrier to the subsequently desorbing Si. This increases the apparent energy required for Si adatoms to desorb from the SiC. The practical consequence is that an increase of temperature will not directly lead to an increase in the nanoribbon width unlike during growth on the substrate with low-miscut.

3.6 Summary

In this chapter, the growth rate of monolayer GNRs synthesized via the surface graphitization of stepped SiC(0001) surfaces was studied. The final width of ribbons as a function of annealing temperature and SiC substrate miscut-angle was investigated, and the apparent activation energy for the formation of monolayer GNRs were identified. In this way, it was possible to gain insight into the influence of the substrate step height on the energy barrier for GNR formation. In particular, an additional energy barrier was observed for a substrate exhibiting a high-miscut, which was also correlated with the formation of few-layer graphene on the non-polar step facets. Such growth behavior was not observed on substrates with a low-miscut angle, where formation of few-layer graphene at the low steps does not take place.

Samples of monolayer GNRs were synthesized by the graphitization method on SiC(0001) with temperatures ranging from 1 410 to 1 460 °C in order to elucidate the connection between growth temperature and final ribbon width. Two substrates with different miscut angles, namely 0.1° and 2.0°, were used to determine the influence of initial step height on final GNRs size. The samples were then examined by AFM, SEM, and Raman spectroscopy.

Based on these analyses, an exponential lateral expansion rate was observed for ribbons grown on the low-miscut substrate. In particular, an apparent activation energy of 6.1 ± 0.3 eV was obtained for the expansion rate of individual GNRs on this substrate and correlated with the energy barrier for Si out-diffusion. For ribbons grown on the high-miscut substrate, on the other hand, a nonexponential expansion rate was observed. In the temperature range below 1 430 °C, a higher activation energy of 9.2 ± 0.1 eV was determined, whereas for higher temperatures it seemed to

saturate at 2.0 ± 0.9 eV. The origin of the two growth regimes can be attributed to the formation of few-layer graphene on the step facets. These thicker layers act as an effective diffusion barrier, constricting Si diffusion and therefore explaining the initial increased E_a. It also explains the saturation, because when enough layers are formed, an increase in temperature no longer leads to a corresponding increase in width. This also contradicts the idea of direct diffusion through periodic defects in the BL, since in that case the $E_a$would not depend on the substrate step height and no difference in growth would be observed between the two substrates examined here.

4 Bilayer graphene nanoribbons

4.1 Introduction

Despite being regarded as a promising material for electronic applications [3], one of the main drawbacks of graphene is the lack of a band gap, which inhibits its utilization. In this respect, BLG is of high interest because, unlike MLG, it offers a tunable band gap under a transverse electric field [125, 160, 126]. In addition to BLG, the tailoring of MLG into nanoribbons also induces a band gap, the magnitude of which increases with decreasing the ribbon's width [172, 120, 121, 122, 116]. Therefore, the combination of the properties of BLG with the ones of GNRs is anticipated to be of great utility for the realization of graphene-based nanoelectronics devices with enhanced features, such as improved on/off current ratios [162] and strong electrical noise suppression [163].

The growth of monolayer GNRs on the step edges of SiC(0001) substrates with different miscut angles was studied in the previous chapter. Depending on the growth temperature, either complete graphene layers (1 600 °C) or GNRs (1 410 – 1 460 °C) will be formed. Figure 4.1 shows the growth of MLG (b,g) and monolayer GNRs (d,i) on a low- and a high-miscut substrate (respectively). The formation of few-layer graphene on the higher step edges is also illustrated.

After growth of monolayer GNRs or MLG, a straightforward annealing in air can be used to fabricate of bilayer GNRs or BLG. At first, our group has studied the production of quasi-free-standing BLG on SiC(0001) by oxygen intercalation upon thermal annealing performed in air [223]. The study revealed the decoupling of the epitaxial MLG due to the formation of a thin oxide layer on the SiC surface, and the conversion of the BL into a graphene layer. The resulting BLG, which is p-doped, was also shown to be of high structural quality and uniform throughout the entire sample area. A schematic view of these process is shown in Figures 4.1 b-c for a low-miscut SiC and in Figures 4.1 g-h for a high-miscut substrate. This work has also demonstrated that air annealing a BL-covered sample at the same temperature would result in a complete etching of the BL.

Therefore, when the same air annealing procedure is applied to monolayer GNRs, a similar behavior is observed. This method removes the bare BL from the terraces, while it promotes the decoupling of the BL underneath the monolayer GNRs, leading to the formation of isolated, quasi-free-standing bilayer GNRs. This evolution can be observed in Figures 4.1 d-e and Figures 4.1 i-j for a low- and high-miscut substrate, respectively.

The intriguing selective removal of the BL from the terraces might have its origin on the different atomic corrugation that this layer exhibits when it is bare or covered by a MLG. While the C atoms from sublattice A of a bare BL are on average 0.36 Å closer to the SiC surface than the ones from sublattice B, when the BL is covered by a MLG, this difference amounts to only 0.09 Å [249]. The bare BL therefore exhibits a higher pyramidalization of the sp^2-hybridized C atoms, which increases their chemical reactivity [250]. As a result, in GNRs samples, the bare BL on the terraces strongly reacts with oxygen-containing species during the air annealing. The removal of the BL thus probably occurs due to the formation of volatile species such as carbon monoxide and hydrocarbons. At the step edge regions, where the GNRs grown on top of the BL, oxygen precursors react preferentially with the SiC surface, since the BL underneath has a higher stability.

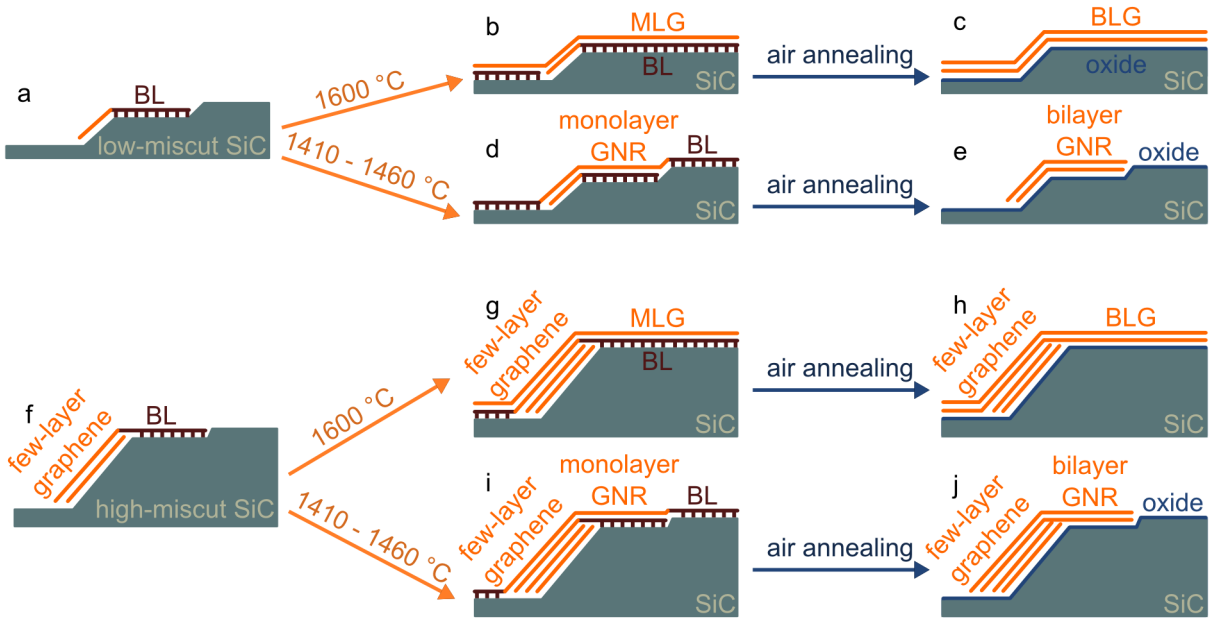

Figure 4.1: Illustration of the growth and air annealing of graphene on a low-miscut (a-e) and a high-miscut (f-j) SiC(0001) surface. Both graphene layers (grown at 1 600 °C, d-e and i-j) and GNRs (1 410 – 1 460 °C, b-c and g-h) are depicted. Note that the figures are not to scale.

A similar effect has been recently demonstrated by Wang et al. [251] for a mixture of oxygen and argon: it removes the exposed BL from the terraces, but, unlike other oxygen-based intercalation schemes for epitaxial graphene films and GNRs [252, 253, 254, 223, 255, 256, 241], it does not decouple the BL underneath graphene, so that instead of isolated bilayer GNRs, one can obtain isolated monolayer GNRs.

Hence, these results serve to illustrate the potential offered by annealing in oxygen-containing atmospheres for performing controlled post-growth intercalation and modifications in epitaxial GNRs. The relative simplicity [223] and compatibility with standard oxidation schemes for semiconductor processing [257] are also important aspects regarding future applications. However, differently for instance from the most widespread method for modification of epitaxial graphene, namely H-intercalation achieved by thermal treatment in a pure hydrogen atmosphere [32, 258, 259], the generation of defects in the graphene lattice, which has an impact on the transport properties [224], is anticipated to be a side effect of oxygen-based treatments that might hinder a broader use of this method. In this context, understanding the stages of oxygen intercalation and how different parameters lead to distinctive changes in the morphology related to the formation of defects is highly relevant. This chapter reports a systematical investigation on the influence of the duration of air annealing treatments, substrate miscut angle, as well as GNRs' width, in the process of oxygen intercalation. The samples are characterized by different techniques to fully understand the stages that comprise the process of oxygen intercalation upon air annealing.

4.2 Sample preparation

Epitaxial monolayer GNRs were fabricated on SiC(0001) substrates by the surface graphitization method (previously described in Section 3.2 on page 43). To study the effects of post-grown air annealing in various conditions, three different substrates were employed, namely A, semi-insulating and with a low-miscut of 0.1°; B, doped and with a slightly higher miscut of 0.2°; and

C, doped and with a high-miscut of 3.6°. All samples were grown in a RF-induction furnace and subsequently annealed in air in another furnace at 600 °C for various times (see Section 2.1.4), as mentioned below. A series of monolayer GNR samples was fabricated with the same growth time and temperature (15 min at 1430 °C) on substrate A, and subsequently annealed in air for different times, ranging from 15 to 240 min, to study the effect of the duration of air treatment in the ribbons' morphology. Two monolayer GNR samples were synthesized on substrate B for 15 min at different growth temperatures (1410 °C and 1450 °C), followed by the air annealing treatment (for 50 min), in order to study the effect of the oxygen intercalation in ribbons possessing different widths. Finally, nanoribbons with similar dimensions were grown for 15 min at a lower temperature (1390 °C) on substrate C, and afterwards thermally treated in air (for 50 min) to analyze the correlation between oxygen intercalation and the substrate miscut. The structural characterization of the samples was performed by means of AFM, SEM, TEM, XPS, and Raman spectroscopy.

Substrate	Miscut angle	Conductivity	Growth temperature	Air anneal duration
A	0.1°	semi-insulating	1430 °C	15 – 240 min
B	0.2°	*n*-doped	1410 °C and 1450 °C	50 min
C	3.6°	*n*-doped	1390 °C	50 min

4.3 Series of GNR samples annealed in air for different periods of time (0 – 240 min)

The influence of air annealing time on the morphology of the bilayer GNRs was studied by preparing a series of identical monolayer GNRs samples on substrate A, which were then intercalated in air for different durations. Height and phase contrast AFM images of the pristine (0 min) and annealed samples (15 – 120 min) are presented in Figure 4.2. For this growth temperature (1430 °C), it is expected that, before thermal treatment in air, the monolayer GNRs appear close to the step edges and the BL covers the terraces (see previous chapter). This is verified by the dark and bright contrast observed in the phase contrast images, which are due to the GNRs and the BL, respectively. After air annealing, the GNRs exhibiting a dark contrast are still observed close to the step edges, indicating that they endure the thermal treatment up to 45 min. It is expected that after 40 min the air annealing process removes the BL from the terraces [241]. It is not clear from the AFM images whether this process can occur prior to this period, but this should be the case for the samples thermally treated for longer than 40 min. From the phase contrast images, there is no significant change in the GNRs until 45 min of air annealing, however after 1 hour the ribbons are almost entirely gone and only some areas where graphene is still present can be observed. The stripes observed in the middle of the step edge indicate those areas (shown in the inset). After 2 hours of treatment, the dark contrast has completely vanished, indicating that all graphene is removed from the sample. Even in this sample it is still possible to observe some phase contrast, which correspond to the height difference between the terraces and the areas previously occupied by the GNRs.

Even though AFM indicates morphological changes in the GNRs, it does not reveal at which point the conversion of monolayer into bilayer GNR occurs, or when the removal of the BL from the terraces takes place. A technique which is better suited to distinguish between BL, MLG and BLG is Raman spectroscopy. Raman spectra of four samples measured in the areas correspondent to the GNRs are presented in Figure 4.3 a. Before the intercalation treatment, the BL-related signal (two broad bands located between 1200 and 1650 cm^{-1} [197]), as well as the typical G ($\sim$ 1590 cm^{-1}) and 2D ($\sim$ 2730 cm^{-1}) peaks for MLG can be detected, confirming that both GNRs, which are observed close to the step edges, and the BL (on the terraces) are present. The BL-related signal is no longer observed after the air annealing treatment, suggesting that the BL has

been removed from the terraces even after 15 min of air annealing. Instead, a small D peak is noticed around 1365 cm^{-1}. Additionally, a broadening of the 2D peak from 39.5 to 56.5 cm^{-1} is noticed after 15 min of air annealing (Figure 4.3 b) and, instead of only one, four Lorentzians are necessary for the 2D peak fit, indicating that the monolayer GNRs turned into bilayer ones [33]. After 30 min of treatment, the Raman spectrum is very similar to the 15 min sample, however after one hour the graphene signal completely vanishes, indicating a removal of the GNRs and in agreement with the AFM findings. Please note that, because the signal that arises from SiC substrate around 1500 – 2000 cm^{-1} is considerably higher than that of the surroundings, the removal of the SiC background from each spectrum leads to a higher noise in this region. This is due to the larger difference between the subtracted background signal and the originally measured spectra around this area.

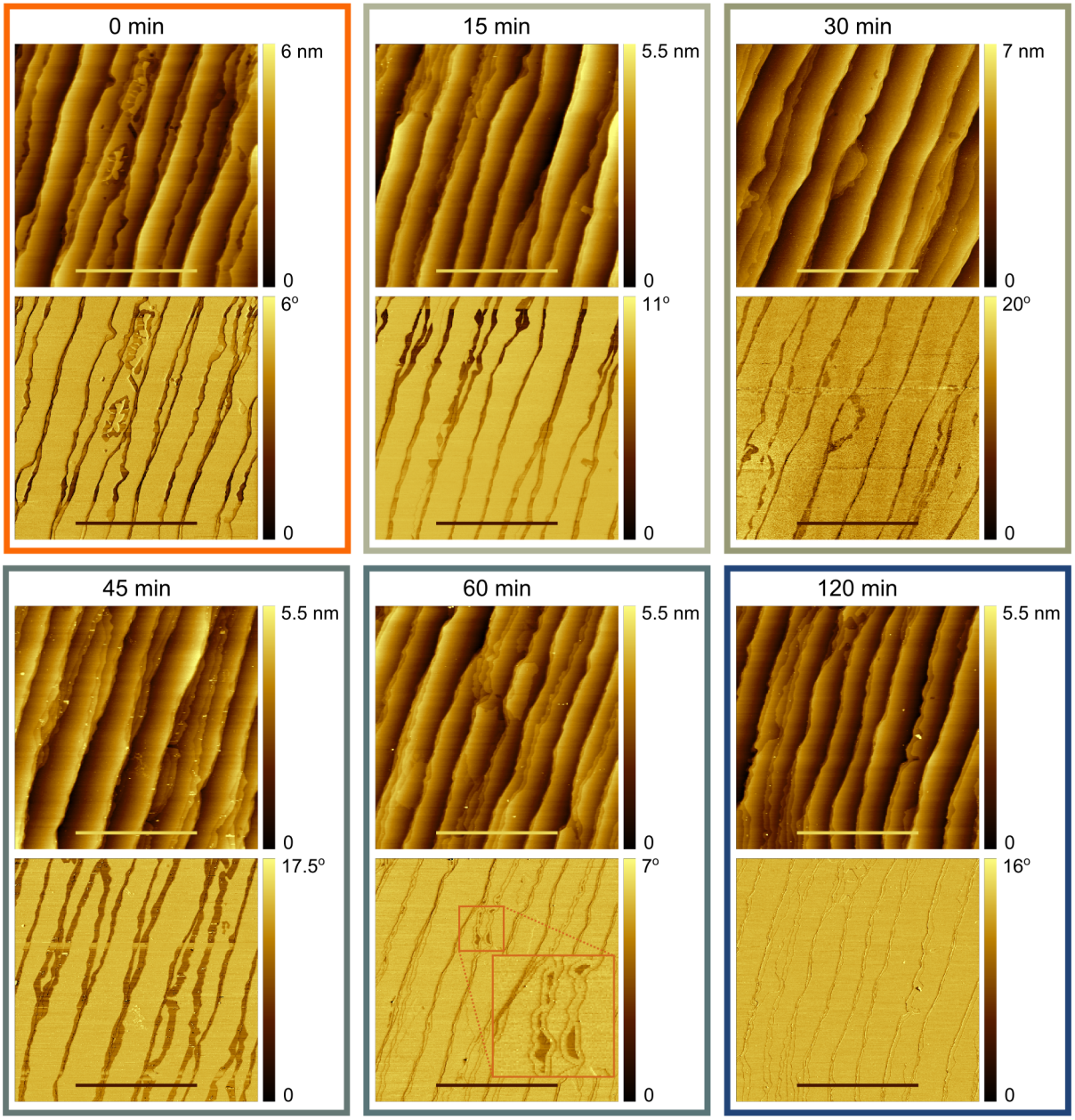

Figure 4.2: AFM height (upper) and phase contrast (lower) images from GNRs before (0 min) and after different periods of air annealing (15 – 120 min). Scale bar corresponds to 5 μm.

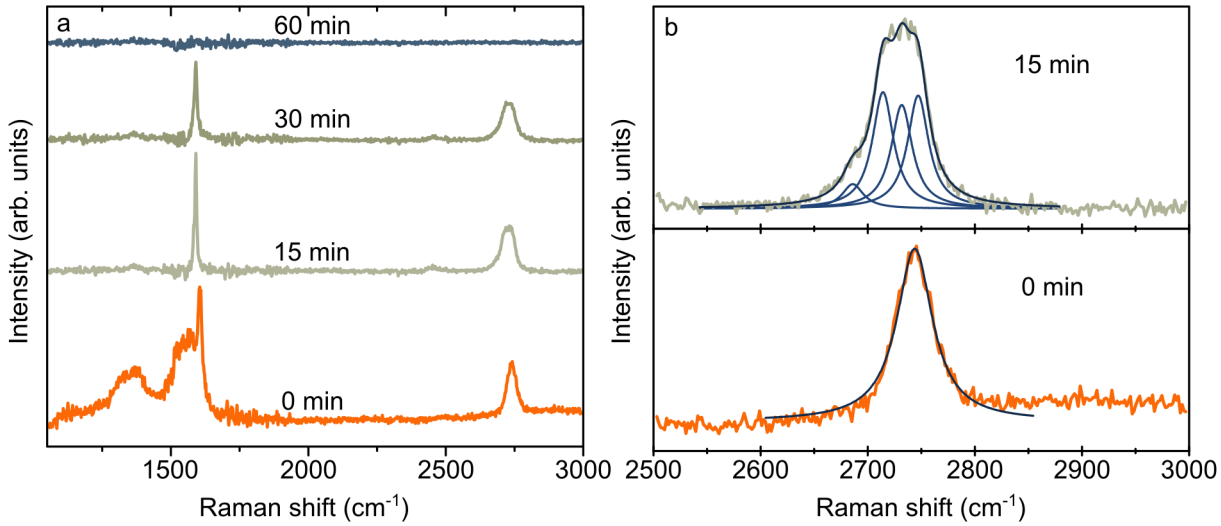

Figure 4.3: (a) Raman spectra of GNRs samples before (0 min) and after (15 – 60 min) air annealing. (b) Raman spectra of the 2D peak of GNRs samples before and after 15 min of air annealing with fitting.

To understand how oxygen interacts with the graphene/SiC system, core-level spectra of the C 1s and Si 2p from a reference SiC substrate (out of the box) and the GNR samples were collected before and after air annealing processes for different durations (Figure 4.4). Possible charging effects were eliminated by applying a silver paste around the samples and by verifying that the position of the spectra did not change with the exposure of a flood gun (a device that provides a steady flow of low-energy electrons to the sample area).

The SiC bulk component of the C 1s spectrum of a p-type 6H-SiC(0001) substrate is located at $\sim$ 281.9 eV [260], whereas for a n-doped SiC substrate the same peak is placed at 283.4 eV [261]. The SiC substrate used in this study, whose SiC bulk component is centered around 282.8 eV (Figure 4.4 a), is semi-insulating. A shoulder at higher binding energies centered around 284.8 eV is attributed to a surface contamination [262], possibly a natural oxide layer from the sample out of the box. Once GNRs are fabricated on top of the substrate, the SiC bulk component exhibits a shift of $\sim$ 0.7 eV to higher binding energies. In addition, new components centered around 284.8 eV with a shoulder at higher binding energies are related to the formation of graphene and the BL, respectively [223]. After 15 minutes of the air annealing treatment, distinct components associated with the formation of C-O-related species at the surface are observed at higher binding energies in the C 1s region [**?**]. As the duration of the air annealing process increases, the intensity of the contributions related to graphene and the BL decreases in comparison to the SiC bulk component, evidencing the etching of the BL from the terraces and the GNRs (in agreement with Raman and AFM data). Finally, after 120 minutes the spectrum of the GNR sample resembles the one from the SiC standard sample, before any graphene growth, indicating that a similar surface, composed of the SiC bulk component and residual C-O components, is observed. Seemingly, the difference between the two spectra is due to the difference between the native oxide layer observed in the SiC standard sample (out of the box) and the oxide originated from the intercalation process, which lead to a shift.

The Si 2p core level spectra of the standard SiC surface (Figure 4.4 b) features the components corresponding to the SiC bulk [223], as well as a shoulder to higher binding energies, which is assigned to a natural oxide layer [260]. After GNR growth, a shift to higher energies of $\sim$ 0.6 eV is observed when compared to the SiC standard, similar to the one noticed in the C 1s region. Such peak shifts indicate a band bending [32, 252, 223], which could be caused by a charge transfer

between the newly formed BL and the SiC substrate to adjust their Fermi energies at the same height. The band bending made the components of the SiC substrate shift to higher binding energy. After air annealing, new Si-O-related species, represented by a shoulder at higher binding energies, are formed.

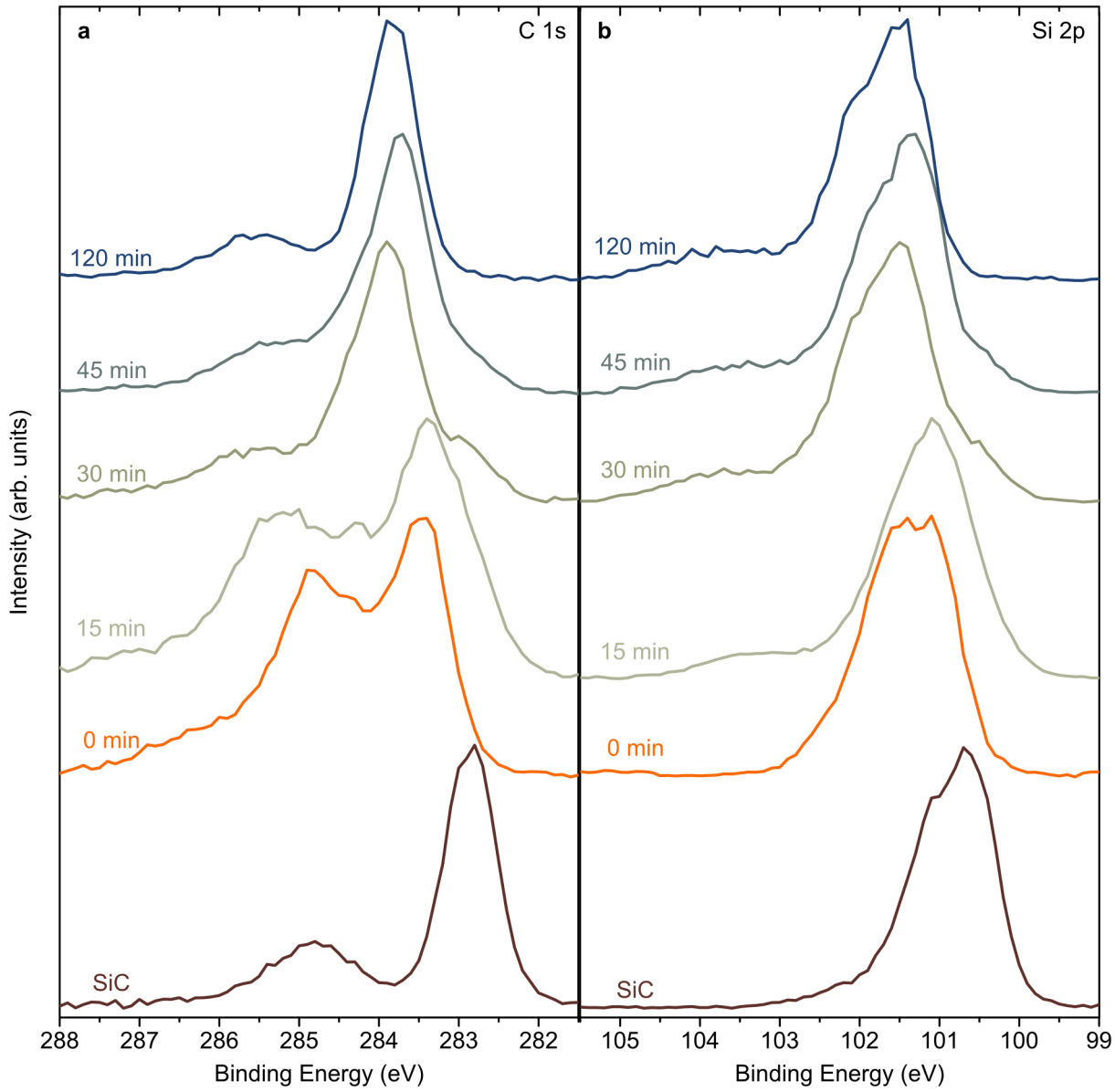

Figure 4.4: Normalized XPS (a) C 1s and (b) Si 2p core level spectra of SiC standard, and GNRs before and after air annealing treatment at different times.

To observe the evolution of the decoupling of the BL in the monolayer GNR areas (leading to bilayer GNR), the AFM height profile at the steps edges containing ribbons was studied next (Figure 4.5). Due to the formation of an oxide layer during the air annealing treatment [223], it is difficult to assess what is the real height difference between the ribbons and the terraces. Nonetheless, a qualitative analysis has proven useful. Before air annealing, the GNRs have a lower height when compared to the terraces, because three bilayers of SiC (0.75 nm) are consumed to

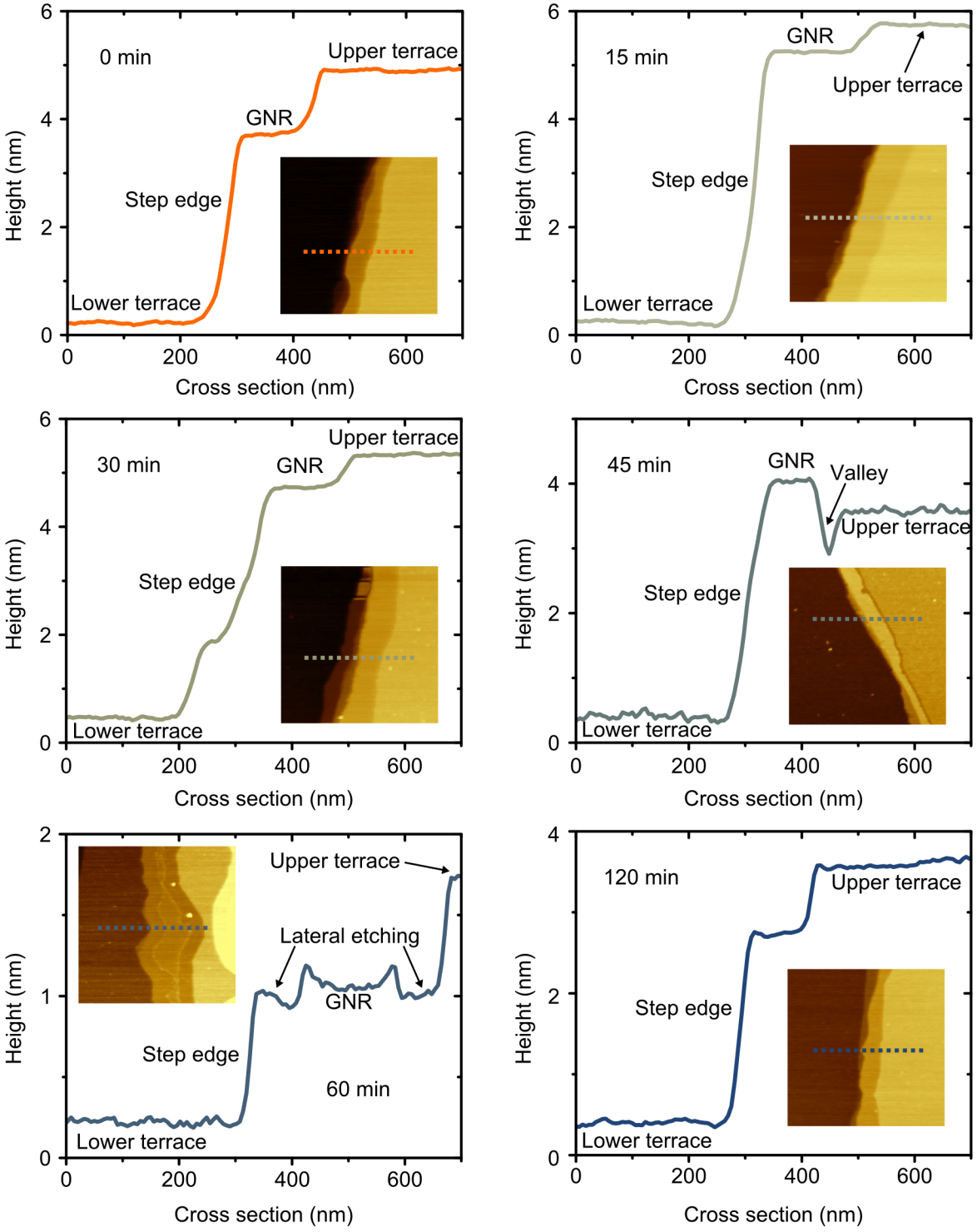

Figure 4.5: Cross section and corresponding AFM image (insets) for GNRs before (0 min) and after different periods (15 – 60 min) of air annealing.

form each graphene layer ($\sim$ 0.35 nm). Up to 30 min of air annealing there is no pronounced difference between the cross sections of the ribbons. After 45 min, a small valley between the ribbon and the terrace appears, a first indication that a lateral etching of graphene takes place. After one hour of treatment, the lateral etching of the remaining ribbons increases and takes place on both

edges, and the cross section reveals the removal of graphene at the border with the terrace as well as at the edge of the step. This means that the width of the GNRs also decreases as the time of air anneal increases. Finally, after two hours of thermal annealing, as judged from AFM analysis, there is no graphene left on the step edge region and the cross section displays the consumed SiC region that was originally covered with the GNR.

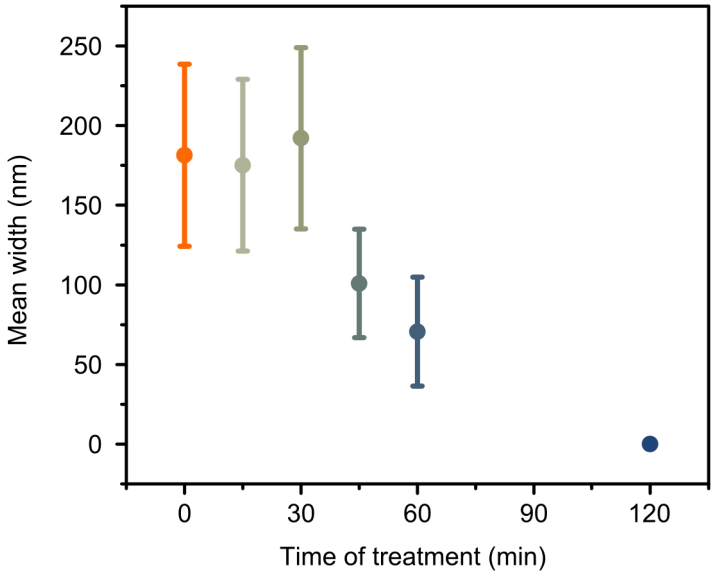

Figure 4.6: Mean width and standard deviation of GNRs as a function of air anneal time.

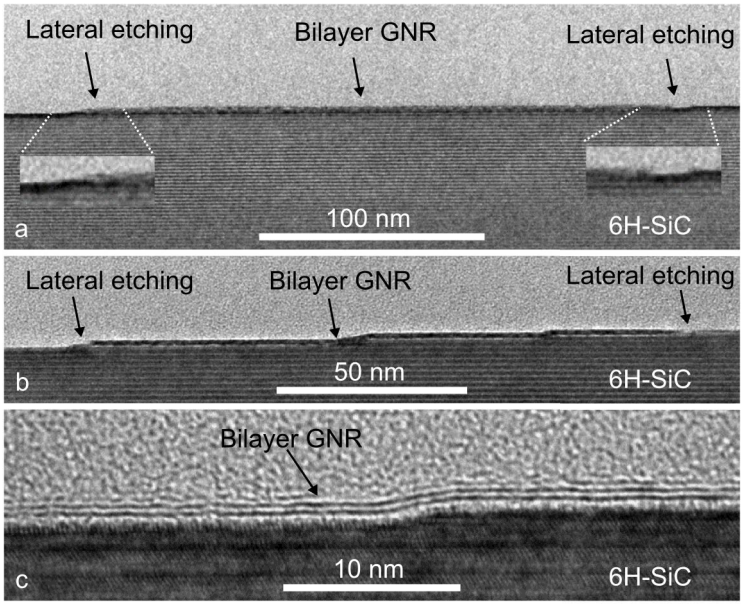

Figure 4.7: TEM images of the bilayer GNRs on SiC after air annealing, showing the process of lateral etching at the borders of the ribbon.

To better quantify the lateral etching of the GNRs (i.e., the decrease in their width), a statistical measurement of their lateral width was performed (Figure 4.6). As already seen on Figure 4.5, up to 30 min of air annealing there is no noticeable lateral etching, and, accordingly, the mean width of the ribbons remains nearly the same. After 45 min, a significant reduction of the width is seen,

which then further decreases for the sample treated in air for one hour. After two hours, the mean width is zero, i.e., graphene has been fully removed from the sample.

Figure 4.7 a shows a TEM image of a GNR on SiC from the substrate B (fabricated at 1440 °C) after air annealing for 50 min. There is no graphene covering the substrate both at the SiC step edge and at the border with the terrace any longer (where SiC has been consumed to form the BL), an evidence of lateral etching. Figure 4.7 b shows a different GNR from the same sample, in which lateral etching also occurs at the borders of the ribbon, exposing the step edges. Additionally, in comparison to the previous ribbon, this one crosses a few steps edges, an effect that can also be observed in the higher magnification image from Figure 4.7 c. This image also shows two graphene layers covering the SiC surface, confirming again the decoupling of the BL and conversion into BLG.

4.4 Additional effects observed for different substrates

To gain more insight into the effects of air annealing on the GNRs, other substrates (i.e., with distinct miscuts) were also used, which lead to different widths of the GNRs. Accordingly, monolayer GNRs were fabricated on a high-miscut SiC wafer (substrate C) at 1390 °C. This was followed by an air annealing treatment for 50 min for O_2 intercalation and thus formation of bilayer GNRs. Because of the high-miscut, the terraces are quite narrow for this sample (approx. 200 nm), resulting in areas which are mostly covered with graphene (dark contrast of the phase image inset in Figure 4.8 a) before air annealing. The GNRs on the terraces undergo a severe lateral etching upon air annealing (Figure 4.8 a), disconnecting them from the few-layer graphene at the step edges, leading to isolated bilayer GNRs. This enhanced etching is probably a result of the different step facet in this sample, which reacts differently with oxygen during the intercalation.

Besides the lateral etching effect, additional features were investigated in this sample. Figure 4.8 c-d shows the height profile of an elevation of 0.24 nm, a phenomenon which has been observed previously [**?**]. This can be understood as a slight localized expansion of the oxide layer underneath the suspended bilayer graphene, which pressures the later and results in the elevated height profile. Additionally, depressions were observed in Figure 4.8 e-f, whose cross section shows a depth of 0.68 nm, which corresponds to the height of the graphene layers surrounding it. This means that such holes reach the oxidized substrate, and are therefore expected to originate from the expanded oxide spots, in a process which started from bellow and evolved to burst the graphene layers to such holes. By considering the green dashed line on the phase image in Figure 4.8 a, it seems clear that the same phase contrast, i.e. both inside the hole and on the terraces, is an additional indication that both areas have the same material (namely silicon oxide). A previous study has reported similar effects for the etching of the BL by oxygen annealing [251]. Wang et al. observe the lateral etching starting from the step edges as well as etched spots on the BL, suggesting that it occurs at defective sites of the BL. However, in their study the BL underneath the monolayer GNRs was not decoupled and was therefore preserved.

GNRs were also grown in a low-miscut, doped SiC substrate (B) at different growth temperatures (namely 1410 °C and 1450 °C), and then submitted to air annealing at 600 °C for 50 min (Figure 4.9). Unlike the high-miscut substrate, the large terraces from this substrate result in (mostly) isolated GNRs. The 40 °C difference resulted in wider ribbons for the sample fabricated at higher temperature (as previously reported in Chapter 3), which allowed the observation of the influence of different widths on the thermal treatment. By comparing the samples grown at different temperatures, it seems clear that both the lateral etching and the oxidation holes are more pronounced for wider ribbons. Once again, the fact that the same phase contrast is seen inside the holes and on the terraces indicates that the same material (i.e., silicon oxide) is present on both.

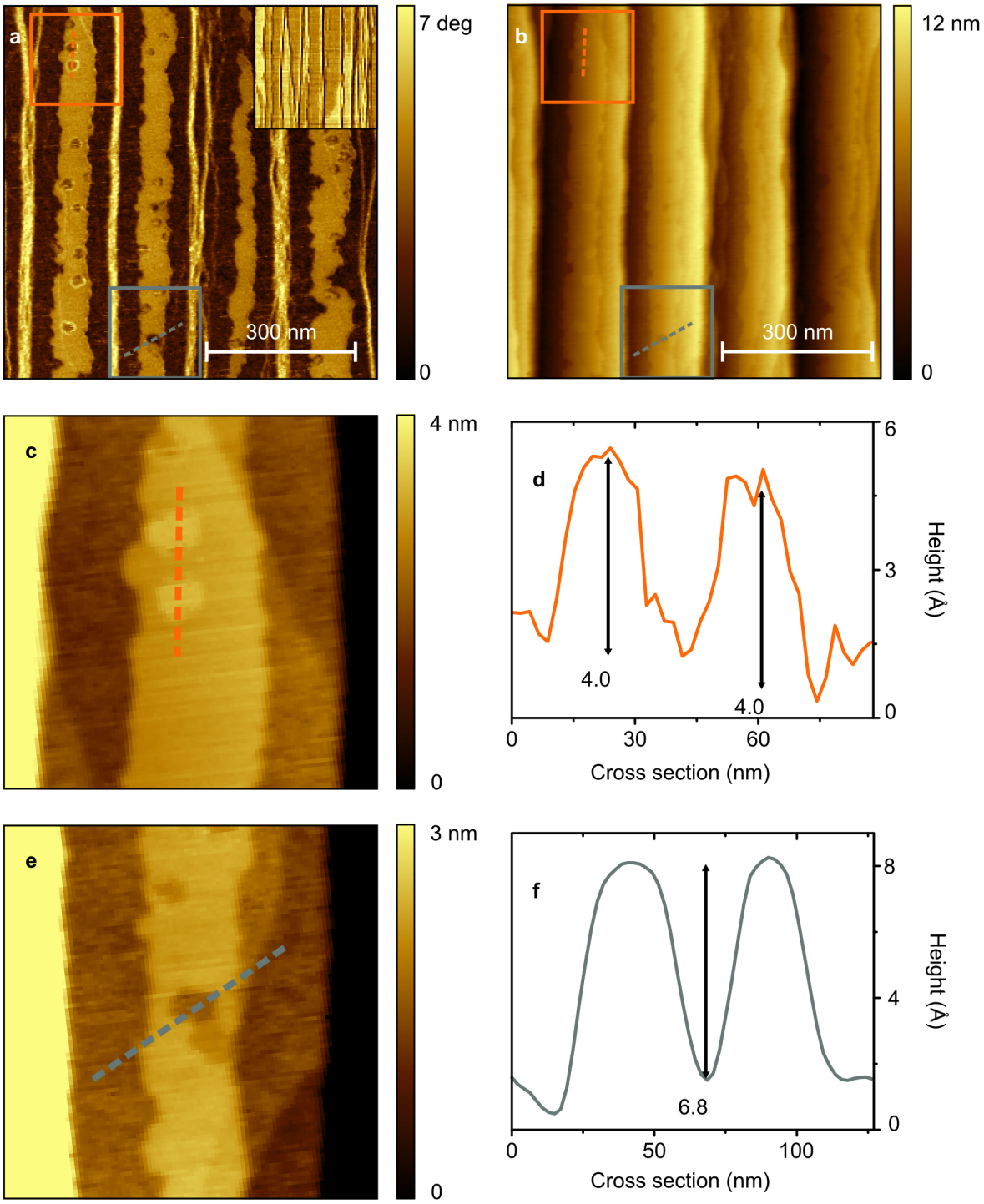

Figure 4.8: AFM (a) phase and (b) height contrast of a high-miscut GNR sample after air annealing. Inset in (a) shows the phase contrast before air annealing. (c) and (e) are leveled height AFM from (b). (d) and (e) are cross sections from the dashed lines in (c) and (e), respectively. The same dashed lines also appear in the phase contrast in (a).

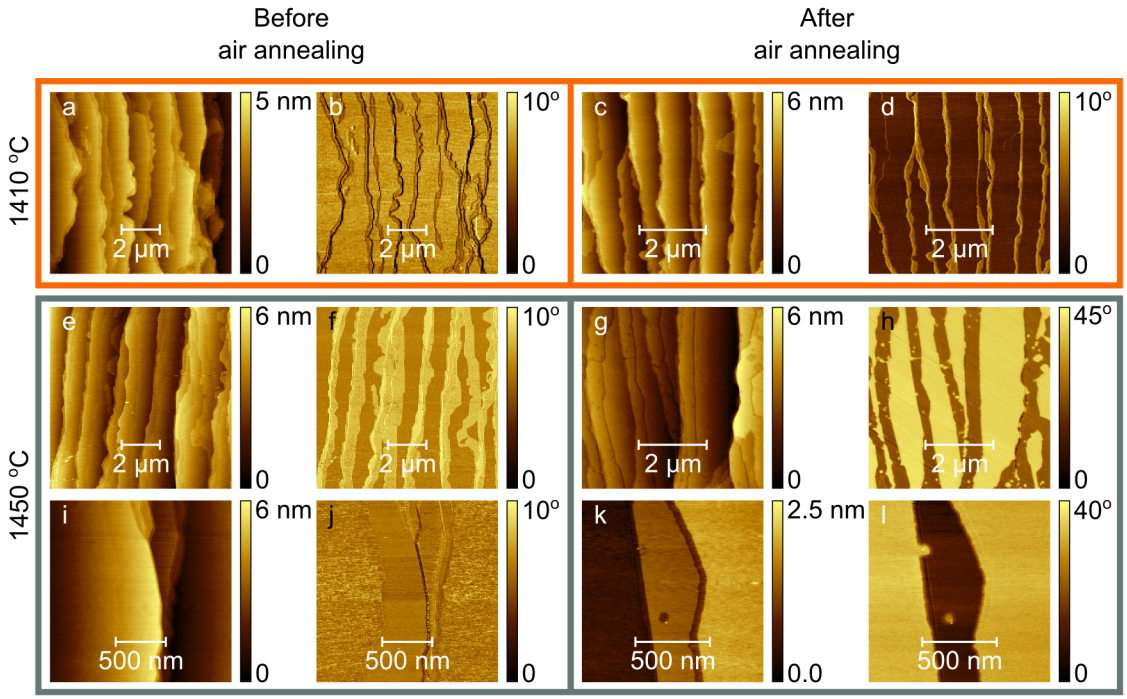

Figure 4.9: Phase and height images from samples grown at 1410 °C before (a-b) and after (c-d) air annealing. Similarly, phase and height images for samples grown at 1450 °C before (e-f) and after (g-h) intercalation, with a higher magnification in (i-j) and (k-l), respectively.

Another set of samples was grown on substrate B and annealed in air for 2h, 3h and 4h. Figure 4.10 shows SEM images before and after air annealing. The as grown sample (a) still contains BL on the terraces, whereas after air annealing (b-c) Raman measurements show that the BL is removed. Therefore for Figures 4.10 b-c the bright contrast is attributed to the SiC surface. After 2h of treatment (b), a lateral etching effect can be observed, though it does not remove graphene completely. Unlike what was observed for the ribbons grown on substrate A at a lower temperature, the GNRs have not yet been removed. The appearance of holes in the ribbons, similar to what has been shown for substrate C (see Figure 4.8), is also noticeable. After 3h (c), the effects are even more pronounced and, after 4h no more graphene is observed in this sample (not shown). The inset in (c) shows AFM height contrast from one of the holes of the sample that was thermally treated for 3h. In Figure 4.10 d, the cross section corresponding to this inset shows that the depth of the hole is once again equal to the height of the bilayer graphene.

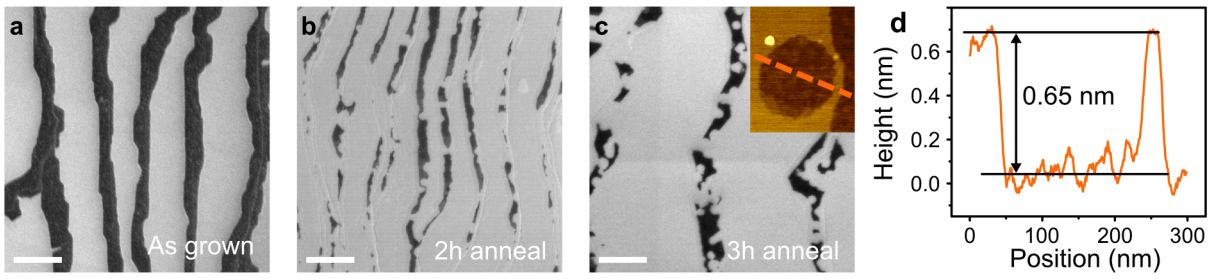

Figure 4.10: SEM image of GNRs (darker contrast) before (a) and after 2h (b) and 3h (c) air annealing. The inset in (c) shows an AFM image of a hole, whose dashed line corresponds to the cross section in (d). The scale bar corresponds to 1 μm.

4.5 Transport characterization

Bilayer GNRs prepared in a similar fashion as the ones described above for a n-type SiC substrate with a nominal 2° miscut angle were probed by electronic transport by the group of Prof. Christoph Tegenkamp from the Leibniz Universität Hannover. The results were published in an article entitled "Quasi-free-standing bilayer graphene nanoribbons probed by electronic transport" [224] and will be shortly summarized in this section.

Epitaxial graphene ribbons with typical widths in the order of $w \approx$100 nm were obtained by growing at 1420 °C for 15 min, and subsequently annealing in air for 50min at 600 °C. Two bilayer GNR structures were mapped by STM (Figure 4.11 a) and exhibit roughness on the edges. The electronic properties of such ribbons, as well as the substrate, were probed by I(V) curves measured by scanning tunneling spectroscopy (STS). I(V) curves taken on top and next to the GNRs show fundamentally different behaviors (Figure 4.11 b), which can be further quantified by the local density of states (LDOS), which is the normalized dI/dV signal (Figure 4.11 c). While the spectrum taken on the GNR exhibits the characteristic parabolic shape expected for a BLG [263, 264], a large bandgap of $\sim$ 3 eV reflects the 6H-SiC substrate in between the ribbons [265]. Since at zero bias the LDOS of the ribbons is finite, they are expected to be metallic [266, 267]. Previous ARPES measurements showed that oxygen intercalation causes p-type doping with a hole concentration of $p_S = 1.3 \times 10^{13}$ cm^2 [223], which corresponds to a Fermi energy of $E_F \approx 550$ meV below the Dirac point. The minimum seen at $V \approx 550$ mV, which is attributed to the position of the Dirac point E_D and small gap in AB-stacked BLG, indicates p-type doping (in full agreement with ARPES measurements [223]).

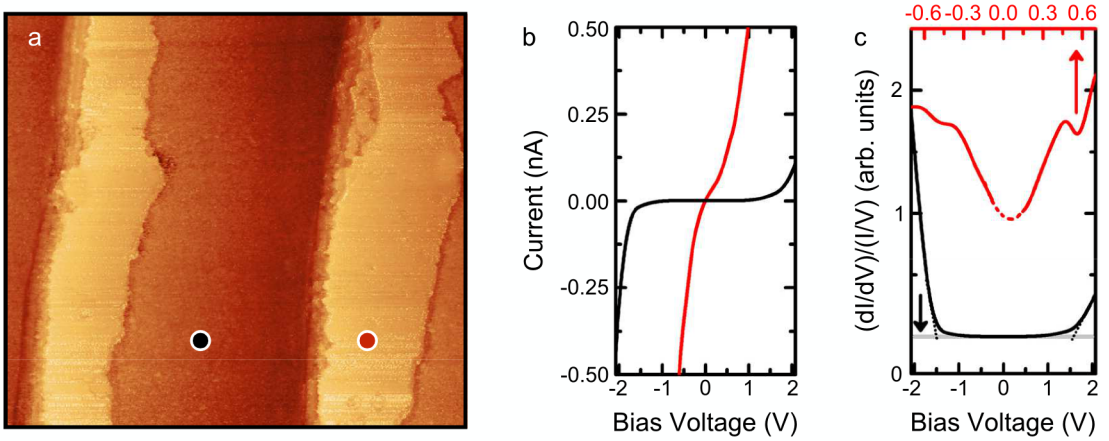

Figure 4.11: (a) Large scale STM image (600 × 600 nm^2, $V_B = +2$ V, $I_T = 500$ pA) of two bilayer GNRs. (b) I(V) curves taken on the GNR (red line, setpoint +1 V, 0.5 nA) and in between (black line, setpoint −2 V, 0.3 nA). The positions are marked in (a). (c) Normalized $(dI/dV) \,/\, (I/V)$ spectra showing the density of states, with different energy scales for each spectra.

2PP measurements taken on the ribbons indicate a linear behavior (in red), whereas a Schottky-diode like behavior is observed if one of the tips is placed besides the ribbon (in black), on the substrate (Figure 4.12 a). The absolute current value also increases in about three orders of magnitude for the GNR in comparison to the substrate, indicating that the ribbons are indeed electronically well decoupled from the substrate. Figure 4.12 b shows the resistance as a function of probe spacing (which is large, compared to the width w), for different GNRs and probe geome-

tries, measured at 300 K. The squares denote 2-point probing, whereas the stars designate co-linear 4PP geometry, in which the current between the outer probes varies from $-10\ \mu$A to $10\ \mu$A, while the voltage difference between the inner probes is measured. The good agreement of the 4-point geometry when compared to the 2-point one indicates the good agreement between the techniques, and demonstrate the low contact resistance of the tips. The resistance curves (squares) increase linearly with the probe spacing, a behavior expected for 1D diffusive transport [268]. Since the linear fits intercept the origin, the contact resistances of the tips are negligible. The resistance per length R/l corresponding to the two ribbons measured in this geometry are around 12 $\mathrm{k\Omega}/\mu$m ($w \approx 70$ nm) and 8 $\mathrm{k\Omega}/\mu$m ($w \approx 100$ nm), which yields comparable sheet resistances of $R_S = (R/l) \times w \approx 800\,\Omega/\square$. Considering the hole concentration obtained by STS and confirmed by ARPES, a hole mobility of around $\mu = 700\,\mathrm{cm}^2/(\mathrm{V\,s})$ was obtained. The values are comparable to other intercalated graphene systems (e.g., microwave-induced oxygen plasma intercalated graphene [**?**]) and are only marginally lower compared to epitaxial graphene without intercalates [**?**]. Since ARPES shows two bands crossing E_F, the bilayer GNRs are close to a regime of multiband transport [269], for which a mean free path length of $\lambda_e \approx 3$ nm is estimated [270]. This indicates why the atomic roughness of the edges is irrelevant for the transport along the ribbons.

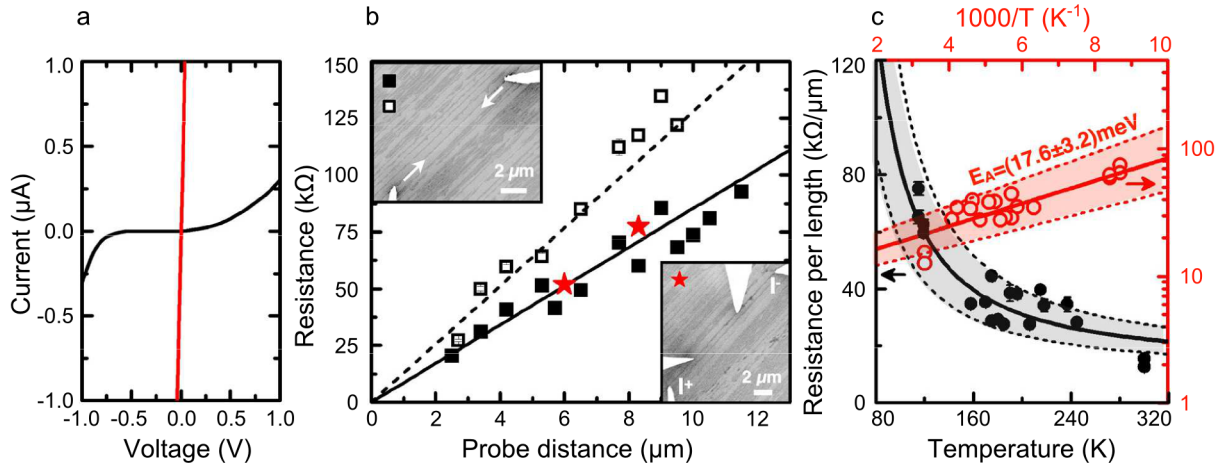

Figure 4.12: (a) Characteristic 2PP I(V) curves taken on the GNR (red) and with one of the two tips on the SiC substrate (black). (b) Resistance as a function of probe spacing for various GNRs measured at 300 K both with the 2PP and co-linear 4PP geometries. Upper inset: SEM image showing a 2-terminal setup. The arrows show the direction of probe movement. Lower inset: SEM image showing a co-linear 4PP arrangement to estimate contact resistances. (c) The resistance per length R/l of various BL-GNRs with comparable widths, as a function of temperature (in black). The same data points are also plotted on the logarithmic scale against the inverse temperature (in red). The solid curves show the best-fits to the points, while the shaded bands denote one standard deviation.

Temperature dependent measurements of the resistance per length are summarized in Figure 4.12 c for ribbons of slightly different widths, which is responsible for the scattering of the data. The resistance per length is reduced by a factor of four as the ribbons are annealed from 100 K to room temperature. In comparison, single layer graphene on SiC typically shows a metallic behavior induced by the weak electron-phonon interaction [271, 57] with an increase of the mobilities by only around 40 % due to remote phonon scattering [270, 272]. Bilayer GNRs, in contrast, show a much stronger effect with opposite trend. Figure 4.12 c also shows a plot of $\log(R) \times 1/T$, i.e., the Arrhenius plot, with a clear temperature activated transport behavior. An activation energy

of around 17 ± 3 meV is deduced from it. This characteristic activation energy already indicates that various defects along the channels, such as holes and lateral roughness promoted by the etching during oxygen intercalation, do not dominate the transport, since several activation energies would be expected otherwise.

The electronic transport in MLG is restricted to the π-orbitals of graphene, which are symmetrically extended with respect to its hexagonal plane. In contrast, propagation in BLG occurs along the π-bands located around each of the two layers, turning interlayer hopping viable [273]. Phonon-assisted interlayer tunneling determines the conductivity across basal planes in graphite [274], and the interlayer hopping of the charge carriers is helpful to circumvent in-plane defects.

In summary, the STS results reveal a strong p-type doping due to charge transfer into the oxide underneath. The process of oxygen intercalation is robust and effectively decouples the GNRs from the substrate. The transport properties are not limited by the edge roughness promoted by etching due to air annealing. Although transport channels in nanostructures can be easily suppressed by defects, phonon-assisted tunneling in bilayer GNRs is an effective mechanism to overcome such issue.

4.6 Summary

In summary, the stages that make up the process of air annealing were investigated in this chapter. Oxygen intercalation starts with the formation of an oxide layer on the SiC surface, which then decouples the BL. This in turn results in the complete removal of the bare BL from the terraces and in the conversion of the monolayer GNRs into bilayer ribbons, since the graphene layer on top acts as a protecting layer. This curious selective removal of the BL is associated with a higher chemical reactivity of the bare BL, due to a higher corrugation in comparison to the BL covered by a MLG. Subsequently, a process of lateral etching starts to develop on the GNRs from both edges, namely the SiC step edge and the border with the terrace. As the duration of the thermal treatment increases, oxide spots are formed under the graphene layers, leading to their local expansion. This process may evolve until the graphene layers burst and form holes, which expand in size over time. The combination of the lateral etching mechanism and the formation of these increasingly large holes on the graphene layers results in their complete elimination, given enough time for these processes to evolve. Although the GNRs have shown low stability under air annealing for prolonged times, this method enables the modulation of their width when using shorter durations of thermal treatment, offering an additional parameter for their controlled formation.

Diffusive 1D-transport was confirmed by probe distance dependent measurements. Despite the edge roughness of these BL-GNRs, charge carrier mobilities up to $\mu = 700\,\mathrm{cm}^2/(\mathrm{Vs})$ were measured at room temperature. Such values are comparable to other intercalated graphene systems and only marginally lower compared to epitaxial graphene without intercalates. Defects across the ribbons can be effectively circumvented by interlayer hopping of the charge carriers. In addition, the strong p-type doping in consequence of intercalation by oxygen was confirmed by local spectroscopy.

The oxygen intercalation process is robust and effectively decouples the nanoribbons from the substrate. The transport properties are not limited by the edge roughness. Although transport channels in nanostructures can easily be suppressed by in-plane defects, phonon-assisted tunneling seems to be an effective mechanism to overcome such issues. The potential to generalize this fabrication method of bilayer graphene nanostructures over large areas to patterned SiC surfaces is very promising for different applications in nanoelectronics.

5 Synthesis of graphene nanoribbons on patterned substrates

5.1 Introduction

In general, commercially available SiC substrates, once etched with hydrogen (as described in Section 2.1.2), exhibit several kinds of steps. If the substrates are tilted towards the $\langle 1-100 \rangle$ direction, straight steps run along the $\langle 11-20 \rangle$ direction [238]. As the miscut angle towards the $\langle 1-100 \rangle$ direction increases from nominally on axis to higher angles, the width of the terraces (after growth) decreases whereas the step heights increase. If, on the other hand, the substrates are tilted towards the $\langle 11-20 \rangle$ direction, the step edges acquire a zigzag shape [238]. Therefore, when it comes to natural steps, not much control can be exerted over the substrate morphology. The utilization of templated substrates is an alternative path to obtain more control over the growth of GNRs, something fundamental for future applications. The patterning of substrates makes the process of fabrication of GNRs not dependent on natural steps, and therefore on the features of each substrate.

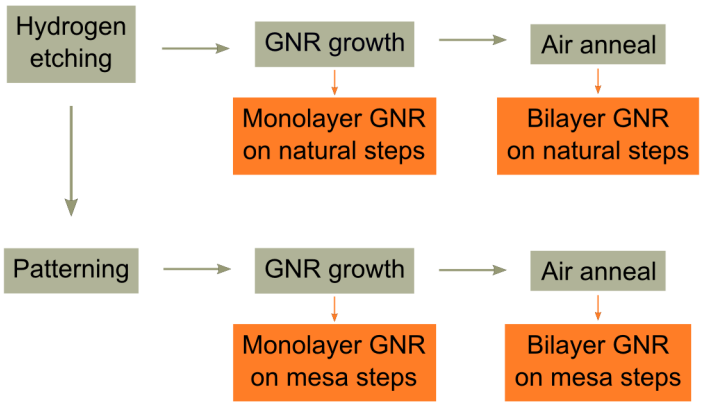

Figure 5.1: Diagram of the different paths to produce monolayer and bilayer GNRs on natural steps or on mesa steps.

Figure 5.1 illustrates a diagram of the sequence of processes that produce GNRs either on natural steps or on patterned mesa steps. The standard hydrogen etching procedure, previously described in Section 2.1.2, precedes both the direct growth of GNRs on natural steps or the patterning of the substrates. After this process, the sample can be directly grown on the SiC(0001) natural steps, producing monolayer GNRs (whose growth mechanism was explored in Chapter 3), and subsequently air annealed, generating isolated bilayer GNRs on the natural steps (whose properties were explained in Chapter 4). Alternatively, the SiC substrate can first be patterned following the hydrogen etching, which leads to the formation of mesa structures on the SiC surface. After the patterning, GNR growth and air annealing produce monolayer and bilayer GNRs, respectively, on the steps of the mesa structures. This chapter will start by briefly discussing our results regarding hydrogen etching and the influence of the substrate morphology on the formation of monolayer

GNRs, followed by a more detailed analysis of the patterning process and the morphology and transport properties of the samples after GNR growth on the mesa structures.

5.2 Hydrogen etching

The preparation of the substrates consisted of a standard hydrogen etching procedure (previously described in Section 2.1.2). Figure 5.2 exhibits AFM height images after the etching of substrates of distinct miscut angles and orientations. For each substrate, different kinds of steps are observed, while some are more ordered with occasional defects (a), others exhibited an overall wave pattern throughout the sample (b). Similarly, both larger (c) and narrower (d) terraces were observed. Such effects may be a consequence of different miscut angles that lead to various terrace widths and step heights [231], as well as different alignment between the miscut direction and the $\langle 1-100 \rangle$ direction for each substrate [238].

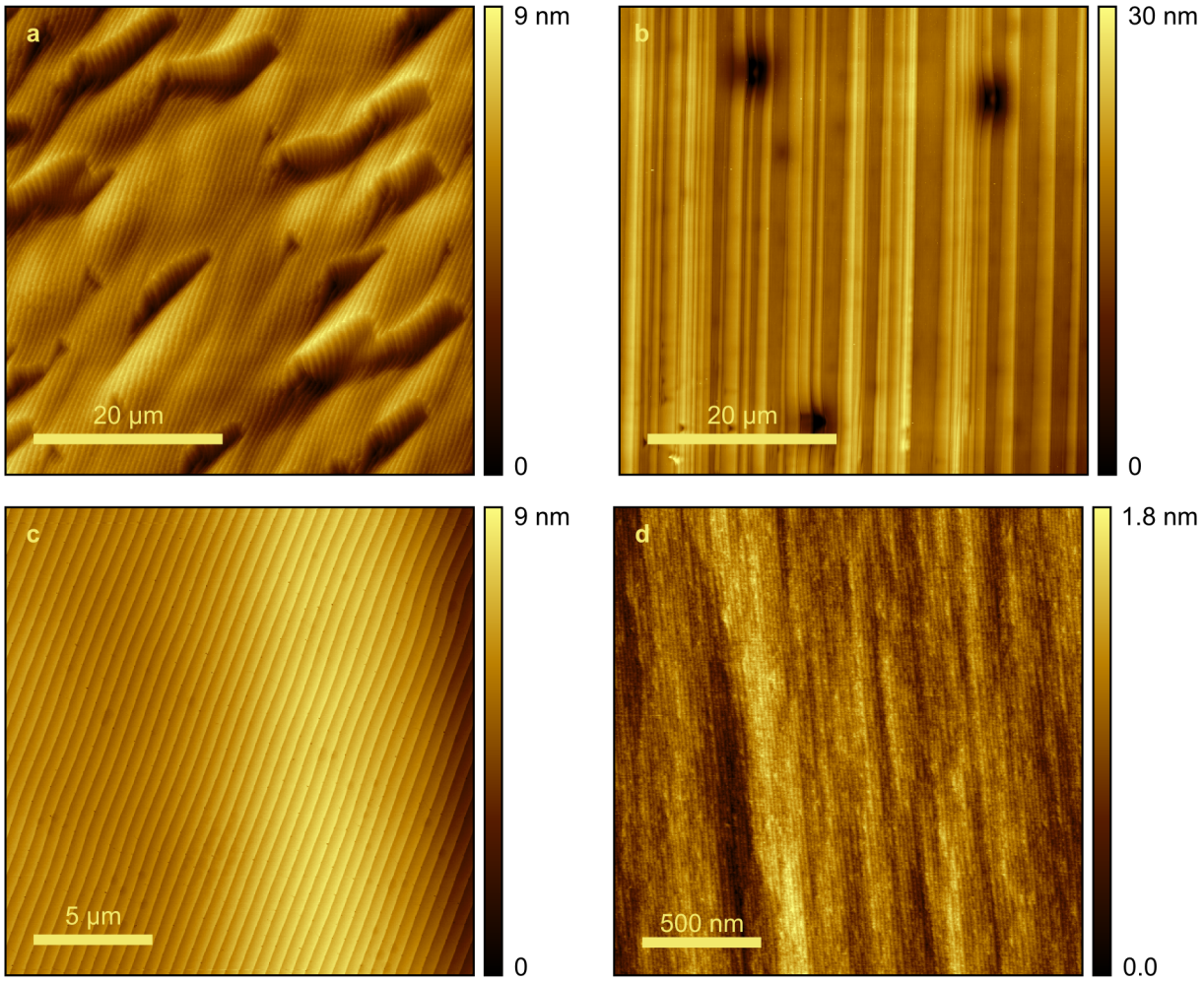

Figure 5.2: AFM height images of different SiC(0001) surfaces after hydrogen etching, with lower (a,c) and higher (b,d) miscut angles, aligned parallel (b-d) to the $\langle 11-20 \rangle$ direction and and slightly misaligned (a) with regards to this direction.

5.3 Natural steps

For the sake of comparison, a few examples of GNRs grown on natural steps will be first examined. The influence of the SiC substrate on the morphology of the GNRs can be observed in Figure 5.3. AFM height (first and third row) and phase contrast images (second and fourth row) are shown for six different substrates after GNR growth. Figures 5.3 a-c show the same semi-insulating SiC and indicate how different areas of the same wafer can result in diverse smoothness. Another semi-insulating substrate was used for the growth of samples presented in Figures 5.3 d-f, where the width of the terraces has significantly changed. Some SiC substrates were very uneven even after H-etching, as is the case of Figure 5.3 g. Finally, doped substrates were also utilized, as is the case of Figures 5.3 h-j, in which different substrates yield distinct terrace widths, as well as different alignment of the terraces. It is important to note that for the studies presented in the previous chapters (3 – 4), only samples from SiC wafers that provided high-quality stepped surfaces over large areas, similar to the one shown in Figures 5.3 i-j, were considered.

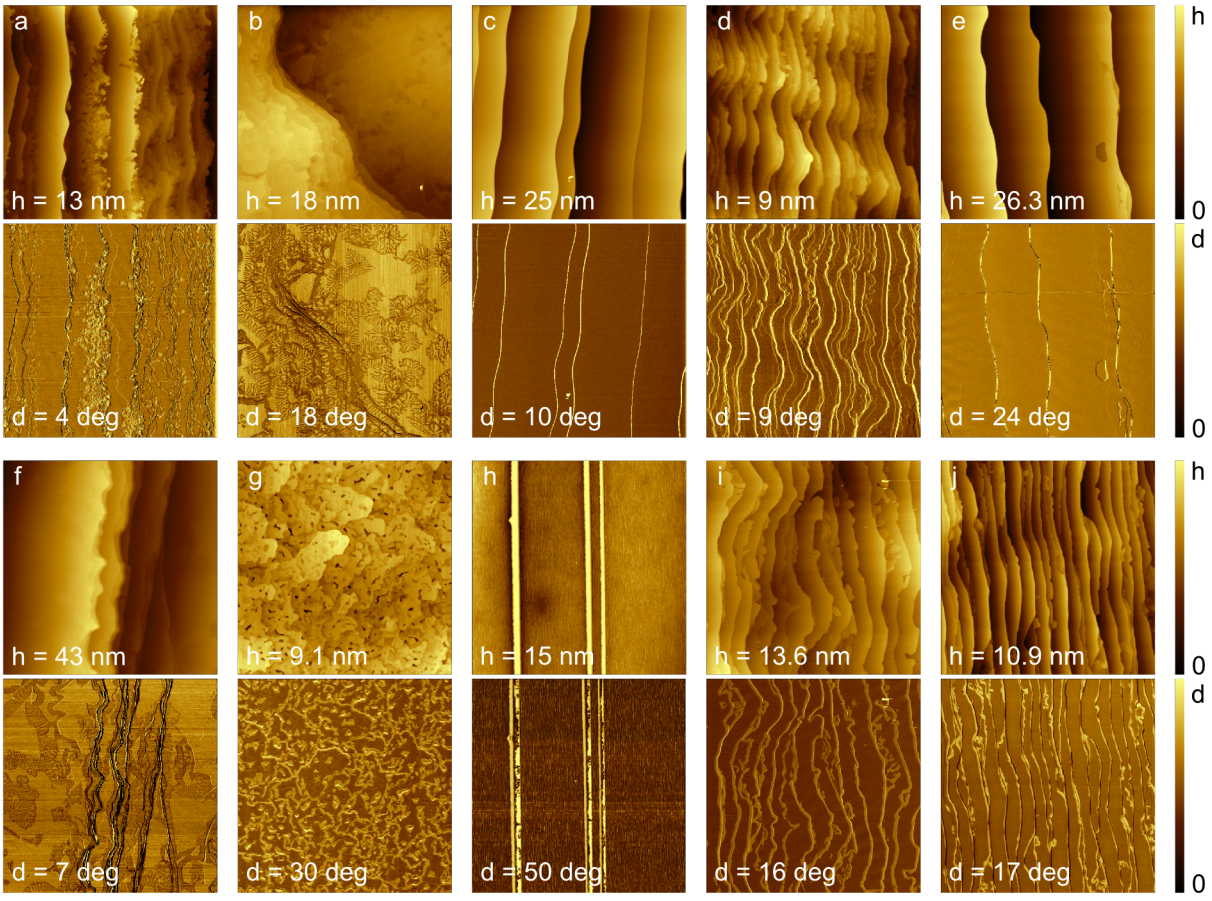

Figure 5.3: An overview of different samples fabricated under the same growth conditions (T = 1 440 °C) for GNR synthesis on various substrates.

5.4 Patterned substrates

The patterning of the structures was performed by EBL (as previously described in Section 2.2), producing well defined edges with $\sim$ 25 nm height. In contrast, previous use of conventional photolithography had produced rough edges of similar height. A comparison is shown in Figure 5.4.

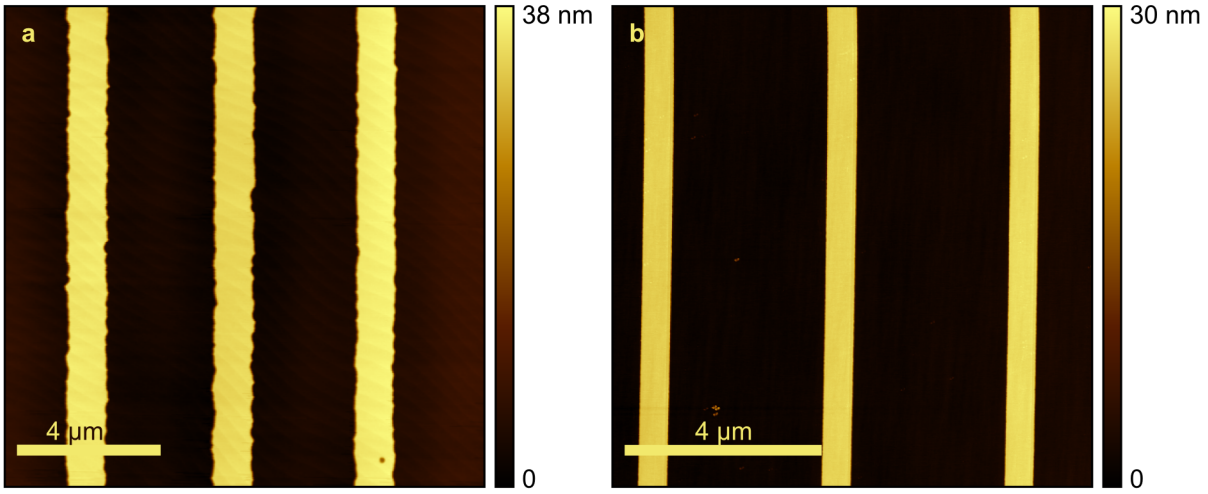

Figure 5.4: AFM height images of the SiC(0001) surface after (a) conventional optical lithography and (b) EBL.

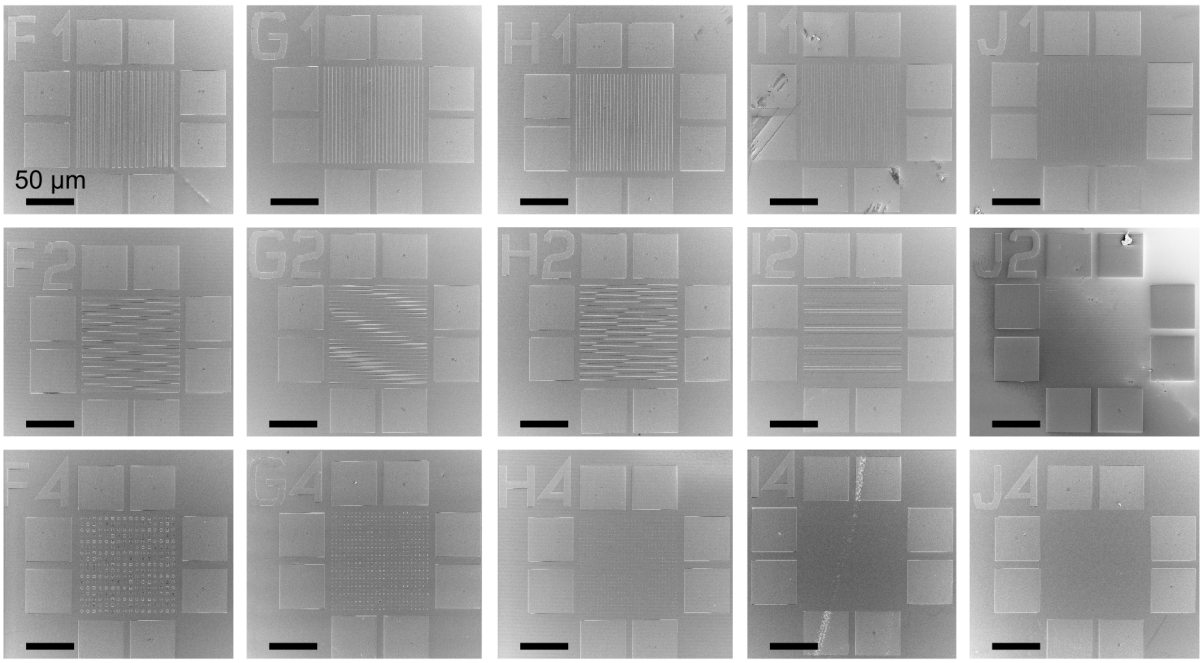

Figure 5.5: In-Lens detector SEM images of the patterns created by EBL on the SiC(0001) surface. The width of the structures is, from left to right, 3 μm, 1 μm, 500 nm, 100 nm and 50 nm, respectively.

The mask designed for EBL is shown in the SEM images of Figure 5.5. In the first row, mesas parallel to the natural steps are seen, whereas perpendicular mesas are observed in the second row. The width of the mesas decreases from 3 μm to 50 nm from left to right, with a constant separation of 3 μm between them. The goal of such structures was to analyze how mesa steps parallel and perpendicular to natural steps would differ from each other, and whether graphene growth would start from the sidewalls of the mesas and be limited to its immediate surroundings on the terraces (in a similar fashion as the one observed in Chapter 3). The third row displays other shapes patterned in the SiC surface, such as filled or outlined squares, circles and hexagons.

The lateral size of those structures varies from 3 μm to 50 nm from left to right, with a constant separation of 3 μm in between them. The idea behind designing those different shapes is to grow graphene quantum dots, circles or other shapes, and determine what is the minimal size in which graphene can be grown before the original shape is decomposed during graphene growth e.g., via SiC step bunching. However, this topic has not been investigated in the present thesis. Higher magnification images are shown in Figure 5.6, where the shapes can be more easily distinguished.

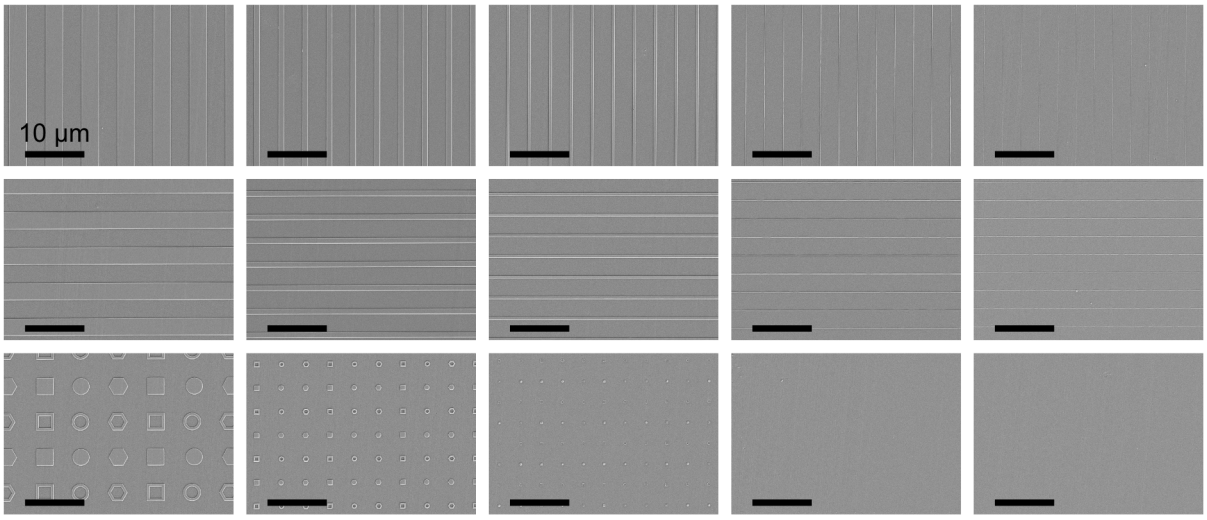

Figure 5.6: Everhart-Thornley detector SEM images of the patterns created by EBL on the SiC(0001) surface.

Bilayer GNRs were fabricated close to the step edges of the mesa structures after growth of monolayer GNRs and air annealing of the samples (as previously illustrated in Figure 5.1). The direct growth of graphene on the templated substrates often produced unstable facets that would decompose or parasitic ribbons that would connect the GNRs formed at the mesa steps from different facets. Such examples can be observed in Figure 5.7, in which AFM height in lower and higher magnifications, as well as phase contrast are exhibited in the first, second and third row, respectively. Figures 5.7 a-c show mesas with rough edges and decomposed terraces. The natural steps in Figures 5.7 d-f, which have a 90° angle in comparison to the mesa structures, are responsible for the instability of the mesa structures. A similar phenomenon is observed in the narrower mesa structures of Figures 5.7 g-i. Finally, Figures 5.7 j-l, which do not exhibit a high degree of roughness in the edges or decomposition of the mesa structures, show parasitic ribbons, originated from the SiC(0001) natural steps, that connect both edges of the mesa structure.

In order to stabilize the facets and to eliminate parasitic ribbons, different methods were pursued, such as Ar annealing or graphene growth followed by hydrogen etching and subsequent GNR growth. The most promising method, though, was vacuum annealing, which was suggested by Sprinkle et al. [90]. They have shown that the step bunching induced by vacuum annealing can eliminate the steps on the terraces. An enhancement regarding the stabilization of the mesa non polar facets could be obtained, as observed by SEM analyses (Figure 5.8) for samples where bilayer GNRs were fabricated.

AFM images of the sample after vacuum annealing at 1 200 °C for 30 min (Figure 5.9) exhibit a distinct roughness in the trenches between the mesas and at the edges of the mesas, whereas the mesa terraces offer a smooth surface with no apparent natural steps.

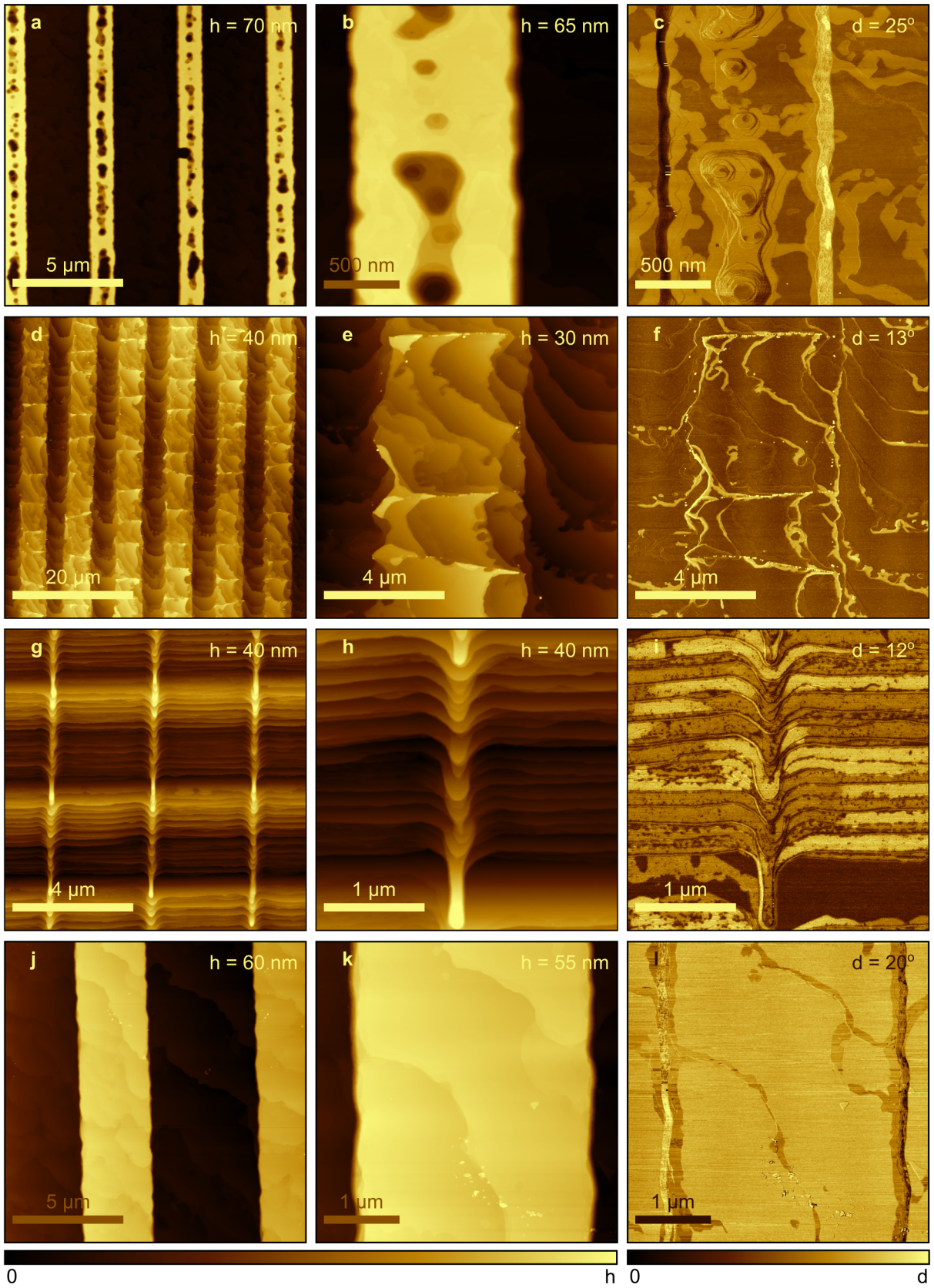

Figure 5.7: AFM height (first and second column) and phase (third column) contrast of mesa structures after GNR growth with unstable facets (a-i) and parasitic ribbons (j-k).

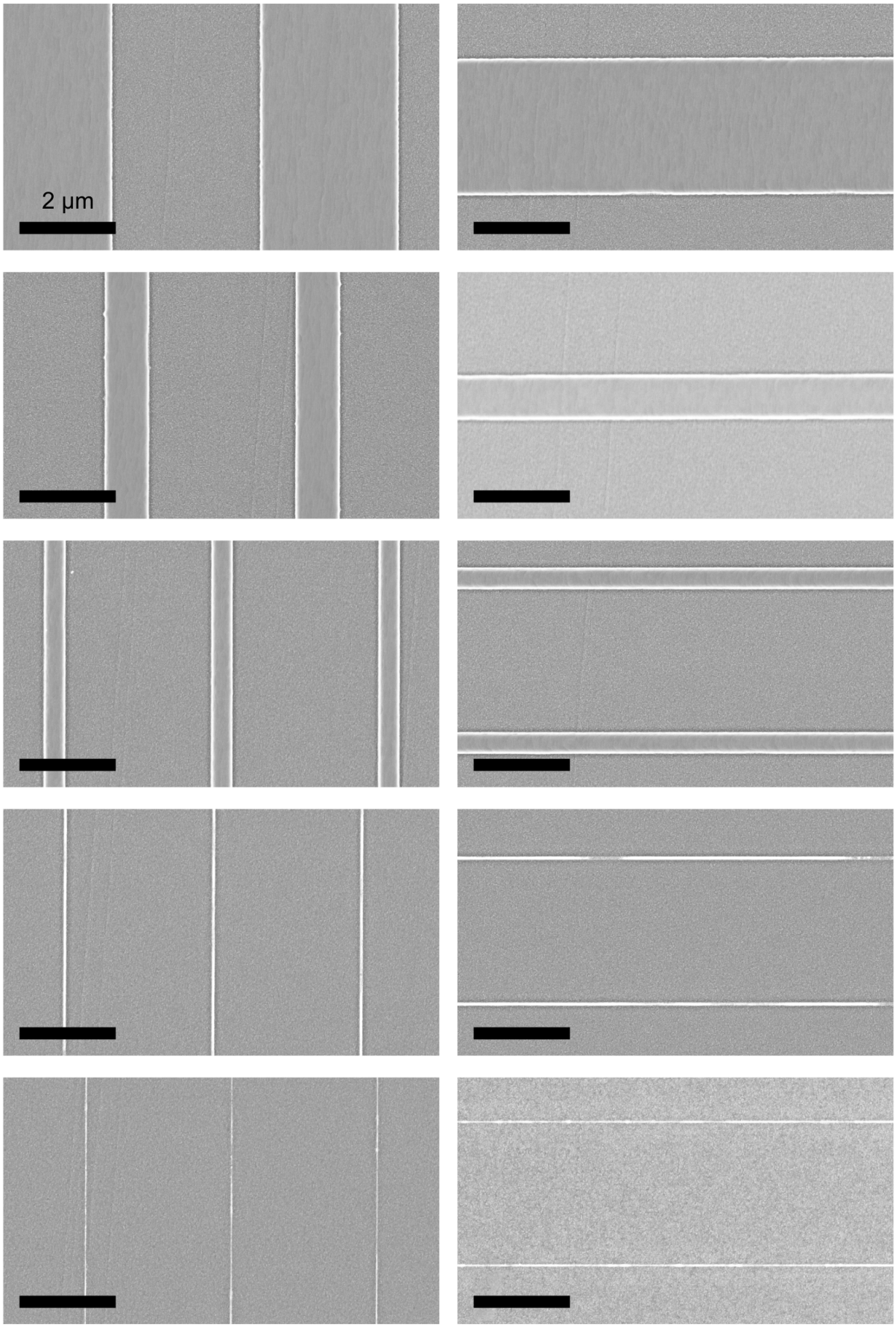

Figure 5.8: In-Lens detector SEM images of the bilayer GNRs fabricated on the templated SiC(0001) substrate. The width of the mesa structures is, from top to bottom, 3 μm, 1 μm, 500 nm, 100 nm and 50 nm, respectively.

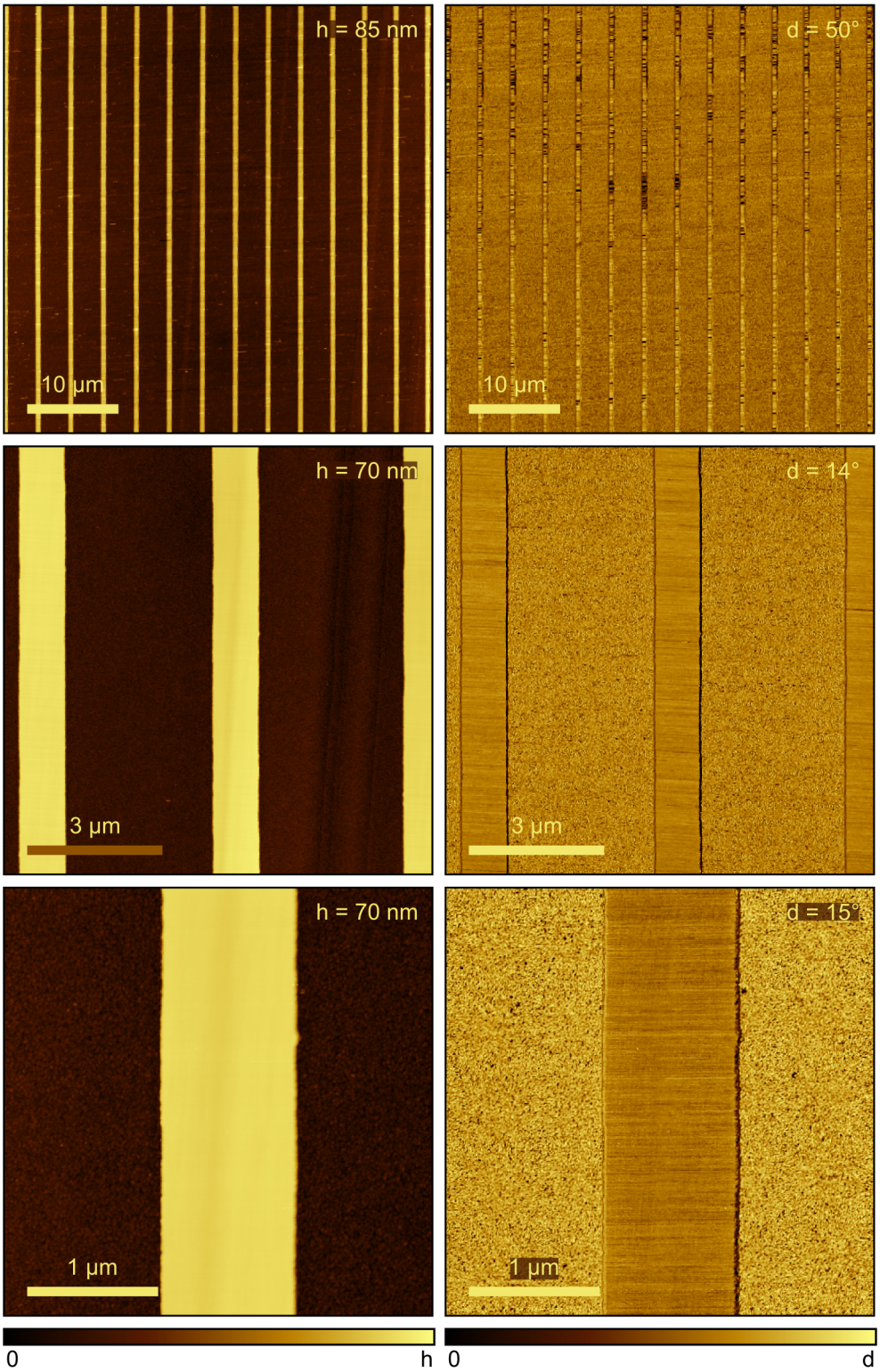

Figure 5.9: AFM height (left column) and phase (right column) contrast images of 1 μm wide mesa structures after the process of vacuum annealing at 1 200 °C for 30 min.

However, after GNR growth on these structures (Figure 5.10), natural steps can still be observed on the mesa terraces. The darker phase-contrast close to them indicates the formation of patches

of MLG.

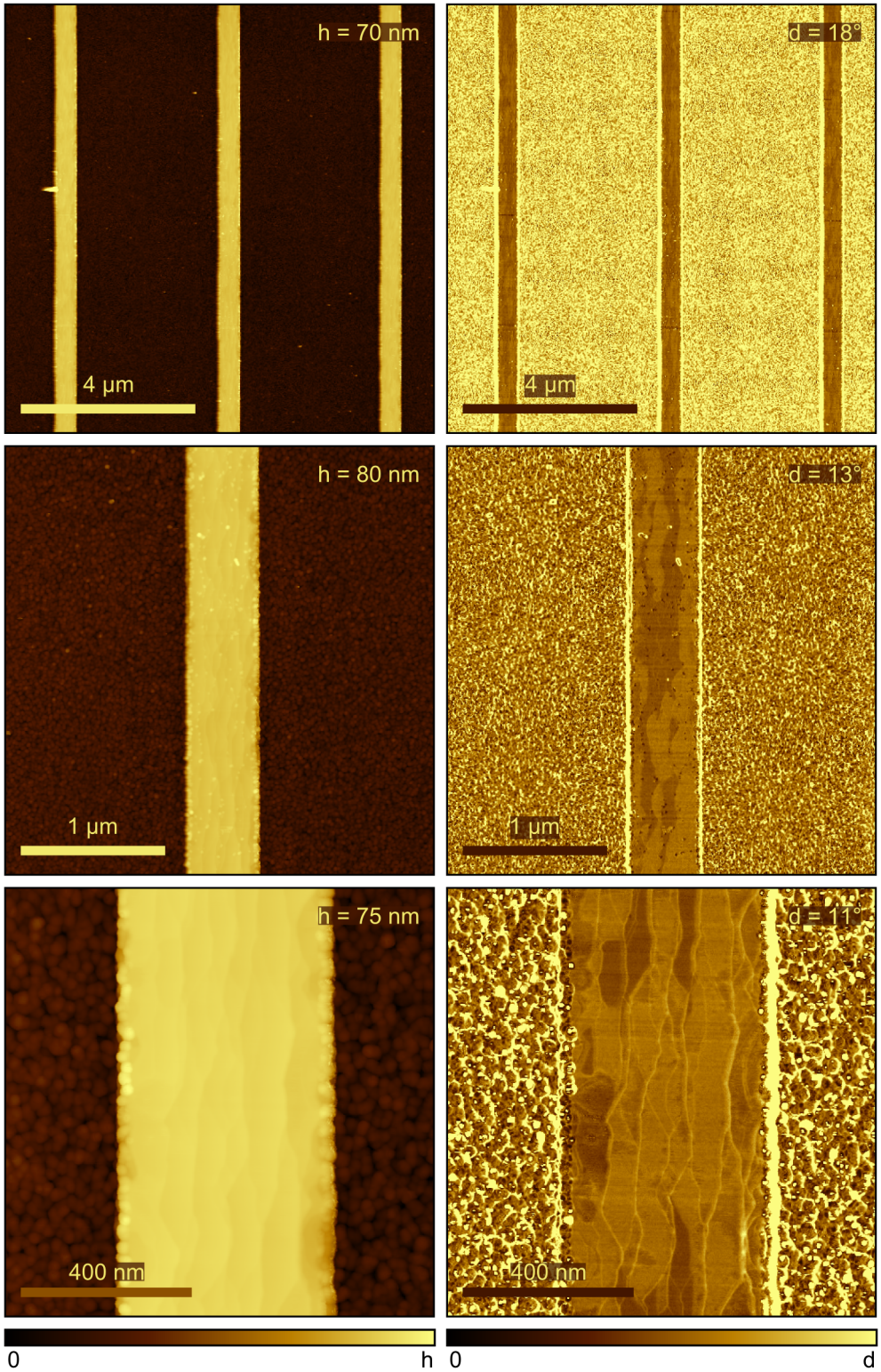

Figure 5.10: AFM height (left column) and phase (right column) contrast images of 500 nm mesa structures after the process of monolayer GNR growth (T = 1 400 °C).

Finally, the air annealing treatment for 50 min seems to partially etch the graphene patches, as indicated by the reduction of AFM phase-contrast (Figure 5.11). Nevertheless, high magnification SEM images from Figure 5.12, in which 1 μm mesas parallel (a) and perpendicular (b) to the natural steps are shown, exhibit a weak contrast suggesting that graphene patches are still present on top of the mesa structures. Due to the air annealing, they are probably composed of bilayer-thick graphene due to O_2 intercalation.

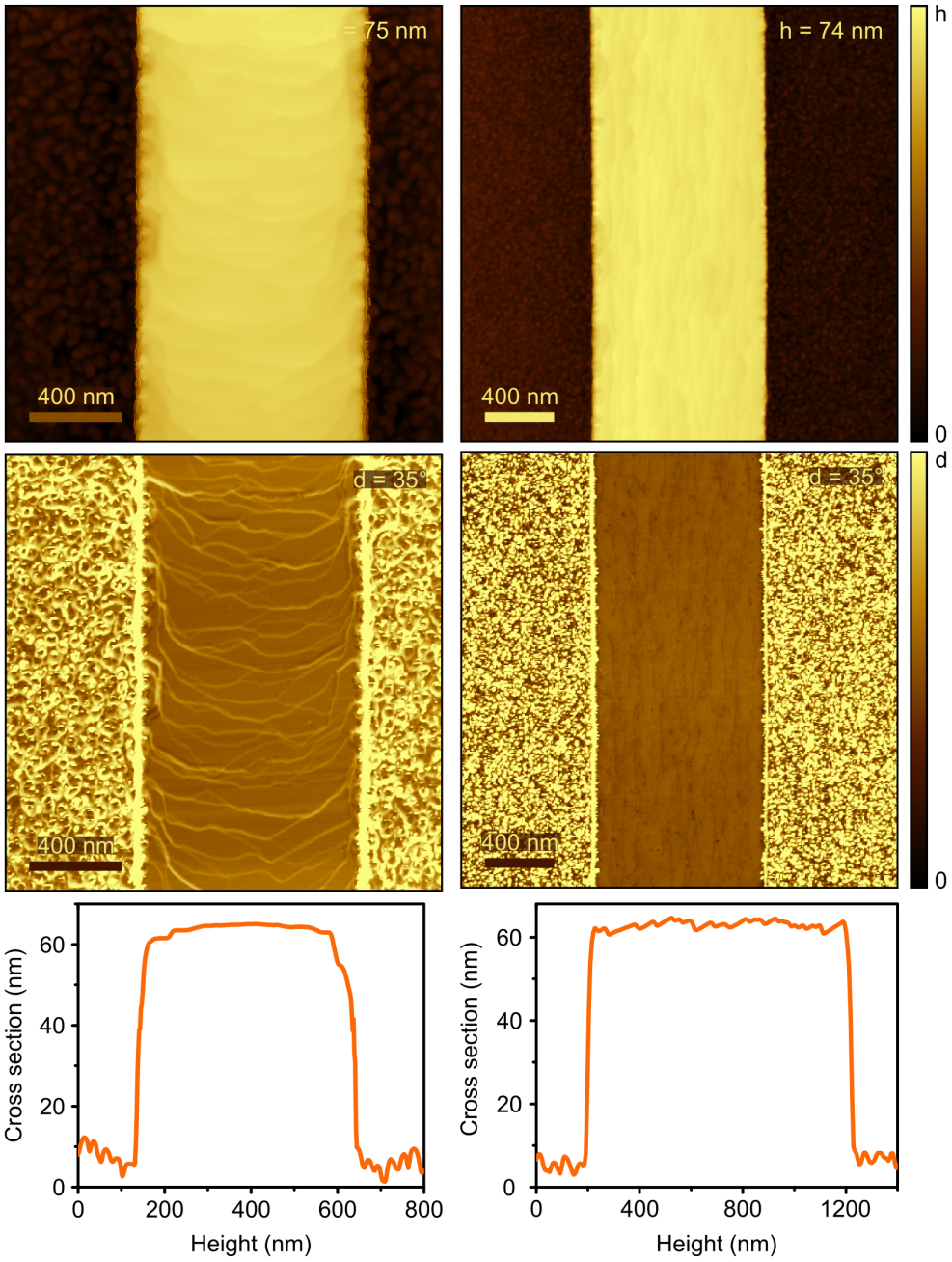

Figure 5.11: AFM height (first row) and phase (second row) contrast images as well as the cross section (last row) of bilayer GNRs grown on 1 μm mesa structures after the process of air annealing for a mesa perpendicular (left column) and one parallel (right column) to the natural steps.

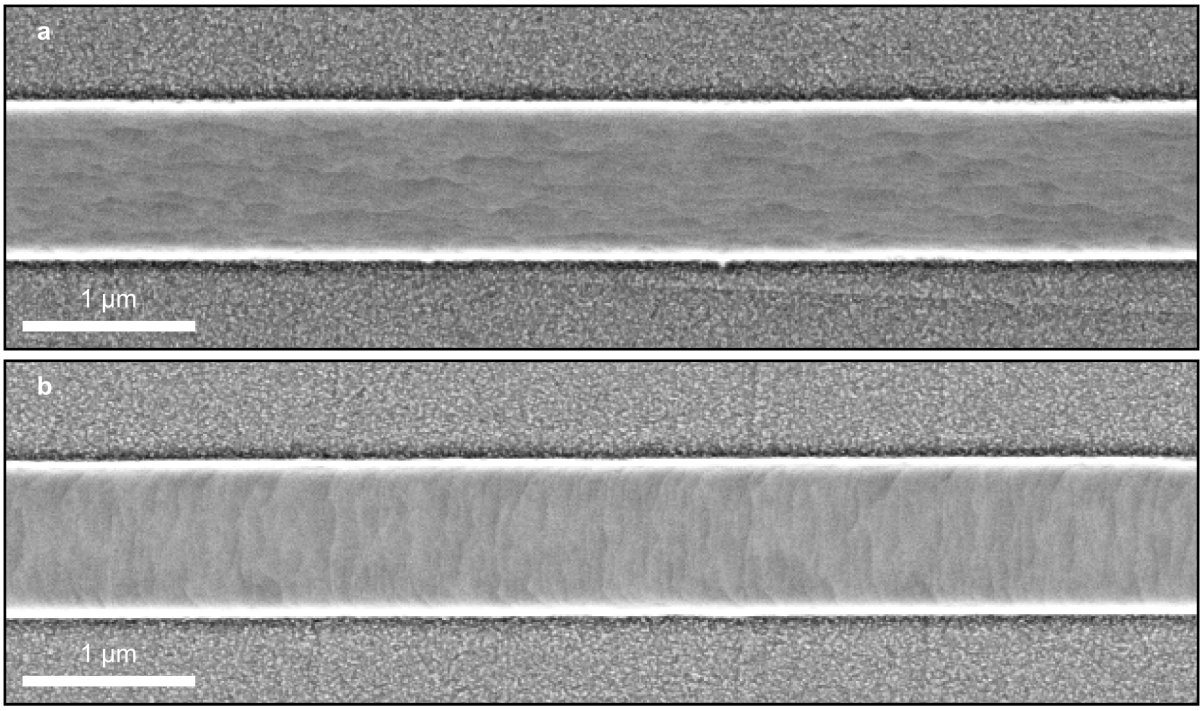

Figure 5.12: In-Lens detector SEM images of the bilayer GNRs prepared in 1 μm wide mesas aligned (a) parallel and (b) perpendicular to the orientation of the natural steps of the SiC(0001) substrate.

The formation of bilayer GNRs was further investigated by Raman spectroscopy. The intensity of the 2D peak of a structure with 3 μm wide mesas parallel to the natural steps is shown in the Raman map of Figure 5.13 a, as well as three representative spectra of the different areas of the mesa structure, i.e., one from a terrace, one from a side wall and one from a trench (Figure 5.13 b). The first feature to be observed is the clear distinction (color) between the spectra from areas that belong to the terraces and areas in the trenches, as well as areas close to the step edges, which points out to the reproducibility of the growth over a large surface area. By analyzing the spectra from the different regions (Figure 5.13 b), besides the variation in the intensity of the 2D peak, other differences can be observed. The clear D peak from the trenches indicate that graphene from this area is very defective, as confirmed by the roughness of the AFM images (Figure 5.11).

Although a very narrow G peak and the presence of a 2D peak in the terraces indicates that there is graphene everywhere in the sample, it must be considered that the laser spot size from the Raman equipment used is $\sim$ 1 μm. By combining these evidences with the images from AFM and SEM (Figures 5.11 – 5.12), it is reasonable to assume that the graphene patches in the terraces, even if reduced after the etching caused by air annealing, lead to a continuous graphene signal in the Raman map. Considering the context of parasitic ribbons (Figures 5.7 j-k), despite the improvement of the patterned SiC(0001) surface by the vacuum annealing step, the formation of graphene growth in the mesa terraces still occurs, though no longer connecting ribbons formed on the step mesas of different facets.

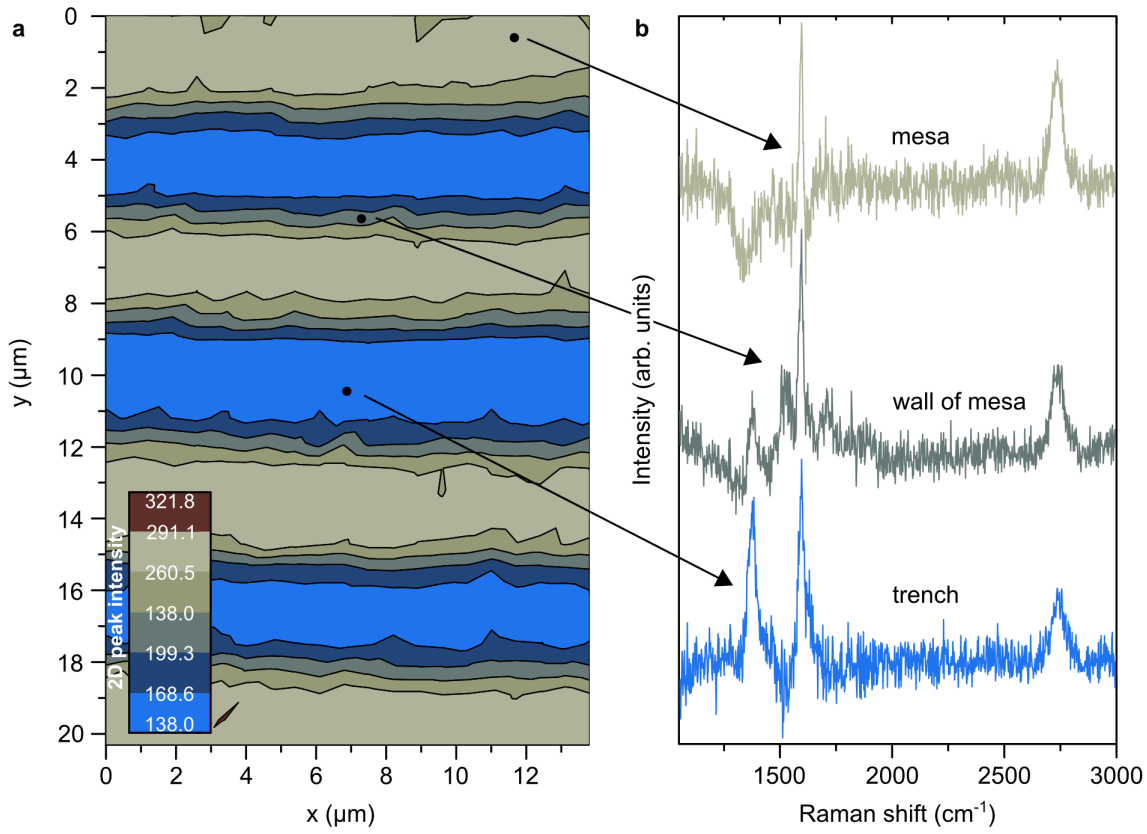

Figure 5.13: (a) Raman mapping of the 2D mode intensity from a structure with 3 μm wide mesas. (b) Representative Raman spectra of an area on top of a mesa (light green), on the wall of a mesa (dark green), and in between mesas (blue).

5.5 Transport characterization

The electronic characterization of GNRs fabricated on templated substrates occurred once again in collaboration with Johannes Aprojanz and Prof. Tegenkamp in Hanover. Figure 5.14 shows an I(V) curve from an area in the trenches, corresponding to the substrate, and from a ribbon. Once again the quality of graphene from the ribbons is contrasted with the quality of graphene in the mesa terraces/trenches, since a metallic-like, or linear, behavior is only observed when measuring close to the step edges. The non-linear behavior from the mesa terraces/trenches indicates that graphene is not continuous in this region, as also previously indicated in Figures 5.11 – 5.12.

Next, the resistance of different ribbons was measured in a linear configuration with 4 tips. Figure 5.15 shows the resistance for bilayer GNRs prepared on mesas aligned parallel to the natural steps of the substrate, whereas Figure 5.16 shows the resistance for GNRs prepared on mesas which are perpendicular to the natural steps. Probe spacing dependent measurements reveal a characteristic 1D diffusive transport behavior with resistances per length in a range of $R/l = 4-8\,\mathrm{k}\Omega/\mu\mathrm{m}$.

The average width of the ribbons was determined by analyzing height and phase contrast AFM images and taking into account that the GNRs are only present on the mesa sidewalls (since no phase contrast is observed in the area close to the mesa steps on the terraces). The size of the mesa sidewalls was obtained by considering a right triangle whose height corresponds to the height of the mesa structures, the width to the size of the phase contrast in the AFM images, and the

hypotenuse to the width of the ribbons. Considering the resulting average width of 60 nm, the sheet resistance R_S for these structures corresponds to 240 – 480 $\Omega/\square$. The mobility μ is related to the sheet resistance R_S in the following way [**?**]

$$\mu = \frac{1}{q p_S R_S}$$

where $q = 1.6 \times 10^{-19}$ C is the elementary charge and $p_S = 1.3 \times 10^{13}$ cm^{-2} the hole concentration (obtained by ARPES, see Section 4.5). From this equation, the mobility obtained for these GNRs is within the range of 1 000 – 2 000 cm^2/(V s). Equivalent measurements performed in GNRs from other structures reveal a similar behavior, indicating that the GNRs are homogeneous all over the sample and therefore confirming the reproducibility of this fabrication method. Although not significantly improved in comparison to the hole mobility obtained for bilayer GNRs fabricated on natural SiC(0001), which was $\mu = 700$ cm^2/(V s), the fact that the GNRs grown on patterned SiC(0001) exhibit electronic transport in a homogeneous fashion is of high importance to large scale applications.

As previously described in section 2.8, the combination of an SEM system with a four-tip STM setup allows a precise control over the position of the tips for transport measurements. The effect of the electron beam from this SEM system on the transport measurements was also studied. For this purpose, time dependent 4PP measurements with a fixed probe spacing of $\sim 2\,\mu$m was performed in two different conditions: after turning the electron beam on and after blocking it. The results are shown in Figure 5.17. The influence of the exposure to the electron beam is clear, the resistance increases with time if the electron beam is turned on, and decays exponentially once the electron beam is blocked. Such behavior indicates a charging effect that can be understood when considering the formation of an interfacial layer of SiO_2, product of the O_2 intercalation (already introduced in Chapter 4), after the air annealing process.

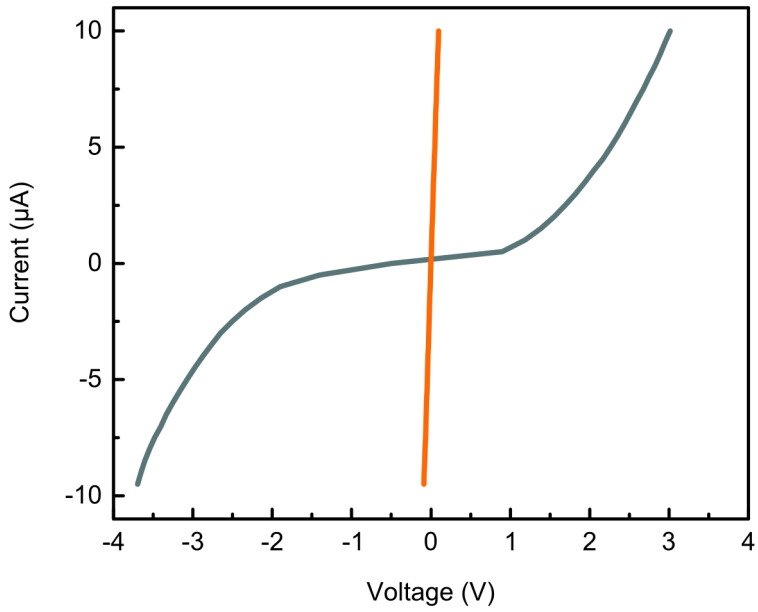

Figure 5.14: Characteristic I(V) curves taken on the trenches, corresponding to the substrate (dark grey curve), and on one GNR (orange line).

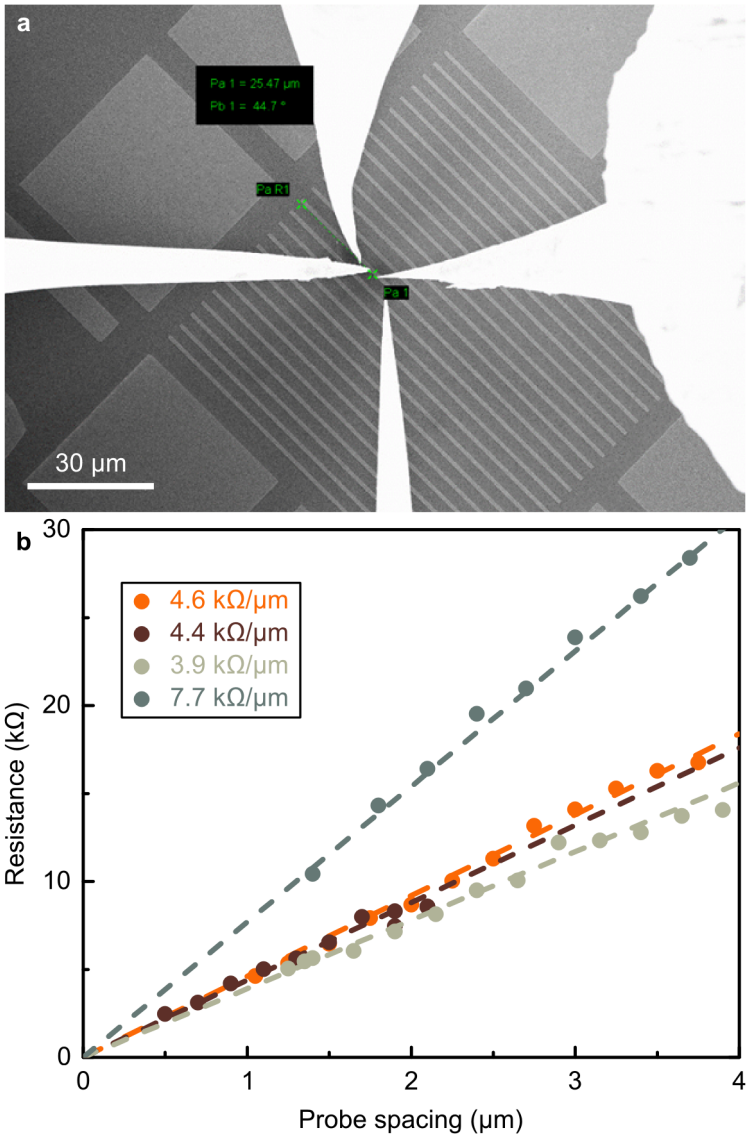

Figure 5.15: (a) In-Lens detector SEM image of the 4PP configuration in a structure with mesas aligned parallel to the natural steps of SiC(0001). (b) Resistance as a function of probe spacing for various ribbons measured on ribbon grown on mesa structures parallel to the natural steps.

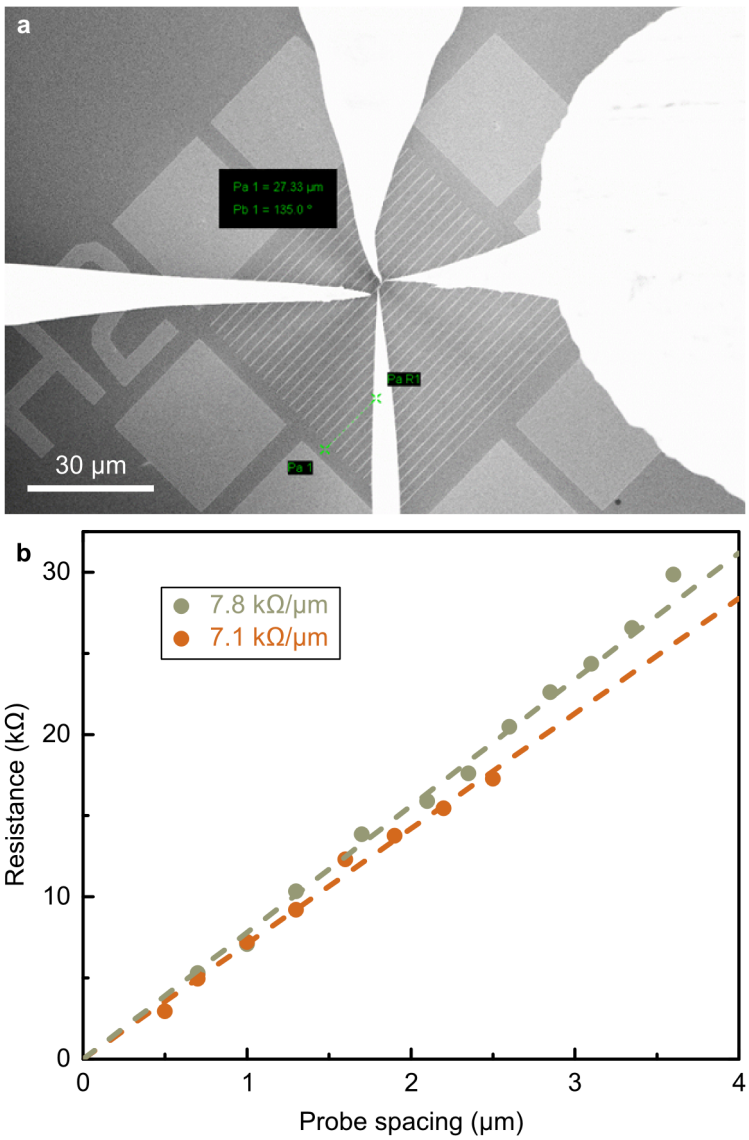

Figure 5.16: (a) In-Lens detector SEM image of the 4PP configuration in a structure with mesas aligned perpendicular to the natural steps of SiC(0001). (b) Resistance as a function of probe spacing for various ribbons measured on ribbon grown on mesa structures perpendicular to the natural steps.

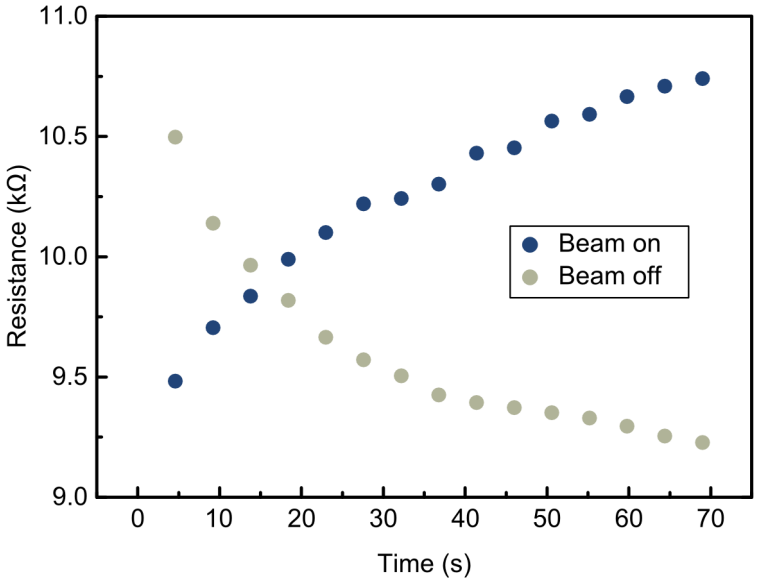

Figure 5.17: Resistance as a function of time after the electron beam used for imaging is turned on (navy blue) or blocked (grey).

5.6 Summary

The study of natural steps demonstrates the difficulty in finding suitable substrates for the growth of monolayer GNRs directly on etched SiC(0001) surfaces. The surface morphology of different substrates after hydrogen etching is varied. As a consequence, after GNR growth, the shape of the ribbons changes with substrate, leading to a non-standardized morphology, which hinders possible applications. As a solution to this issue, well defined mesa structures can be patterned by EBL on the surface of SiC.

When GNRs are fabricated directly after the patterning process, unstable facets may decompose during the growth. Even if the mesa structures are not decomposed, parasitic ribbons may still be observed crossing the terraces. To avoid such matters, vacuum annealing emerged as an intermediate route to stabilize the facets and create smooth terraces. If the GNR growth is preceded by vacuum annealing, the resulting intercalated graphene is observed as patches throughout the mesas, whereas a defective graphene is detected on the suddenly rough trenches.

Transport characterization of intercalated GNRs grown on the sidewalls of the mesas show a metallic behavior that contrasts with the non-linear I(V) curve from the substrate. Hole mobilities in the range of $1\,000-2\,000\ \mathrm{cm}^2/(\mathrm{V\,s})$ were determined for those ribbons, which, although a slight improvement when compared to bilayer GNRs grown on natural steps, exhibit high reproducibility throughout the sample, a promising feature for large-scale implementation.

6 Conclusions

The first focus of this work has been to understand the mechanisms behind the formation of monolayer and bilayer GNRs via the surface graphitization method and oxygen intercalation by air annealing, respectively. A second aim of the study was the morphological and electrical characterization of monolayer and bilayer GNRs fabricated either on natural steps or on patterned substrates.

As a way to accomplish such purpose, the growth of monolayer GNRs synthesized via the surface graphitization of stepped SiC(0001) surfaces was initially studied. Samples of monolayer GNRs were synthesized by the graphitization method on SiC(0001) with temperatures ranging from 1 410 to 1 460 °C in order to elucidate the connection between growth temperature and final ribbon width. Two substrates with different miscut angles, namely 0.1° and 2.0°, were used to determine the influence of initial step height on final GNRs size. The investigation of the width of GNRs as a function of annealing temperature and SiC substrate miscut-angle allowed to estimate an apparent activation energy for the formation of monolayer GNRs. Based on these analyses, it was possible to learn about the influence of the substrate step height on the energy barrier for GNRs formation. In substrates with a low-miscut angle, which do not exhibit few-layer graphene on the low steps, an exponential lateral expansion rate as a function of growth temperature was observed for the GNRs. In particular, an apparent activation energy of 6.1 ± 0.3 eV was obtained for the expansion rate of individual GNRs on this substrate and correlated with the energy barrier for Si out-diffusion. On the contrary, a different growth behavior was identified for ribbons grown on the high-miscut substrate, where non-polar step facets exhibited few-layer graphene. Two regimes were detected, one for temperatures below 1 430 °C, in which an activation energy of 9.2 ± 0.1 eV was determined, and another one for higher temperatures, that saturates at 2.0 ± 0.9 eV. The origin of the additional energy barrier was attributed to the formation of few-layer graphene on the step facets. The thicker layers, which act as an effective diffusion barrier, constrict Si diffusion and therefore justify the higher activation energy for lower temperatures. Nevertheless, when enough layers are formed, an increase in temperature no longer leads to a corresponding increase in GNR width, a result in line with the observed saturation of the activation energy. However, these findings contradict the idea of direct diffusion of Si through periodic defects in the BL, for which an activation energy independent on substrate step height, as well as no divergent growth behavior, would be observed between the two substrates.

The following study focused on the steps that comprise the process of air annealing. It has been observed that the oxygen intercalation starts with the formation of an oxide layer on the SiC surface, which then decouples the BL. This in turn results in the complete removal of the bare BL from the terraces and in the conversion of the monolayer GNRs into bilayer GNRs (the graphene layer on top acts as a protecting layer). Subsequently, a process of lateral etching that initiates on both edges of the GNRs, namely the SiC step edge and the border with the terrace, was observed. As the duration of the thermal treatment was increased, oxide spots were formed under the graphene layers, leading to their local expansion. This process could evolve until the graphene layers burst and formed holes, which expanded in size. The combination of the lateral etching mechanism and the formation of these increasingly large holes on the graphene layers resulted in their complete elimination, given enough time for these processes to evolve. Although the GNRs have shown low stability under air annealing for prolonged times, this method enabled the modulation of their width when using shorter durations of thermal treatment. Diffusive 1D-transport was confirmed

by probe distance dependent measurements on the bilayer GNRs. Despite the edge roughness of such ribbons, charge carrier mobilities up to $\mu = 700\,\mathrm{cm}^2/(\mathrm{Vs})$ were measured at room temperature. Defects across the GNRs can be effectively circumvented by interlayer hopping of the charge carriers. Moreover, the strong p-type doping in consequence of intercalation by oxygen was confirmed by local spectroscopy.

Since the study of natural steps demonstrated the difficulty in finding suitable substrates for the growth of GNRs directly on etched SiC(0001) surfaces, the final focus of this work was the fabrication of GNRs on patterned SiC(0001) substrates. The investigation of the surface morphology of different substrates after hydrogen etching indicated varied outcomes, which, after GNR growth, lead to diverse shapes of the ribbons. This non-standardized GNR morphology for different substrates hinders possible applications. An alternative to such issue, well defined mesa structures were patterned by EBL on the surface of SiC(0001). GNRs fabricated directly after the patterning process suffered from unstable facets that decomposed during the growth process or from parasitic ribbons that connected GNRs from different mesa steps. Vacuum annealing emerged as an intermediate step to stabilize the facets and create smooth terraces. GNR growth preceded by vacuum annealing resulted in intercalated graphene observed as patches throughout the mesa structures, whereas a defective graphene was detected on the suddenly rough trenches. Transport characterization of GNRs grown on the sidewalls of the mesas showed a metallic behavior that contrasted with the non-linear I(V) curve from the substrate. Hole mobilities in the range of $1\,000-2\,000\ \mathrm{cm}^2/(\mathrm{V\,s})$ could be determined for measurements performed in several ribbons, which indicates the robustness of the process over large-areas. Even though further improvement in the overall morphology of the graphene nanostructures has to be achieved, these results helps in paving the way for the implementation of epitaxially grown GNRs in future technologies.

Nomenclature

0D	zero-dimensional
1D	one-dimensional
2D	two-dimensional
2PP	2-point probe
3D	three-dimensional
4PP	4-point probe
AFM	atomic force microscopy
BL	buffer layer
BLG	bilayer graphene
BSE	backscattered electrons
BZ	Brillouin zone
CNTs	carbon nanotubes
CVD	chemical vapor deposition
DFT	density functional theory
EBL	electron beam lithography
FETs	field effect transistors
FG	forming gas
FWHM	full width at half maximum
GNMs	graphene nanomeshes
GNRs	graphene nanoribbons
GQDs	graphene quantum dots
HMDS	hexamethyldisilazane
HOPG	highly ordered pyrolytic graphite
LDOS	local density of states
MFC	mass flow controller
MLG	monolayer graphene
RF	radio frequency
sccm	standard cubic cm per minute
SE	secondary electrons
SEM	scanning electron microscopy
STM	scanning tunneling microscopy
STS	scanning tunneling spectroscopy

TE	transmission electron
TEM	transmission electron microscopy
XPS	X-ray photoelectron spectroscopy

Bibliography

[1] Caterina Soldano, Ather Mahmood, and Erik Dujardin. Production, properties and potential of graphene. *Carbon*, 48:2127 – 2150, 2010.

[2] A.K. Geim. Graphene: Status and Prospects. *Science*, 324:1530 – 1534, 2009.

[3] A.K. Geim and K.S. Novoselov. The rise of graphene. *Nat. Mater.*, 6:183 – 191, 2007.

[4] M.J. Allen, V.C. Tung, and R.B. Kaner. Honeycomb Carbon: A Review of Graphene. *Chem. Rev.*, 110:132 – 145, 2010.

[5] K.S. Novoselov. Electric Field Effect in Atomically Thin Carbon Films. *Science*, 306:666 – 669, 2004.

[6] Christian Riedl. *Epitaxial Graphene on Silicon Carbide Surfaces: Growth, Characterization, Doping and Hydrogen Intercalation*. PhD dissertation, Friedrich-Alexander-Universität Erlangen-Nürnberg, 2010.

[7] Y. Hernandez, V. Nicolosi, M. Lotya, F.M. Blighe, Z. Sun, S. De, I.T. McGovern, B. Holland, M. Byrne, Y.K. Gun'ko, J.J. Boland, P. Niraj, G. Duesberg, S. Krishnamurthy, R. Goodhue, J. Hutchison, V. Scardaci, A.C. Ferrari, and J.N. Coleman. High-yield production of graphene by liquid-phase exfoliation of graphite. *Nat. Nanotechnol.*, 3:563 – 568, 2008.

[8] K.S. Novoselov, A.K. Geim, S.V. Morozov, D. Jiang, M.I. Katsnelson, I.V. Grigorieva, S.V. Dubonos, and A.A. Firsov. Two-dimensional gas of massless Dirac fermions in graphene. *Nature*, 438:197 – 200, 2005.

[9] Y. Zhang, Y.W. Tan, H.L. Stormer, and P. Kim. Experimental observation of the quantum Hall effect and Berry's phase in graphene. *Nature*, 438:201 – 204, 2005.

[10] J. Wintterlin and M.L. Bocquet. Graphene on metal surfaces. *Surf. Sci.*, 603:1841 – 1852, 2009.

[11] A.T. N'Diaye, S. Bleikamp, P.J. Feibelman, and T. Michely. Two-dimensional Ir cluster lattice on a graphene moiré on Ir(111). *Phys. Rev. Lett.*, 97:219904, 2006.

[12] S. Marchini, S. Günther, and J. Wintterlin. Scanning tunneling microscopy of graphene on Ru(0001). *Phys. Rev. B*, 76:075429, 2007.

[13] P.W. Sutter, J.I. Flege, and E.A. Sutter. Epitaxial graphene on ruthenium. *Nat. Mater.*, 7:406 – 411, 2008.

[14] C. Berger, Z. Song, T. Li, X. Li, A.Y. Ogbazghi, R. Feng, Z. Dai, A.N. Marchenkov, E.H. Conrad, P.N. First, and W.A. de Heer. Ultrathin Epitaxial Graphite: 2D Electron Gas Properties and a Route toward Graphene-based Nanoelectronics. *J. Phys. Chem. B*, 108:19912 – 19916, 2004.

[15] P.R. Wallace. The band theory of graphite. *Phys. Rev.*, 71:622 – 634, 1947.

[16] J.W. McClure. Diamagnetism of graphite. *Phys. Rev.*, 104:666 – 671, 1956.

[17] J.C. Slonczewski and P.R. Weiss. Band structure of graphite. *Phys. Rev.*, 109:272 – 279, 1958.

[18] X. Lu, M. Yu, H. Huang, and R.S. Ruoff. Tailoring graphite with the goal of achieving single sheets. *Nanotechnology*, 10:269 – 272, 1999.

[19] D.A.C. Brownson, D.K. Kampouris, and C.E. Banks. Graphene electrochemistry: fundamental concepts through to prominent applications. *Chem. Soc. Rev.*, 41:6944, 2012.

[20] W.S. Hummers and R.E. Offeman. Preparation of Graphitic Oxide. *J. Am. Chem. Soc.*, 80:1339, 1958.

[21] L. Staudenmaier. Verfahren zur Darstellung der Graphitsäure. *Berichte der Dtsch. Chem. Gesellschaft*, 31:1481 – 1487, 1898.

[22] B.C. Brodie. On the Atomic Weight of Graphite. *Philos. Trans. R. Soc. Lond.*, 149:249 – 259, 1859.

[23] A.J. Van Bommel, J.E. Crombeen, and A. Van Tooren. LEED and Auger electron observations of the SiC(0001) surface. *Surf. Sci.*, 48:463 – 472, 1975.

[24] E. Fradkin. Critical behavior of disordered degenerate semiconductors. II. Spectrum and transport properties in mean-field theory. *Phys. Rev. B*, 33:3263 – 3268, 1986.

[25] K.S. Novoselov, D. Jiang, F. Schedin, T.J. Booth, V.V. Khotkevich, S.V. Morozov, and A.K. Geim. Two-dimensional atomic crystals. *Proc. Natl. Acad. Sci.*, 102:10451 – 10453, 2005.

[26] L.D. Landau. Theory of phase transformations i. *Phys. Z. Sowjetunion*, 11:26–35, 1937.

[27] S. Stankovich, D.A. Dikin, G.H.B. Dommett, K.M. Kohlhaas, E.J. Zimney, E.A. Stach, R.D. Piner, S.B.T. Nguyen, and R.S. Ruoff. Graphene-based composite materials. *Nature*, 442:282 – 286, 2006.

[28] J.C. Meyer, A.K. Geim, M.I. Katsnelson, K.S. Novoselov, T.J. Booth, and S. Roth. The structure of suspended graphene sheets. *Nature*, 446:60 – 63, 2007.

[29] R.E. Peierls. Quelques proprietes typiques des corpses solides. *Ann. I. H. Poincare*, 5:177 – 222, 1935.

[30] J.A. Venables, G.D.T. Spiller, and M. Hanbucken. Nucleation and growth of thin films. *Reports Prog. Phys.*, 47:399 – 459, 1984.

[31] J.W. Evans, P.A. Thiel, and M.C. Bartelt. Morphological evolution during epitaxial thin film growth: Formation of 2D islands and 3D mounds. *Surf. Sci. Rep.*, 61:1 – 128, 2006.

[32] C. Riedl, C. Coletti, T. Iwasaki, A.A. Zakharov, and U. Starke. Quasi-Free-Standing Epitaxial Graphene on SiC Obtained by Hydrogen Intercalation. *Phys. Rev. Lett.*, 103:246804, 2009.

[33] A.C. Ferrari, J.C. Meyer, V. Scardaci, C. Casiraghi, M. Lazzeri, F. Mauri, S. Piscanec, D. Jiang, K.S. Novoselov, S. Roth, and A.K. Geim. Raman Spectrum of Graphene and Graphene Layers. *Phys. Rev. Lett.*, 97:187401, 2006.

[34] A. Gupta, G. Chen, P. Joshi, S. Tadigadapa, and P.C. Eklund. Raman scattering from high-frequency phonons in supported n-graphene layer films. *Nano Lett.*, 6:2667 – 2673, 2006.

[35] The nobel prize in physics 2010. `http://www.nobelprize.org/nobel_prizes/physics/laureates/2010` accessed on Dec 2017.

[36] K. Lee, S. Kim, M.S. Points, T.E. Beechem, T. Ohta, and E. Tutuc. Magnetotransport properties of quasi-free-standing epitaxial graphene bilayer on SiC: Evidence for Bernal stacking. *Nano Lett.*, 11:3624 – 3628, 2011.

[37] J.-N. Fuchs and M. O. Goerbig. Introduction to the physical properties of graphene - lecture notes, 2008. `http://web.physics.ucsb.edu/~phys123B/w2015/pdf_CoursGraphene2008.pdf` accessed on Dec 2017.

[38] Prasanta K. Misra. *Physics of Condensed Matter*. Elsevier, 2010.

[39] M. Wilson. Electrons in atomically thin carbon sheets behave like massless particles. *Phys. Today*, 59:21 – 23, 2006.

[40] G.W. Semenoff. Condensed-Matter simulation of a three-Dimensional anomaly. *Phys. Rev. Lett.*, 53:2449 – 2452, 1984.

[41] F.D.M. Haldane. Model for a quantum hall effect without landau levels: Condensed-matter realization of the "parity anomaly". *Phys. Rev. Lett.*, 61:2015 – 2018, 1988.

[42] A. Schakel. Relativistic quantum Hall effect. *Phys. Rev. D*, 43:1428 – 1431, 1991.

[43] J. Gonzalez, F. Guinea, and M.A.H. Vozmediano. Unconventional quasiparticle lifetime in graphite. *Phys. Rev. Lett.*, 77:3589 – 3592, 1996.

[44] E.V. Gorbar, V.P. Gusynin, V.A. Miransky, and I.A. Shovkovy. Magnetic field driven metal-insulator phase transition in planar systems. *Phys. Rev. B*, 66:451081 – 4510822, 2002.

[45] M.I. Katsnelson. Zitterbewegung, chirality, and minimal conductivity in graphene. *Eur. Phys. J. B*, 51:157 – 160, 2006.

[46] M.I. Katsnelson, K.S. Novoselov, and A.K. Geim. Chiral tunnelling and the Klein paradox in graphene. *Nat. Phys.*, 2:620 – 625, 2006.

[47] J. Tworzydło, B. Trauzettel, M. Titov, A. Rycerz, and C.W.J. Beenakker. Sub-Poissonian Shot Noise in Graphene. *Phys. Rev. Lett.*, 96:246802, 2006.

[48] A.H. Castro Neto, F. Guinea, N.M.R. Peres, K.S. Novoselov, and A.K. Geim. The electronic properties of graphene. *Rev. Mod. Phys.*, 81:109 – 162, 2009.

[49] S. Das Sarma, A.K. Geim, P. Kim, and A.H. MacDonald. Foreword. *Solid State Commun.*, 143:1 – 2, 2007.

[50] H.C. Lee, W.W. Liu, S.P. Chai, A.R. Mohamed, A. Aziz, C.S. Khe, N.M.S. Hidayah, and U. Hashim. Review of the synthesis, transfer, characterization and growth mechanisms of single and multilayer graphene. *RSC Adv.*, 7:15644 – 15693, 2017.

[51] M.I. Katsnelson and K.S. Novoselov. Graphene: New bridge between condensed matter physics and quantum electrodynamics. *Solid State Commun.*, 143:3 – 13, 2007.

[52] M. Orlita, C. Faugeras, P. Plochocka, P. Neugebauer, G. Martinez, D.K. Maude, A.L. Barra, M. Sprinkle, C. Berger, W.A. de Heer, and M. Potemski. Approaching the Dirac Point in High-Mobility Multilayer Epitaxial Graphene. *Phys. Rev. Lett.*, 101:267601, 2008.

[53] A.S. Mayorov, R.V. Gorbachev, S.V. Morozov, L. Britnell, R. Jalil, L.A. Ponomarenko, P. Blake, K.S. Novoselov, K. Watanabe, T. Taniguchi, and A.K. Geim. Micrometer-scale ballistic transport in encapsulated graphene at room temperature. *Nano Lett.*, 11:2396 – 2399, 2011.

[54] S.V. Morozov, K.S. Novoselov, M.I. Katsnelson, F. Schedin, D.C. Elias, J.A. Jaszczak, and A.K. Geim. Giant Intrinsic Carrier Mobilities in Graphene and Its Bilayer. *Phys. Rev. Lett.*, 100:016602, 2008.

[55] H.C. Schniepp, J.L. Li, M.J. McAllister, H. Sai, M. Herrera-Alonson, D.H. Adamson, R.K. Prud'homme, R. Car, D.A. Seville, and I.A. Aksay. Functionalized single graphene sheets derived from splitting graphite oxide. *J. Phys. Chem. B*, 110:8535 – 8539, 2006.

[56] X. Du, I. Skachko, A. Barker, and E.Y. Andrei. Approaching ballistic transport in suspended graphene. *Nat. Nanotechnol.*, 3:491 – 495, 2008.

[57] K.I. Bolotin, K.J. Sikes, J. Hone, H.L. Stormer, and P. Kim. Temperature-Dependent Transport in Suspended Graphene. *Phys. Rev. Lett.*, 101:096802, 2008.

[58] K.I. Bolotin, K.J. Sikes, Z. Jiang, M. Klima, G. Fudenberg, J. Hone, P. Kim, and H.L. Stormer. Ultrahigh electron mobility in suspended graphene. *Solid State Commun.*, 146:351 – 355, 2008.

[59] K.S. Novoselov, E. McCann, S.V. Morozov, V.I. Fal'ko, M.I. Katsnelson, U. Zeitler, D. Jiang, F. Schedin, and A.K. Geim. Unconventional quantum Hall effect and Berry's phase of 2π in bilayer graphene. *Nat. Phys.*, 2(3):177–180, 2006.

[60] Z. Jiang, Y. Zhang, Y.W. Tan, H.L. Stormer, and P. Kim. Quantum Hall effect in graphene. *Solid State Commun.*, 143:14 – 19, 2007.

[61] Z. Jiang, Y. Zhang, H.L. Stormer, and P. Kim. Quantum Hall States near the Charge-Neutral Dirac Point in Graphene. *Phys. Rev. Lett.*, 99:106802, 2007.

[62] K.S. Novoselov, Z. Jiang, Y. Zhang, S.V. Morozov, H.L. Stormer, U. Zeitler, J.C. Maan, G.S. Boebinger, P. Kim, and A.K. Geim. Room-Temperature Quantum Hall Effect in Graphene. *Science*, 315:1379 – 1379, 2007.

[63] B. Özyilmaz, P. Jarillo-Herrero, D. Efetov, D.A. Abanin, L.S. Levitov, and P. Kim. Electronic Transport and Quantum Hall Effect in Bipolar Graphene p-n-p Junctions. *Phys. Rev. Lett.*, 99:166804, 2007.

[64] R.R. Nair, P. Blake, A.N. Grigorenko, K.S. Novoselov, T.J. Booth, T. Stauber, N.M.R. Peres, and A.K. Geim. Fine Structure Constant Defines Visual Transparency of Graphene. *Science*, 320:1308 – 1308, 2008.

[65] A.A. Balandin. Thermal properties of graphene and nanostructured carbon materials. *Nat. Mater.*, 10:569, 2011.

[66] A.A. Balandin, S. Ghosh, W. Bao, I. Calizo, D. Teweldebrhan, F. Miao, and C.N. Lau. Superior thermal conductivity of single-layer graphene. *Nano Lett.*, 8:902 – 907, 2008.

[67] W. Bao, F. Miao, Z. Chen, H. Zhang, W. Jang, C. Dames, and C.N. Lau. Controlled ripple texturing of suspended graphene and ultrathin graphite membranes. *Nat. Nanotechnol.*, 4:562 – 566, 2009.

[68] C. Lee, X. Wei, J.W. Kysar, and J. Hone. Measurement of the Elastic Properties and Intrinsic Strength of Monolayer Graphene. *Science*, 321:385 – 388, 2008.

[69] J.S. Bunch, S.S. Verbridge, J.S. Alden, A.M. van der Zande, J.M. Parpia, H.G. Craighead, and P.L. McEuen. Impermeable atomic membranes from graphene sheets. *Nano Lett.*, 8:2458 – 2462, 2008.

[70] M.D. Stoller, S. Park, Z. Yanwu, J. An, and R.S. Ruoff. Graphene-Based ultracapacitors. *Nano Lett.*, 8:3498 – 3502, 2008.

[71] F. Schedin, A.K. Geim, S.V. Morozov, E.W. Hill, P. Blake, M.I. Katsnelson, and K.S. Novoselov. Detection of individual gas molecules adsorbed on graphene. *Nat. Mater.*, 6:652 – 655, 2007.

[72] V.M. Pereira, A.H. Castro Neto, and N.M.R. Peres. Tight-binding approach to uniaxial strain in graphene. *Phys. Rev. B*, 80:045401, 2009.

[73] H. Cheng, Y. Huang, G. Shi, L. Jiang, and L. Qu. Graphene-Based Functional Architectures: Sheets Regulation and Macrostructure Construction toward Actuators and Power Generators. *Acc. Chem. Res.*, 50:1663 – 1671, 2017.

[74] J. Zhang, F. Zhao, Z. Zhang, N. Chen, and L. Qu. Dimension-tailored functional graphene structures for energy conversion and storage. *Nanoscale*, 5:3112, 2013.

[75] L. Dai. Functionalization of graphene for efficient energy conversion and storage. *Acc. Chem. Res.*, 46:31 – 42, 2013.

[76] Z. Xu and C. Gao. Graphene in macroscopic order: Liquid crystals and wet-spun fibers. *Acc. Chem. Res.*, 47:1267 – 1276, 2014.

[77] Z. Li, Z. Liu, H. Sun, and C. Gao. Superstructured Assembly of Nanocarbons: Fullerenes, Nanotubes, and Graphene. *Chem. Rev.*, 115:7046 – 7117, 2015.

[78] Y. Liu, Z. Xu, W. Gao, Z. Cheng, and C. Gao. Graphene and Other 2D Colloids: Liquid Crystals and Macroscopic Fibers. *Adv. Mater.*, 29:1606794, 2017.

[79] K.S. Kim, Y. Zhao, H. Jang, S.Y. Lee, J.M. Kim, K.S. Kim, J.H. Ahn, P. Kim, J.Y. Choi, and B.H. Hong. Large-scale pattern growth of graphene films for stretchable transparent electrodes. *Nature*, 457:706 – 710, 2009.

[80] X. Li, Q. Zhang, X. Chen, and M. Gu. Giant refractive-index modulation by two-photon reduction of fluorescent graphene oxides for multimode optical recording. *Sci. Rep.*, 3:2819, 2013.

[81] T. Zhang, S. Wu, R. Yang, and G. Zhang. Graphene: Nanostructure engineering and applications. *Front. Phys.*, 12:127206, 2017.

[82] J. Zheng, L. Wang, R. Quhe, Q. Liu, H. Li, D. Yu, W.N. Mei, J. Shi, Z. Gao, and J. Lu. Sub-10 nm Gate Length Graphene Transistors: Operating at Terahertz Frequencies with Current Saturation. *Sci. Rep.*, 3:1314, 2013.

[83] C. Hu, L. Song, Z. Zhang, N. Chen, Z. Feng, and L. Qu. Tailored graphene systems for unconventional applications in energy conversion and storage devices. *Energy Environ. Sci.*, 8:31 – 54, 2015.

[84] S. Fujii and T. Enoki. Nanographene and graphene edges: Electronic structure and nanofabrication. *Acc. Chem. Res.*, 46:2202 – 2210, 2013.

[85] N. Chen, X. Huang, and L. Qu. Heteroatom substituted and decorated graphene: preparation and applications. *Phys. Chem. Chem. Phys.*, 17:32077 – 32098, 2015.

[86] C.R. Dean, A.F. Young, I. Meric, C. Lee, L. Wang, S. Sorgenfrei, K. Watanabe, T. Taniguchi, P. Kim, K.L. Shepard, and J. Hone. Boron nitride substrates for high-quality graphene electronics. *Nat. Nanotechnol.*, 5:722 – 726, 2010.

[87] E.V. Castro, K.S. Novoselov, S.V. Morozov, N.M.R. Peres, J.M.B.L. dos Santos, J. Nilsson, F. Guinea, A.K. Geim, and A.H. Castro Neto. Biased Bilayer Graphene: Semiconductor with a Gap Tunable by the Electric Field Effect. *Phys. Rev. Lett.*, 99:216802, 2007.

[88] J.C. Meyer, A.K. Geim, M.I. Katsnelson, K.S. Novoselov, D. Obergfell, S. Roth, C. Girit, and A. Zettl. On the roughness of single- and bi-layer graphene membranes. *Solid State Commun.*, 143:101 – 109, 2007.

[89] J. Yan, E.A. Henriksen, P. Kim, and A. Pinczuk. Observation of Anomalous Phonon Softening in Bilayer Graphene. *Phys. Rev. Lett.*, 101:136804, 2008.

[90] M. Sprinkle, M. Ruan, Y. Hu, J. Hankinson, M. Rubio-Roy, B. Zhang, X. Wu, C. Berger, and W. de Heer. Scalable templated growth of graphene nanoribbons on SiC. *Nat. Nanotechnol.*, 5:727 – 731, 2010.

[91] Y.M. Lin, C. Dimitrakopoulos, K.A. Jenkins, D.B. Farmer, H.Y. Chiu, A. Grill, and P. Avouris. 100-GHz Transistors from Wafer-Scale Epitaxial Graphene. *Science*, 327:662 – 662, 2010.

[92] D.E.D. Pereira, D. Chernoff, Jr. E. Claudio-da Silva, and B.J. Demuner. Towards wafer-size graphene layers by atmospheric pressure graphitization of silicon carbide. *Nat. Mater.*, 8:203 – 207, 2009.

[93] Price of sic wafer. `https://order.universitywafer.com/default.aspx?cat=Silicon%20Carbide%20Wafers` accessed on Jun 2018.

[94] D. V. Badami. Graphitization of α-Silicon Carbide. *Nature*, 193:569 – 570, 1962.

[95] C. Berger, Z. Song, X. Li, X. Wu, N. Brown, C. Naud, D. Mayou, T. Li, J. Hass, A.N. Marchenkov, E.H. Conrad, P.N. First, and W.A. de Heer. Electronic confinement and coherence in patterned epitaxial graphene. *Science*, 312:1191 – 1196, 2006.

[96] T. Seyller. Passivation of hexagonal SiC surfaces by hydrogen termination. *J. Phys. Condens. Matter*, 16:S1755 – S1782, 2004.

[97] I. Forbeaux, J.-M. Themlin, and J.-M. Debever. Heteroepitaxial graphite on 6h-sic(0001): Interface formation through conduction-band electronic structure. *Physical Review B*, 58:16396–16406, 1998.

[98] M. Sabisch, P. Krüger, and J. Pollmann. Ab initio calculations of structural and electronic properties of 6H-SiC(0001) surfaces. *Phys. Rev. B*, 55:10561 – 10570, 1997.

[99] U. Starke. Atomic structure of sic surfaces. In W.J. Choyke, H. Matsunami, and G. Pensl, editors, *Silicon Carbide, Recent Major Advances*, pages 281–316. Springer, 2004.

[100] E. A. Wood. Vocabulary of surface crystallography. *J. Appl. Phys.*, 35:1306 – 1312, 1964.

[101] K. V. Emtsev, F. Speck, T. Seyller, L. Ley, and J. D. Riley. Interaction, growth, and ordering of epitaxial graphene on SiC{0001} surfaces: A comparative photoelectron spectroscopy study. *Phys. Rev. B*, 77:155303, 2008.

[102] A. Mattausch and O. Pankratov. Ab Initio Study of Graphene on SiC. *Phys. Rev. Lett.*, 99:076802, 2007.

[103] F. Varchon, R. Feng, J. Hass, X. Li, B.N. Nguyen, C. Naud, P. Mallet, J.Y. Veuillen, C. Berger, E.H. Conrad, and L. Magaud. Electronic Structure of Epitaxial Graphene Layers on SiC: Effect of the Substrate. *Phys. Rev. Lett.*, 99:126805, 2007.

[104] J. Jobst, D. Waldmann, F. Speck, R. Hirner, D.K. Maude, T. Seyller, and H.B. Weber. Quantum oscillations and quantum Hall effect in epitaxial graphene. *Phys. Rev. B*, 81:195434, 2010.

[105] U. Starke and C. Riedl. Epitaxial graphene on SiC(0001) and SiC(000$\bar{1}$): from surface reconstructions to carbon electronics. *J. Phys. Condens. Matter*, 21:134016, 2009.

[106] J. Baringhaus, M. Ruan, F. Edler, A. Tejeda, M. Sicot, A. Taleb-Ibrahimi, A.P. Li, Z. Jiang, E.H. Conrad, C. Berger, C. Tegenkamp, and W.A. de Heer. Exceptional ballistic transport in epitaxial graphene nanoribbons. *Nature*, 506:349 – 354, 2014.

[107] S. Mao and J. Chen. Graphene-based electronic biosensors. *J. Mater. Res.*, 32:2954 – 2965, 2017.

[108] E.P. Randviir, D.A.C. Brownson, and C.E. Banks. A decade of graphene research: production, applications and outlook. *Mater. Today*, 17:426 – 432, 2014.

[109] J.H. Wong, B.R. Wu, and M.F. Lin. Strain Effect on the Electronic Properties of Single Layer and Bilayer Graphene. *J. Phys. Chem. C*, 116:8271 – 8277, 2012.

[110] N. Levy, S.A. Burke, K.L. Meaker, M. Panlasigui, A. Zettl, F. Guinea, A.H. Castro Neto, and M.F. Crommie. Strain-induced pseudo-magnetic fields greater than 300 tesla in graphene nanobubbles. *Science*, 329:544 – 547, 2010.

[111] D. C. Elias, R. R. Nair, T. M. G. Mohiuddin, S. V. Morozov, P. Blake, M. P. Halsall, A. C. Ferrari, D. W. Boukhvalov, M. I. Katsnelson, A. K. Geim, and K. S. Novoselov. Control of Graphene's Properties by Reversible Hydrogenation: Evidence for Graphane. *Science (80-.).*, 323(5914):610–613, 2009.

[112] A. Celis, M. N. Nair, A. Taleb-Ibrahimi, E. H. Conrad, C. Berger, W. A. De Heer, and A. Tejeda. Graphene nanoribbons: Fabrication, properties and devices. *J. Phys. D.*, 49(14):143001, 2016.

[113] L. A. Ponomarenko, F. Schedin, M. I. Katsnelson, R. Yang, E. W. Hill, K. S. Novoselov, and A. K. Geim. Chaotic Dirac Billiard in Graphene Quantum Dots. *Science*, 320:356 – 358, 2008.

[114] J. Bai, X. Zhong, S. Jiang, Y. Huang, and X. Duan. Graphene nanomesh. *Nat. Nanotechnol.*, 5:190 – 194, 2010.

[115] X. Liang, Y. S. Jung, S. Wu, A. Ismach, D. L. Olynick, S. Cabrini, and J. Bokor. Formation of bandgap and subbands in graphene nanomeshes with sub-10 nm ribbon width fabricated via nanoimprint lithography. *Nano Lett.*, 10:2454 – 2460, 2010.

[116] M. Y. Han, B. Özyilmaz, Y. Zhang, and P. Kim. Energy Band-Gap Engineering of Graphene Nanoribbons. *Phys. Rev. Lett.*, 98:206805, 2007.

[117] L. Jiao, X. Wang, G. Diankov, H. Wang, and H. Dai. Facile synthesis of high-quality graphene nanoribbons. *Nat. Nanotechnol.*, 5:321 – 325, 2010.

[118] D.V. Kosynkin, A.L. Higginbotham, A. Sinitskii, J.R. Lomeda, A. Dimiev, B.K. Price, and J.M. Tour. Longitudinal unzipping of carbon nanotubes to form graphene nanoribbons. *Nature*, 458:872 – 876, 2009.

[119] Y.W. Son, M.L. Cohen, and S.G. Louie. Energy Gaps in Graphene Nanoribbons. *Phys. Rev. Lett.*, 97:216803, 2006.

[120] K. Nakada, M. Fujita, G. Dresselhaus, and M.S. Dresselhaus. Edge state in graphene ribbons: Nanometer size effect and edge shape dependence. *Phys. Rev. B*, 54:17954 – 17961, 1996.

[121] V. Barone, O. Hod, and G. E. Scuseria. Electronic Structure and Stability of Semiconducting Graphene Nanoribbons. *Nano Lett.*, 6:2748 – 2754, 2006.

[122] Y.Y. Li, M.X. Chen, M. Weinert, and L. Li. Direct experimental determination of onset of electron–electron interactions in gap opening of zigzag graphene nanoribbons. *Nat. Commun.*, 5:8, 2014.

[123] X. Li, X. Wang, L. Zhang, S. Lee, and H. Dai. Chemically Derived, Ultrasmooth Graphene Nanoribbon Semiconductors. *Science*, 319(5867):1229 – 1232, 2008.

[124] P. Gava, M. Lazzeri, A.M. Saitta, and F. Mauri. Ab initio study of gap opening and screening effects in gated bilayer graphene. *Phys. Rev. B*, 79:165431, 2009.

[125] T. Ohta, A. Bostwick, T. Seyller, K. Horn, and E. Rotenberg. Controlling the Electronic Structure of Bilayer Graphene. *Science*, 313:951 – 954, 2006.

[126] Y. Zhang, T.T. Tang, C. Girit, Z. Hao, M.C. Martin, A. Zettl, M.F. Crommie, Y.R. Shen, and F. Wang. Direct observation of a widely tunable bandgap in bilayer graphene. *Nature*, 459:820 – 823, 2009.

[127] F. Schwierz. Graphene transistors. *Nat. Nanotechnol.*, 5:487, 2010.

[128] B. Song, G.F. Schneider, Q. Xu, G. Pandraud, C. Dekker, and H. Zandbergen. Atomic-scale electron-beam sculpting of near-defect-free graphene nanostructures. *Nano Lett.*, 11:2247 – 2250, 2011.

[129] A. Sinitskii and J.M. Tour. Patterning graphene through the self-assembled templates: Toward periodic two-dimensional graphene nanostructures with semiconductor properties. *J. Am. Chem. Soc.*, 132:14730 – 14732, 2010.

[130] J. G. Son, M. Son, K. J. Moon, B. H. Lee, J. M. Myoung, M. S. Strano, M. H. Ham, and C. A. Ross. Sub-10 nm graphene nanoribbon array field-effect transistors fabricated by block copolymer lithography. *Adv. Mater.*, 25:4723 – 4728, 2013.

[131] L. Liao, J. Bai, Y.C. Lin, Y. Qu, Y. Huang, and X. Duan. High-performance top-gated graphene-nanoribbon transistors using zirconium oxide nanowires as high-dielectric-constant gate dielectrics. *Adv. Mater.*, 22:1941 – 1945, 2010.

[132] W. Xu, H. K. Seo, S. Y. Min, H. Cho, T. S. Lim, C. Y. Oh, Y. Lee, and T. W. Lee. Rapid fabrication of designable large-scale aligned graphene nanoribbons by electro-hydrodynamic nanowire lithography. *Adv. Mater.*, 26:3459 – 3464, 2014.

[133] W. S. Hwang, P. Zhao, K. Tahy, L. O. Nyakiti, V. D. Wheeler, R. L. Myers-Ward, C. R. Eddy, D. K. Gaskill, J. A. Robinson, W. Haensch, H. G. Xing, A. Seabaugh, and D. Jena. Graphene nanoribbon field-effect transistors on wafer-scale epitaxial graphene on SiC substrates a. *APL Mater.*, 3:011101, 2015.

[134] L. Weng, L. Zhang, Y. P. Chen, and L. P. Rokhinson. Atomic force microscope local oxidation nanolithography of graphene. *Appl. Phys. Lett.*, 93, 2008.

[135] S. Masubuchi, M. Ono, K. Yoshida, K. Hirakawa, and T. Machida. Fabrication of graphene nanoribbon by local anodic oxidation lithography using atomic force microscope. *Appl. Phys. Lett.*, 94:082107, 2008.

[136] G. Lu, X. Zhou, H. Li, Z. Yin, B. Li, L. Huang, F. Boey, and H. Zhang. Nanolithography of single-layer graphene oxide films by atomic force microscopy. *Langmuir*, 26:6164 – 6166, 2010.

[137] K. Zhang, Q. Fu, N. Pan, X. Yu, J. Liu, Y. Luo, X. Wang, J. Yang, and J. Hou. Direct writing of electronic devices on graphene oxide by catalytic scanning probe lithography. *Nat. Commun.*, 3:1194, 2012.

[138] Z. Wei, D. Wang, S. Kim, S.Y. Kim, Y. Hu, M.K. Yakes, A.R. Laracuente, Z. Dai, S.R. Marder, C. Berger, W.P. King, W.A. De Heer, P.E. Sheehan, and E. Riedo. Nanoscale tunable reduction of graphene oxide for graphene electronics. *Science*, 328:1373 – 1376, 2010.

[139] L. Tapasztó, G. Dobrik, P. Lambin, and L.P. Biró. Tailoring the atomic structure of graphene nanoribbons by scanning tunnelling microscope lithography. *Nat. Nanotechnol.*, 3:397 – 401, 2008.

[140] G. Z. Magda, X. Jin, I. Hagymási, P. Vancsó, Z. Osváth, P. Nemes-Incze, C. Hwang, L. P. Biró, and L. Tapasztó. Room-temperature magnetic order on zigzag edges of narrow graphene nanoribbons. *Nature*, 514:608 – 611, 2014.

[141] L.C. Campos, V.R. Manfrinato, J.D. Sanchez-Yamagishi, J. Kong, and P. Jarillo-Herrero. Anisotropic etching and nanoribbon formation in single-layer graphene. *Nano Lett.*, 9:2600 – 2604, 2009.

[142] S.S. Datta, D.R. Strachan, S.M. Khamis, and A.T.C. Johnson. Crystallographic etching of few-layer graphene. *Nano Lett.*, 8:1912 – 1915, 2008.

[143] L. Ci, Z. Xu, L. Wang, W. Gao, F. Ding, K. F. Kelly, B. I. Yakobson, and P. M. Ajayan. Controlled nanocutting of graphene. *Nano Res.*, 1:116–122, 2008.

[144] R. Yang, L. Zhang, Y. Wang, Z. Shi, D. Shi, H. Gao, E. Wang, and G. Zhang. An anisotropic etching effect in the graphene basal plane. *Adv. Mater.*, 22:4014 – 4019, 2010.

[145] Z. Shi, R. Yang, L. Zhang, Y. Wang, D. Liu, D. Shi, E. Wang, and G. Zhang. Patterning graphene with zigzag edges by self-aligned anisotropic etching. *Adv. Mater.*, 23:3061 – 3065, 2011.

[146] G. Wang, S. Wu, T. Zhang, P. Chen, X. Lu, S. Wang, D. Wang, K. Watanabe, T. Taniguchi, D. Shi, R. Yang, and G. Zhang. Patterning monolayer graphene with zigzag edges on hexagonal boron nitride by anisotropic etching. *Appl. Phys. Lett.*, 109:241403, 2016.

[147] T.H. Vo, M. Shekhirev, D.A. Kunkel, M.D. Morton, E. Berglund, L. Kong, P.M. Wilson, P.A. Dowben, A. Enders, and A. Sinitskii. Large-scale solution synthesis of narrow graphene nanoribbons. *Nat. Commun.*, 5:3189, 2014.

[148] J. Cai, P. Ruffieux, R. Jaafar, M. Bieri, T. Braun, S. Blankenburg, M. Muoth, A.P. Seitsonen, M. Saleh, X. Feng, K. Müllen, and R. Fasel. Atomically precise bottom-up fabrication of graphene nanoribbons. *Nature*, 466:470 – 473, 2010.

[149] H. Huang, D. Wei, J. Sun, S. L. Wong, Y. P. Feng, A. H. C. Neto, and A. T. S. Wee. Spatially resolved electronic structures of atomically precise armchair graphene nanoribbons. *Sci. Rep.*, 2:983, 2012.

[150] A. Narita, X. Feng, Y. Hernandez, S.A. Jensen, M. Bonn, H. Yang, I.A. Verzhbitskiy, C. Casiraghi, M.R. Hansen, A.H.R. Koch, G. Fytas, O. Ivasenko, B. Li, K.S. Mali, T. Balandina, S. Mahesh, S. De Feyter, and K. Müllen. Synthesis of structurally well-defined and liquid-phase-processable graphene nanoribbons. *Nat. Chem.*, 6:126 – 132, 2014.

[151] W.X. Wang, M. Zhou, X. Li, S.Y. Li, X. Wu, W. Duan, and L. He. Energy gaps of atomically precise armchair graphene sidewall nanoribbons. *Phys. Rev. B*, 93:241403, 2016.

[152] J. Baringhaus, J. Aprojanz, J. Wiegand, D. Laube, M. Halbauer, J. Hübner, M. Oestreich, and C. Tegenkamp. Growth and characterization of sidewall graphene nanoribbons. *Appl. Phys. Lett.*, 106:043109, 2015.

[153] W. A. de Heer, C. Berger, X. Wu, P. N. First, E. H. Conrad, X. Li, T. Li, M. Sprinkle, J. Hass, M. L. Sadowski, M. Potemski, and G. Martinez. Epitaxial graphene. *Solid State Commun.*, 143:92 – 100, 2007.

[154] J. Hass, W.A. de Heer, and E.H. Conrad. The growth and morphology of epitaxial multilayer graphene. *J. Phys. Condens. Matter*, 20:323202, 2008.

[155] C. Virojanadara, R. Yakimova, J.R. Osiecki, M. Syväjärvi, R.I.G. Uhrberg, L.I. Johansson, and A.A. Zakharov. Substrate orientation: A way towards higher quality monolayer graphene growth on 6H-SiC(0001). *Surf. Sci.*, 603:L87 – L90, 2009.

[156] J. Robinson, X. Weng, K. Trumbull, R. Cavalero, M. Wetherington, E. Frantz, M. LaBella, Z. Hughes, M. Fanton, and D. Snyder. Nucleation of Epitaxial Graphene on SiC(0001). *ACS Nano*, 4:153 – 158, 2010.

[157] F. Wang, Y. Zhang, C. Tian, C. Girit, A. Zettl, M. Crommie, and Y.R. Shen. Gate-variable optical transitions in graphene. *Science*, 320:206 – 209, 2008.

[158] F. Xia, T. Mueller, Y. M. Lin, A. Valdes-Garcia, and P. Avouris. Ultrafast graphene photodetector. *Nat. Nanotechnol.*, 4:839 – 843, 2009.

[159] J. Bai, X. Duan, and Y. Huang. Rational fabrication of graphene nanoribbons using a nanowire etch mask. *Nano Lett.*, 9:2083 – 2087, 2009.

[160] J. B. Oostinga, H. B. Heersche, X. Liu, A. F. Morpurgo, and L. M. K. Vandersypen. Gate-induced insulating state in bilayer graphene devices. *Nat. Mater.*, 7(2):151 – 157, 2008.

[161] F. Xia, D.B. Farmer, Y.M. Lin, and P. Avouris. Graphene field-effect transistors with high on/off current ratio and large transport band gap at room temperature. *Nano Lett.*, 10:715 – 718, 2010.

[162] W. J. Yu and X. Duan. Tunable transport gap in narrow bilayer graphene nanoribbons. *Sci. Rep.*, 3:1248, 2013.

[163] Y.M. Lin and P. Avouris. Strong suppression of electrical noise in bilayer graphene nanodevices. *Nano Lett.*, 8:2119 – 2125, 2008.

[164] B. Sahu, H. Min, A.H. MacDonald, and S.K. Banerjee. Energy gaps, magnetism, and electric-field effects in bilayer graphene nanoribbons. *Phys. Rev. B*, 78:045404, 2008.

[165] M.P. Lima, A. Fazzio, and A.J.R. da Silva. Edge effects in bilayer graphene nanoribbons: Ab initio total-energy density functional theory calculations. *Phys. Rev. B*, 79:153401, 2009.

[166] S. Bala Kumar and J. Guo. Multilayer graphene nanoribbon under vertical electric field. *J. Appl. Phys.*, 110:044309, 2011.

[167] K. Tamersit and F. Djeffal. Double-Gate Graphene Nanoribbon Field-Effect Transistor for DNA and Gas Sensing Applications: Simulation Study and Sensitivity Analysis. *IEEE Sens. J.*, 16:4180 – 4191, 2016.

[168] M. Terrones, A. R. Botello-Méndez, J. Campos-Delgado, F. López-Urías, Y. I. Vega-Cantú, F. J. Rodríguez-Macías, A. L. Elías, E. Muñoz-Sandoval, A. G. Cano-Márquez, J. C. Charlier, and H. Terrones. Graphene and graphite nanoribbons: Morphology, properties, synthesis, defects and applications. *Nano Today*, 5(4):351–372, 2010.

[169] J. Cai, C.A. Pignedoli, L. Talirz, P. Ruffieux, H. Söde, L. Liang, V. Meunier, R. Berger, R. Li, X. Feng, K. Müllen, and R. Fasel. Graphene nanoribbon heterojunctions. *Nat. Nanotechnol.*, 9:896 – 900, 2014.

[170] M. Xing, W. Fang, X. Yang, B. Tian, and J. Zhang. Highly-dispersed boron-doped graphene nanoribbons with enhanced conductibility and photocatalysis. *Chem. Commun.*, 50:6637 – 6640, 2014.

[171] I. Palacio, A. Celis, M. N. Nair, A. Gloter, A. Zobelli, M. Sicot, D. Malterre, M. S. Nevius, W. A. De Heer, C. Berger, E. H. Conrad, A. Taleb-Ibrahimi, and A. Tejeda. Atomic structure of epitaxial graphene sidewall nanoribbons: Flat graphene, miniribbons, and the confinement gap. *Nano Lett.*, 15:182 – 189, 2015.

[172] J. Hicks, A. Tejeda, A. Taleb-Ibrahimi, M. S. Nevius, F. Wang, K. Shepperd, J. Palmer, F. Bertran, P. Le Fèvre, J. Kunc, W. A. de Heer, C. Berger, and E. H. Conrad. A wide-bandgap metal–semiconductor–metal nanostructure made entirely from graphene. *Nat. Phys.*, 9:49 – 54, 2012.

[173] M. Ostler, F. Speck, M. Gick, and T. Seyller. Automated preparation of high-quality epitaxial graphene on 6H-SiC(0001). *Phys. Status Solidi B*, 247:2924 – 2926, 2010.

[174] Timo Schumann. *Direct growth and characterization of graphene layers on insulating substrates*. PhD dissertation, Humboldt-Universität zu Berlin, 2014.

[175] A.C. Ferrari and D.M. Basko. Raman spectroscopy as a versatile tool for studying the properties of graphene. *Nat. Nanotechnol.*, 8:235 – 246, 2013.

[176] A. C. Ferrari. Raman spectroscopy of graphene and graphite: Disorder, electron–phonon coupling, doping and nonadiabatic effects. *Solid State Commun.*, 143:47 – 57, 2007.

[177] Sharon Ann Holgate. *Understanding Solid State Physics*. CRC Press, 2010.

[178] P. Vandenabeele. *Practical Raman Spectroscopy*. Wiley, 2013.

[179] J. Workman. *The concise Handbook of analytical spectroscopy : theory, applications, and reference materials*. World Scientific, 2016.

[180] C. V. Raman and K. S. Krishnan. A New Type of Secondary Radiation. *Nature*, 121:501 – 502, 1928.

[181] Max Born and Kun Huang. *Dynamical Theory of Crystal Lattices*. Oxford University Press, 1954.

[182] D. M. Basko, S. Piscanec, and A. C. Ferrari. Electron-electron interactions and doping dependence of the two-phonon raman intensity in graphene. *Phys. Rev. B*, 80:165413, 2009.

[183] C. Faugeras, P. Kossacki, D.M. Basko, M. Amado, M. Sprinkle, C. Berger, W.A. de Heer, and M. Potemski. Effect of a magnetic field on the two-phonon Raman scattering in graphene. *Phys. Rev. B*, 81:155436, 2010.

[184] A. C. Ferrari and D. M. Basko. Raman spectroscopy as a versatile tool for studying the properties of graphene - supplementary information. *Nature Nanotechnology*, 8:S1–S11, 2013.

[185] P. Y. Yu and M. Cardona. *Fundamentals of Semiconductors*. Springer, 2005.

[186] F. Tuinstra and J. L. Koenig. Raman Spectrum of Graphite. *J. Chem. Phys.*, 53:1126 – 1130, 1970.

[187] A. C. Ferrari and J. Robertson. Raman spectroscopy in carbons: from nanotubes to diamond, theme issue. *Philosophical Transactions of the Royal Society A*, 362:2267 – 2565, 2004.

[188] L.M. Malard, M.A. Pimenta, G. Dresselhaus, and M.S. Dresselhaus. Raman spectroscopy in graphene. *Phys. Rep.*, 473:51 – 87, 2009.

[189] M.S. Dresselhaus, A. Jorio, and R. Saito. Characterizing Graphene, Graphite, and Carbon Nanotubes by Raman Spectroscopy. *Annu. Rev. Condens. Matter Phys.*, 1:89 – 108, 2010.

[190] M. Lazzeri, C. Attaccalite, L. Wirtz, and F. Mauri. Impact of the electron-electron correlation on phonon dispersion: Failure of LDA and GGA DFT functionals in graphene and graphite. *Phys. Rev. B*, 78:081406, 2008.

[191] R. Vidano and D.B. Fischbach. New Lines in the Raman Spectra of Carbons and Graphite. *J. Am. Ceram. Soc.*, 61:13 – 17, 1978.

[192] R. Saito, M. Hofmann, G. Dresselhaus, A. Jorio, and M.S. Dresselhaus. Raman spectroscopy of graphene and carbon nanotubes. *Adv. Phys.*, 60:413 – 550, 2011.

[193] Syahril Siregar. Double resonance raman spectra of g $\prime$ and g $*$ bands of graphene. Master thesis, Tohoku University, 2015.

[194] A.C. Ferrari and J. Robertson. Interpretation of Raman spectra of disordered and amorphous carbon. *Phys. Rev. B*, 61:14095 – 14107, 2000.

[195] C. Thomsen and S. Reich. Double resonant raman scattering in graphite. *Phys. Rev. Lett.*, 85:5214 – 5217, 2000.

[196] J. Röhrl, M. Hundhausen, K.V. Emtsev, T. Seyller, R. Graupner, and L. Ley. Raman spectra of epitaxial graphene on SiC(0001). *Appl. Phys. Lett.*, 92:201918, 2008.

[197] F. Fromm, M. H. Oliveira Jr, A. Molina-Sánchez, M. Hundhausen, J. M. J. Lopes, H. Riechert, L. Wirtz, and T. Seyller. Contribution of the buffer layer to the Raman spectrum of epitaxial graphene on SiC(0001). *New J. Phys.*, 15:043031, 2013.

[198] L.G. Cançado, A. Reina, J. Kong, and M.S. Dresselhaus. Geometrical approach for the study of G' band in the Raman spectrum of monolayer graphene, bilayer graphene, and bulk graphite. *Phys. Rev. B*, 77:245408, 2008.

[199] L.M. Malard, J. Nilsson, D.C. Elias, J.C. Brant, F. Plentz, E.S. Alves, A.H. Castro Neto, and M.A. Pimenta. Probing the electronic structure of bilayer graphene by Raman scattering. *Phys. Rev. B*, 76:201401, 2007.

[200] C. Riedl, C. Coletti, and U. Starke. Structural and electronic properties of epitaxial Graphene on SiC(0001): A review of growth, characterization, transfer doping and hydrogen intercalation. *J. Phys. D*, 43:374009, 2010.

[201] R. Beams, L. G. Cançado, and L. Novotny. Raman characterization of defects and dopants in graphene. *J. Phys. Condens. Matter*, 27:083002, 2015.

[202] G. Binnig, H. Rohrer, Ch. Gerber, and E. Weibel. Surface Studies by Scanning Tunneling Microscopy. *Phys. Rev. Lett.*, 49:57 – 61, 1982.

[203] G. Binnig, C.F. Quate, and Ch. Gerber. Atomic Force Microscope. *Phys. Rev. Lett.*, 56:930 – 933, 1986.

[204] P. Eaton and P. West. *Atomic Force Microscopy*. Oxford University Press, 2010.

[205] Q Zhong, D. Innis, K. Kjoller, and V. B. Elings. Fractured polymer/silica fiber surface studied by tapping mode atomic force microscopy. *Surface Science Letters*, 290:L688–L692, 1993.

[206] M. Dreier, D. Anselmetti, T. Richmond, U. Dammer, and H.-J. Güntherodt. Dynamic force microscopy in liquids. *Journal of Applied Physics*, 76:5095–5098, 1994.

[207] N. F. Martínez and R. García. Measuring phase shifts and energy dissipation with amplitude modulation atomic force microscopy. *Nanotechnology*, 17:S167–S172, 2006.

[208] J. Tamayo and R. García. Relationship between phase shift and energy dissipation in tapping-mode scanning force microscopy. *Applied Physics Letters*, 73:2926–2928, 1998.

[209] R. García, J. Tamayo, and A. S. Paulo. Phase contrast and surface energy hysteresis in tapping mode scanning force microsopy. *Surface and Interface Analysis*, 27:312–316, 1999.

[210] D.E.D. Pereira, D. Chernoff, Jr. E. Claudio-da Silva, and B.J. Demuner. The use of afm to investigate the delignification process: Part i - afm performance by differentiating pulping processes. *Associassion Technique de la Industrie Papeterie Magazine*, 56:6–12, 2001.

[211] M. L. Bolen, S. E. Harrison, L. B. Biedermann, and M. A. Capano. Graphene formation mechanisms on 4H-SiC(0001). *Phys. Rev. B*, 80:115433, 2009.

[212] The nobel prize in physics 1986 - perspectives. `http://www.nobelprize.org/nobel_prizes/physics/laureates/1986/perspectives.htm` accessed on Oct 2017.

[213] D. B. Williams and C. B. Carter. *Transmission Electron Microscopy*. Springer, 2009.

[214] Hyperphysics: Debroglie wavelength. `http://hyperphysics.phy-astr.gsu.edu/hbase/quantum/debrog2.html` accessed on Mai 2018.

[215] R. F. Egerton. *Physical Principles of Electron Microscopy*. Springer, 2005.

[216] Scanning electron microscope - wikipedia. `https://en.wikipedia.org/wiki/Scanning_electron_microscope` accessed on Feb 2018.

[217] W. Norimatsu and M. Kusunoki. Transitional structures of the interface between graphene and 6H–SiC(0001). *Chem. Phys. Lett.*, 468:52 – 56, 2009.

[218] W. Norimatsu and M. Kusunoki. Formation process of graphene on SiC(0001). *Physica E*, 42:691 – 694, 2010.

[219] D. C. Joy and C. S. Joy. Low voltage scanning electron microscopy. *Micron*, 27:247–263, 1996.

[220] L. Reimer. *Scanning Electron Microscopy*. Springer, 1998.

[221] Siamak Nakhaie. *Growth of graphene/hexagonal boron nitride heterostructures using molecular beam epitaxy*. PhD dissertation, Humboldt-Universität zu Berlin, 2018.

[222] J.M. Wofford, M.H. Oliveira, T. Schumann, B. Jenichen, M. Ramsteiner, U. Jahn, S. Fölsch, J.M.J. Lopes, and H. Riechert. Molecular beam epitaxy of graphene on ultra-smooth nickel: growth mode and substrate interactions. *New J. Phys.*, 16:093055, 2014.

[223] M.H. Oliveira, T. Schumann, F. Fromm, R. Koch, M. Ostler, M. Ramsteiner, T. Seyller, J.M.J. Lopes, and H. Riechert. Formation of high-quality quasi-free-standing bilayer graphene on SiC(0001) by oxygen intercalation upon annealing in air. *Carbon*, 52:83 – 89, 2013.

[224] I. Miccoli, J. Aprojanz, J. Baringhaus, T. Lichtenstein, L. A. Galves, J. M. J. Lopes, and C. Tegenkamp. Quasi-free-standing bilayer graphene nanoribbons probed by electronic transport. *Appl. Phys. Lett.*, 110:051601, 2017.

[225] Jens Baringhaus. *Mesoscopic transport phenomena in epitaxial graphene nanostructure: A surface science approach*. PhD dissertation, Gottfried Wilhelm Leibniz Universität Hannover, 2015.

[226] L. Jiao, L. Zhang, X. Wang, G. Diankov, and H. Dai. Narrow graphene nanoribbons from carbon nanotubes. *Nature*, 458:877 – 880, 2009.

[227] Y. Hagihara, T. Kajiwara, A. Visikovskiy, and S. Tanaka. Graphene Nanoribbons Grown on Epitaxial $Si_xC_yO_z$ Layer on Vicinal SiC(0001) Surfaces by Chemical Vapor Deposition. *Appl. Phys. Express*, 6:055102, 2013.

[228] T. Kajiwara, Y. Nakamori, A. Visikovskiy, T. Iimori, F. Komori, K. Nakatsuji, K. Mase, and S. Tanaka. Graphene nanoribbons on vicinal SiC surfaces by molecular beam epitaxy. *Phys. Rev. B*, 87:121407, 2013.

[229] G. Nicotra, Q.M. Ramasse, I. Deretzis, A. La Magna, C. Spinella, and F. Giannazzo. Delaminated Graphene at Silicon Carbide Facets: Atomic Scale Imaging and Spectroscopy. *ACS Nano*, 7:3045 – 3052, 2013.

[230] M. Ostler, I. Deretzis, S. Mammadov, F. Giannazzo, G. Nicotra, C. Spinella, T. Seyller, and A. La Magna. Direct growth of quasi-free-standing epitaxial graphene on nonpolar SiC surfaces. *Phys. Rev. B*, 88:085408, 2013.

[231] S. Nie, C.D. Lee, R.M. Feenstra, Y. Ke, R.P. Devaty, W.J. Choyke, C.K. Inoki, T.S. Kuan, and G. Gu. Step formation on hydrogen-etched 6H-SiC{0001} surfaces. *Surf. Sci.*, 602:2936 – 2942, 2008.

[232] J. Drowart, G. De Maria, and M. G. Inghram. Thermodynamic study of sic utilizing a mass spectrometer. *The Journal of Chemical Physics*, 29:1015–1021, 1958.

[233] S. Tanaka, K. Morita, and H. Hibino. Anisotropic layer-by-layer growth of graphene on vicinal SiC(0001) surfaces. *Phys. Rev. B*, 81:041406, 2010.

[234] C. Riedl, U. Starke, J. Bernhardt, M. Franke, and K. Heinz. Structural properties of the graphene-SiC(0001) interface as a key for the preparation of homogeneous large-terrace graphene surfaces. *Phys. Rev. B*, 76(24):245406, 2007.

[235] F. Varchon, P. Mallet, J.Y. Veuillen, and L. Magaud. Ripples in epitaxial graphene on the Si-terminated SiC(0001) surface. *Phys. Rev. B*, 77:235412, 2008.

[236] S. Kim, J. Ihm, H. J. Choi, and Y.W. Son. Origin of Anomalous Electronic Structures of Epitaxial Graphene on Silicon Carbide. *Phys. Rev. Lett.*, 100:176802, 2008.

[237] S. Nie and R.M. Feenstra. Tunneling spectroscopy of graphene and related reconstructions on SiC(0001). *J. Vac. Sci. Technol. A*, 27:1052 – 1057, 2009.

[238] A. Nakajima, H. Yokoya, Y. Furukawa, and H. Yonezu. Step control of vicinal 6H–SiC(0001) surface by H2 etching. *J. Appl. Phys.*, 97:104919, 2005.

[239] F. Ming and A. Zangwill. Model and simulations of the epitaxial growth of graphene on non-planar 6H–SiC surfaces. *J. Phys. D.*, 45:154007, 2012.

[240] L. Nemec, V. Blum, P. Rinke, and M. Scheffler. Thermodynamic Equilibrium Conditions of Graphene Films on SiC. *Phys. Rev. Lett.*, 111:065502, 2013.

[241] M.H. Oliveira, Jr., J.M.J. Lopes, T. Schumann, L.A. Galves, M. Ramsteiner, K. Berlin, A. Trampert, and H. Riechert. Synthesis of quasi-free-standing bilayer graphene nanoribbons on SiC surfaces. *Nat. Commun.*, 6:7632, 2015.

[242] M. H. Oliveira, T. Schumann, M. Ramsteiner, J. M. J. Lopes, and H. Riechert. Influence of the silicon carbide surface morphology on the epitaxial graphene formation. *Appl. Phys. Lett.*, 99:111901, 2011.

[243] K. Grodecki, R. Bozek, W. Strupinski, A. Wysmolek, R. Stepniewski, and J.M. Baranowski. Micro-Raman spectroscopy of graphene grown on stepped 4H-SiC(0001) surface. *Appl. Phys. Lett.*, 100:261604, 2012.

[244] G. F. Sun, Y. Liu, S. H. Rhim, J. F. Jia, Q. K. Xue, M. Weinert, and L. Li. Si diffusion path for pit-free graphene growth on SiC(0001). *Phys. Rev. B*, 84:195455, 2011.

[245] F. Zarotti, B. Gupta, F. Iacopi, A. Sgarlata, M. Tomellini, and N. Motta. Time evolution of graphene growth on SiC as a function of annealing temperature. *Carbon*, 98:307 – 312, 2016.

[246] S. Goler, C. Coletti, V. Piazza, P. Pingue, F. Colangelo, V. Pellegrini, K. V. Emtsev, S. Forti, U. Starke, F. Beltram, and S. Heun. Revealing the atomic structure of the buffer layer between SiC(0001) and epitaxial graphene. *Carbon*, 51:249 – 254, 2013.

[247] J. Borysiuk, J. Sołtys, R. Bożek, J. Piechota, S. Krukowski, W. Strupiński, J.M. Baranowski, and R. Stępniewski. Role of structure of C-terminated 4H-SiC(000$\bar{1}$) surface in growth of graphene layers: Transmission electron microscopy and density functional theory studies. *Phys. Rev. B*, 85:045426, 2012.

[248] A. Fissel. Artificially layered heteropolytypic structures based on SiC polytypes: molecular beam epitaxy, characterization and properties. *Phys. Rep.*, 379:149 – 255, 2003.

[249] L. H. de Lima, A. de Siervo, R. Landers, G. A. Viana, A. M. B. Goncalves, R. G. Lacerda, and P. Häberle. Atomic surface structure of graphene and its buffer layer on SiC(0001): A chemical-specific photoelectron diffraction approach. *Phys. Rev. B*, 87:081403, 2013.

[250] G. Sclauzero and A. Pasquarello. Carbon rehybridization at the graphene/SiC(0001) interface: Effect on stability and atomic-scale corrugation. *Phys. Rev. B*, 85:161405, 2012.

[251] C. Wang, H. Nakahara, and Y. Saito. *In Situ* Study on Oxygen Etching of Surface Buffer Layer on SiC(0001) Terraces. *e-Journal Surf. Sci. Nanotechnol.*, 15:13 – 18, 2017.

[252] S. Oida, F. R. McFeely, J. B. Hannon, R. M. Tromp, M. Copel, Z. Chen, Y. Sun, D. B. Farmer, and J. Yurkas. Decoupling graphene from SiC(0001) via oxidation. *Phys. Rev. B*, 82:041411, 2010.

[253] C. Mathieu, B. Lalmi, T.O. Menteş, E. Pallecchi, A. Locatelli, S. Latil, R. Belkhou, and A. Ouerghi. Effect of oxygen adsorption on the local properties of epitaxial graphene on SiC(0001). *Phys. Rev. B*, 86:035435, 2012.

[254] M. Ostler, R. J. Koch, F. Speck, F. Fromm, H. Vita, M. Hundhausen, K. Horn, and T. Seyller. Decoupling the Graphene Buffer Layer from SiC(0001) via Interface Oxidation. *Mater. Sci. Forum*, 717-720:649 – 652, 2012.

[255] M. Ostler, F. Fromm, R.J. Koch, P. Wehrfritz, F. Speck, H. Vita, S. Böttcher, K. Horn, and T. Seyller. Buffer layer free graphene on SiC(0001) via interface oxidation in water vapor. *Carbon*, 70:258 – 265, 2014.

[256] G. Kowalski, M. Tokarczyk, P. Dąbrowski, P. Ciepielewski, M. Możdżonek, W. Strupiński, and J. M. Baranowski. New X-ray insight into oxygen intercalation in epitaxial graphene grown on 4H-SiC(0001). *J. Appl. Phys.*, 117:105301, 2015.

[257] N.M. Bom, M.H. Oliveira, G.V. Soares, C. Radtke, J.M.J. Lopes, and H. Riechert. Synergistic effect of H_2O and O_2 on the decoupling of epitaxial monolayer graphene from SiC(0001) via thermal treatments. *Carbon*, 78:298 – 304, 2014.

[258] F. Speck, J. Jobst, F. Fromm, M. Ostler, D. Waldmann, M. Hundhausen, H. B. Weber, and T. Seyller. The quasi-free-standing nature of graphene on H-saturated SiC(0001). *Appl. Phys. Lett.*, 99:122106, 2011.

[259] E. Pallecchi, F. Lafont, V. Cavaliere, F. Schopfer, D. Mailly, W. Poirier, and A. Ouerghi. High Electron Mobility in Epitaxial Graphene on 4H-SiC(0001) via post-growth annealing under hydrogen. *Sci. Rep.*, 4:4558, apr 2014.

[260] N. Sieber, B. F. Mantel, T. Seyller, J. Ristein, L. Ley, T. Heller, D. R. Batchelor, and D. Schmeißer. Electronic and chemical passivation of hexagonal 6H–SiC surfaces by hydrogen termination. *Appl. Phys. Lett.*, 78:1216 – 1218, 2001.

[261] L. I. Johansson, F. Owman, and P. Mårtensson. High-resolution core-level study of 6H-SiC(0001). *Phys. Rev. B*, 53:13793 – 13802, 1996.

[262] D. Ferrah, J. Penuelas, C. Bottela, G. Grenet, and A. Ouerghi. X-ray photoelectron spectroscopy (XPS) and diffraction (XPD) study of a few layers of graphene on 6H-SiC(0001). *Surf. Sci.*, 615:47–56, 2013.

[263] V.W. Brar, Y. Zhang, Y. Yayon, T. Ohta, J.L. McChesney, A. Bostwick, E. Rotenberg, K. Horn, and M.F. Crommie. Scanning tunneling spectroscopy of inhomogeneous electronic structure in monolayer and bilayer graphene on SiC. *Appl. Phys. Lett.*, 91:122102, 2007.

[264] S. Das Sarma, S. Adam, E. H. Hwang, and E. Rossi. Electronic transport in two-dimensional graphene. *Rev. Mod. Phys.*, 83:407 – 470, 2011.

[265] M. E. Levinshtein, S. L. Rumyantsev, and M. Shur. *Properties of Advanced Semiconductor Materials: GaN, AlN, InN, BN, SiC, SiGe*. Wiley, 2001.

[266] P. Lauffer, K.V. Emtsev, R. Graupner, T. Seyller, L. Ley, S.A. Reshanov, and H.B. Weber. Atomic and electronic structure of few-layer graphene on SiC(0001) studied with scanning tunneling microscopy and spectroscopy. *Phys. Rev. B*, 77:155426, 2008.

[267] G.M. Rutter, J.N. Crain, N.P. Guisinger, T. Li, P.N. First, and J.A. Stroscio. Scattering and interference in epitaxial graphene. *Science*, 317:219–222, 2007.

[268] I. Miccoli, F. Edler, H. Pfnür, and C. Tegenkamp. The 100th anniversary of the four-point probe technique: the role of probe geometries in isotropic and anisotropic systems. *J. Phys. Condens. Matter*, 27:223201, 2015.

[269] D. K. Efetov, P. Maher, S. Glinskis, and P. Kim. Multiband transport in bilayer graphene at high carrier densities. *Phys. Rev. B*, 84:161412, 2011.

[270] W. Zhu, V. Perebeinos, M. Freitag, and P. Avouris. Carrier scattering, mobilities, and electrostatic potential in monolayer, bilayer, and trilayer graphene. *Phys. Rev. B*, 80:235402, 2009.

[271] Y.W. Tan, Y. Zhang, H. L. Stormer, and P. Kim. Temperature dependent electron transport in graphene. *Eur. Phys. J. Spec. Top.*, 148:15 – 18, 2007.

[272] J. Baringhaus, F. Edler, C. Neumann, C. Stampfer, S. Forti, U. Starke, and C. Tegenkamp. Local transport measurements on epitaxial graphene. *Appl. Phys. Lett.*, 103:111604, 2013.

[273] X.Y. Fang, X.X. Yu, H.M. Zheng, H.B. Jin, L. Wang, and M.S. Cao. Temperature- and thickness-dependent electrical conductivity of few-layer graphene and graphene nanosheets. *Phys. Lett. A*, 379(37):2245 – 2251, oct 2015.

[274] L. Edman, B. Sundqvist, E. McRae, and E. Litvin-Staszewska. Electrical resistivity of single-crystal graphite under pressure: An anisotropic three-dimensional semimetal. *Phys. Rev. B*, 57:6227 – 6230, 1998.

Acknowledgments

I would like to first acknowledge the two institutions that allowed me to perform the work presented in this thesis:

My PhD fellowship of the CAPES Foundation, from the Ministry of Education of Brazil, through the program Science Without Borders (process no. 13461/13-3).

The Paul-Drüde-Institut für Festkürperelektronik in Berlin, where the majority of the experiments, analysis, and writing of this thesis took place.

This work would also not have been possible without the guidance, collaboration and support from the following people:

Prof. Dr. Henning Riechert, for for giving me the opportunity to perform this work at the PDI.

Dr. João Marcelo J. Lopes, for, from the very beginning, writing with me the proposal for this project, guiding me throughout the research and the understanding of data, and supervising the writing of this thesis.

Similarly, I would like to thank the present and past members of the graphene group: Dr. Timo Schumann, who introduced me to the growth of epitaxial graphene on SiC(0001) and AFM characterization; Dr. Joseph M. Wofford and Dr. Gabriel V. Soares, for fruitful discussions about the growth mechanism of GNRs; Dr. Martin Heilmann, for discussions about the process of O_2 intercalation of graphene and translation of the abstract of this thesis into German; and Dr. Siamak Nakhaie, for helpful scientific (and informal) conversations; Ms. Tahiyat Huq for the collaborative study of the buffer layer growth and for providing me the experience of guiding someone myself.

Dr. Lutz Geelhaar for welcoming me in the Department of Epitaxy.

All the collaborators from the institute, Dr. Abbes Tahraoui and Mr. Walid Anders for the production of patterned SiC substrates; Dr. Manfred Ramsteiner for introducing me to the Raman system, Dr. Achim Trampert and Dr. Katja Berlin for the TEM measurements; Dr. Uwe Jahn and Dr. Carsten Pfüller for assisting me with the SEM measurements.

The collaborators from outside of our institute, who helped me expand my research: Dr. Muhammad Y. Bashouti, from the Ben-Gurion University of the Negev, for performing the XPS measurements and assisting me with the analysis; Dr. Christoph Tegenkamp, Dr. Ilio Miccoli, Dr. Timo Lichtenstein and Johannes Aprojanz, from Leibniz Universität Hannover, for the transport measurements, and in particular to J. Aprojanz for also assisting me with the understanding the transport measurements.

Ms. Claudia Herrmann, for assisting me in the use of AFM, as well as Mr. Michael Höricke and Mr. Hans-Peter Schönherr for technical support in the MBE and chemistry laboratories.

Mr. Andreas Hartung for all the assistance with documentation in the PDI and the Ausländerbehörde, and for doing so with an uplifting sense of humor.

All the colleagues for the scientific and non-scientific discussions.

All the friends who helped me keep sane throughout these years and ultimately made this experience much nicer, in particular: Alex, Dé, Laís, Lari, Gabi, Vale, Rui Ning, Tuan, and Ziani.

Minha família por todo apoio e carinho, em especial meus pais, que estão próximos mesmo a 11 000 km de distância.

Selbständigkeitserklärung

Ich erkläre, dass ich die vorliegende Arbeit selbständig und nur unter Verwendung der angegebenen Literatur und Hilfsmittel angefertigt habe.

Berlin, den 30.07.2018 Lauren Aranha Galves